# POLITECNICO
## MILANO 1863

# Molecular sensing with surface waves

Physics Department

Doctoral Programme in Physics

Doctoral dissertation of: **Erika Mogni**

Supervisor: Prof. Paolo Biagioni
Tutor: Prof. Marco Finazzi
The Chair of the Doctoral Program: Prof. Marco Finazzi

March 2023

# Abstract

Optical sensors are well-established tools in today's life. The specific detection of small quantities of analytes has a huge importance due to its application in medicine and life science so sensing tools that allow enhancing the molecular signals are of great interest. Bloch Surface Waves (BSWs) generated at the surface of a semi-infinite one-dimensional photonic crystal (1DPC) and Surface Plasmon Polaritons (SPPs) generated at the surface of a metallic layer are nowadays well-known tools for surface-enhanced spectroscopies and will be discussed in this Thesis. BSWs and SPPs share common points like being evanescent surface waves used for surface-enhanced spectroscopies but they have many differences that will be exploited: SPPs are sustained by a metallic surface while BSWs are generated at the surface of a 1DPC made by dielectric materials; with SPPs one can work in the red – near infrared part of the spectrum while with a careful choice of materials and thicknesses, one can tune the BSWs resonances and cover, as in the case presented in this manuscript, the visible – UV range, allowing for the investigation of resonant electronic states of molecules. Moreover, due to their coupled nature to electronic oscillations on the surface, SPPs can be excited only with TM polarization of the illuminating beam, while photonic crystals can sustain both TE and TM surface modes, allowing the investigation of resonant electronic states of molecules. TE and TM modes have, in general, different phase velocities, i.e. different dispersion relations, so one could not have the control over the polarization state of their combination over a broadband spectral range. With this motivation, we propose a novel design of a 1DPC that allows for the overlap of dispersion relations over a broadband spectral range. The first important step is the experimental demonstration of this feature that in our experimental setup configuration, described in Chapter 2, translated into collecting reflectivity signals from the samples, where surface modes appear as dips, and check that they are excited at the same angle when the wavelength of illumination is fixed. The validation of our 1DPC platform is described in Chapter 3 where different designs are analyzed in an aqueous environment. The mode overlap is also exploited for preliminary circular dichroism measurements performed during the last days of the PhD, that leave the door open for further developments of the acquisition process. The simultaneous excitation of TE and TM modes, in fact, allows for the generation of a so called "superchiral" wave, used for the study of chiral molecules. Chirality is an important geometric property of objects that cannot be superimposed to their mirror image through translations or rotations and, since many biocomponents are chiral, the study of this property has many applications in molecular physics, chemistry and life

science. Afterwards, the mode superposition is exploited for polarization-sensitive measurements where it is possible to investigate the birefringence of a molecular layer, i.e. to distinguish between random and oriented molecules anchored to the surface. In this field, we investigate the birefringence of a single-stranded DNA layer immobilized on the 1DPC surface through the simultaneous tracking of the TE and TM resonances, showing the results in Chapter 4. In the SPPs field, instead, we worked on a biosensor whose final goal is the detection of a specific antigen in blood. Biosensors are made by a transducer that collects the biological response, and an electronic system that elaborates and shows it to the user. We worked on the optical validation of the functionalization protocol of the transducer of the biosensor and the activity is reported in Chapter 5. We worked on a prototype of transducer, testing if each step of the functionalization is successful. Moreover, we performed preliminary measurements with the aim to detect the binding of the antigen to the correspondent antibody. Optical results are then compared with the electronic characterization of the sample, presenting a good accordance, that confirms the consistent operation of the sensor under investigation.

**Key-words:** surface waves; one-dimensional photonic crystals; surface plasmon polaritons; Bloch surface waves; superchirality; circular dichroism; polarization-resolved spectroscopy; biosensors.

# Riassunto

I sensori ottici sono ad oggi degli strumenti presenti nella vita di tutti i giorni. L'acquisizione specifica di segnali provenienti da piccole quantità di componenti biologici è di grande importanza viste le possibili applicazioni in medicina, farmacologia e nell'ambito delle scienze della vita; quindi, gli strumenti in grado di amplificare il segnale molecolare sono ad oggi di grande interesse. Le onde superficiali di Bloch generate sulla superficie di un cristallo fotonico monodimensionale e i plasmoni di superficie generati sulla superficie di un film metallico sono ormai strumenti molto conosciuti per le tecniche di spettroscopia ottica di superficie, come viene discusso in questa tesi. Le onde di Bloch e i plasmoni hanno alcuni punti in comune come l'essere onde di superficie evanescenti usate per tecniche di spettroscopia ottica ma hanno anche molte differenze che verranno descritte: i plasmoni sono sostenuti da una superficie metallica mentre le onde di Bloch sono generate sulla superficie di un cristallo fotonico monodimensionale costituito da materiali dielettrici; con i plasmoni è possibile focalizzarsi nella regione spettrale del rosso – vicino infrarosso, mentre per le onde di Bloch con una scelta accurata dei materiali e degli spessori di ciascuno strato è possibile controllare le risonanze e raggiungere, come presentato in questo lavoro, il visibile – UV, permettendo così lo studio degli stati elettronici delle molecole. Inoltre, a causa del loro accoppiamento con le oscillazioni elettroniche superficiali, i plasmoni possono essere eccitati solo con una polarizzazione TM della luce incidente, mentre i cristalli fotonici possono sostenere entrambe le polarizzazioni, TE e TM, dei modi di superficie, permettendo così lo studio degli stati elettronici delle molecole. I modi TE e TM hanno, in generale, velocità di fase differenti, il che significa che hanno relazioni di dispersione distinte; quindi, non è possibile controllare lo stato di polarizzazione dell'onda ottenuta dalla loro combinazione in un ampio range spettrale. Con questa motivazione, abbiamo proposto un nuovo design di cristallo fotonico monodimensionale che permette la sovrapposizione delle relazioni di dispersione dei modi superficiali su un ampio intervallo spettrale. Il primo risultato importante è stata la dimostrazione sperimentale di questa proprietà che, nella nostra configurazione sperimentale descritta nel Capitolo 2, corrisponde all'acquisizione di segnali di riflettività dei campioni, dove le onde di superficie appaiono come picchi di assenza di segnale, e controllare che l'angolo di eccitazione dei due modi è lo stesso quando la lunghezza d'onda di illuminazione è fissata. La validazione del nostro campione è descritta nel Capitolo 3 dove design diversi della piattaforma sono analizzati usando l'acqua come mezzo esterno. La sovrapposizione dei modi è stata anche utilizzata per acquisire delle

misure preliminari di dicroismo circolare durante gli ultimi giorni di dottorato, che lasciano spazio per ulteriori sviluppi e miglioramenti nel processo di acquisizione. La generazione simultanea dei modi TE e TM, infatti, permette di originare una cosiddetta onda "superchirale", usata per lo studio di molecole chirali. La chiralità è un'importante proprietà geometrica degli oggetti che non possono essere sovrapposti alla loro immagine speculare per mezzo di sole traslazioni e rotazioni e, poiché molti componenti biologici sono chirali, lo studio di questa proprietà ha molte applicazioni nella fisica molecolare, nella chimica e nelle scienze della vita. Successivamente, la sovrapposizione dei modi è stata utilizzata per compiere misure sensibili alla polarizzazione dove è possibile studiare la birifrangenza di uno strato molecolare, che significa poter distinguere tra molecole disordinate oppure ordinatamente disposte sulla superficie. Per quanto riguarda questo argomento, abbiamo studiato la birifrangenza di uno strato composto da singole eliche di DNA immobilizzate sulla superficie del cristallo fotonico attraverso il tracciamento delle risonanze TE e TM. I risultati sono mostrati nel Capitolo 4. Nell'ambito dei plasmoni di superficie invece, abbiamo lavorato su un biosensore il cui obbiettivo finale è il riconoscimento di un antigene specifico nel sangue. I biosensori sono composti da un trasduttore che raccoglie la risposta biologica, e da un sistema elettronico che lo elabora e lo mostra all'utilizzatore. Abbiamo quindi lavorato sulla validazione ottica del protocollo di funzionalizzazione del biosensore, e l'attività è riportata nel Capitolo 5. Abbiamo analizzato un prototipo del trasduttore, controllando che ogni step di funzionalizzazione fosse riuscito. Successivamente, abbiamo svolto delle misure preliminari con l'obbiettivo di distinguere la fase di associazione dell'antigene con il rispettivo anticorpo. I risultati ottici sono stati quindi comparati con la caratterizzazione elettronica del campione, presentando un corretto accordo che conferma il buon funzionamento del sensore in analisi.

**Parole chiave:** onde di superficie; cristalli fotonici monodimensionali; plasmoni di superficie; onde superficiali di Bloch; superchiralità; dicroismo circolare, spettroscopie sensibili di polarizzazione; biosensori.

# Contents

# 1 Chapter one: Surface waves for molecular sensing and superchirality

In this Chapter surface waves are introduced. The ability of different platforms to sustain surface modes is exploited, then a comparison between Bloch Surface Waves and Surface Plasmon Polaritons is pointed out. The possibility with a one-dimensional photonic crystal of having both polarizations of surface modes at the same phase velocity is discussed, together with possible applications such as circular dichroism spectroscopy. Last, a novel design of one-dimensional photonic crystal for superchiral surface waves is described.

## 1.1. Bloch Surface Waves in one-dimensional photonic crystals

In optics, a surface wave is an electromagnetic wave that propagates along an interface between two dissimilar media with a field amplitude that exponentially decays away from the boundary. Due to its distinctive surface sensitivity and field localization characteristics, research on surface waves has been booming in the last decades. These characteristics have led to applications in near-field imaging,[1] sensing,[2] light-trapping,[3] and nano-guiding.[4] Surface waves have so far been studied in a wide range of materials and structure conditions. In this framework, Bloch Surface Waves (BSW) and Surface Plasmon Polaritons (SPP) are discussed in this Chapter. Bloch Surface Waves are generated at the surface of a truncated one-dimensional photonic crystal (1DPC), a periodic multilayer structure made of dielectric materials. Surface Plasmon Polaritons are instead sustained by metallic surfaces. Both kinds of surface waves are now well-established tools for molecular sensing and surface-enhanced spectroscopy as it will be pointed out along the manuscript. Photonic crystals are optical media where the refractive index changes periodically.[5] Many examples of photonic crystal structures can be found in nature[6] showing how a periodic structure can control the scattering of an incident light beam and inspiring in this way many studies and applications. The periodicity of the dielectric function can be along one, two or three dimensions, giving rise respectively to one-, two- and three-dimensional photonic crystals. One-dimensional photonic crystals (1DPCs) have the simplest structure but

keep features and advantages of photonic crystals in general. For example, they can be scaled and designed to work in a selected wavelength range, they show a photonic band gap and allow for localized modes if any defect is present in the structure. Those features allow for different applications of 1DPCs such as omnidirectional reflectors,[7] optical absorbers,[8] polarization selectors[9] and, as it will be discussed in Chapter 3 and 4, sensors exploiting Bloch Surface Waves.[10–18] A general 1DPCs could be seen as a stack of layers, homogeneous in the x-y plane and periodic in the z-direction, whose refractive index present a certain contrast, as sketched in Figure 1.1.
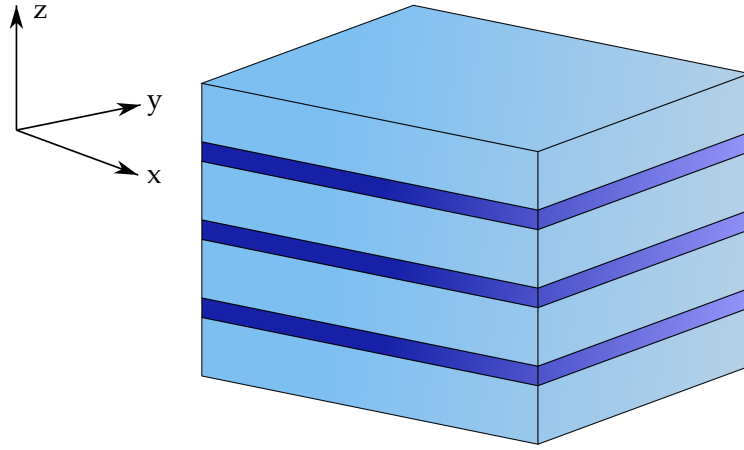


Figure 1.1 Sketch of a generic one-dimensional photonic crystal

Modes belonging to this kind of geometry can be described with the in-plane wavevector $\boldsymbol{k}_\parallel$, the wavevector along the z-direction $k_z$ and the band number $n$. Modes can be described using the Bloch form as in Equation 1.1:

$$\mathbf{H}_{n,k_z,\boldsymbol{k}_\parallel}(\boldsymbol{r}) = e^{i\boldsymbol{k}_\parallel \cdot \rho} e^{ik_z z} \boldsymbol{u}_{n,k_z,\boldsymbol{k}_\parallel}(z) \tag{1.1}$$

where $\mathbf{H}$ is the macroscopic magnetic field solution of the eigenvalue problem. Since we have a periodic structure in the z-direction, the $\boldsymbol{u}(z)$ function is as well periodic. $\boldsymbol{k}_\parallel$ can assume any value since the structure is homogeneous in the plane. $k_z$ has instead a finite interval of possible values, that is the one-dimensional Brillouin zone, whose dimension is $2\pi/a$, where $a$ is the periodicity of the crystal, over which $k_z$ is repeating. Let's start considering an electromagnetic wave propagating only along the z-direction, that means with $\boldsymbol{k}_\parallel = 0$, and a homogeneous structure without any index contrast. In this case permitted modes lie along the light line, that depends on the dielectric function of the considered material, as shown in Equation 1.2:

$$\omega(k) = \frac{ck_z}{\sqrt{\varepsilon}} \tag{1.2}$$

Where $c$ is the speed of light in vacuum and $\varepsilon$ the dielectric function of the material where light is propagating. If we consider now a crystal made by different materials (with different dielectric functions), what happens is that in the band structure a band

gap appears whose width depends on the contrast between the refractive index of the materials as depicted in Figure 1.2.
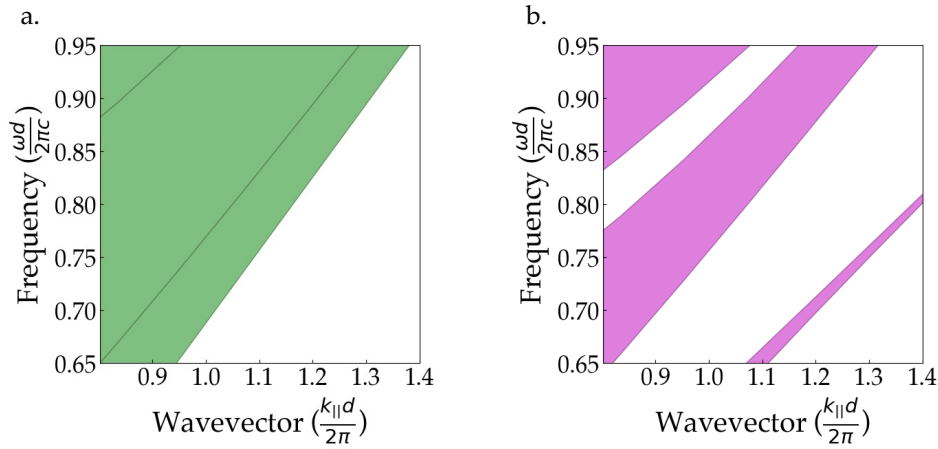
a.

b.

Figure 1.2. a) Band structure of a homogeneous system with refractive index n = 1.454. There is not any gap in the structure. The shadowed area represents the continuum of allowed bands. Solid lines denote band edges that are coincident. The bottom line is the light line. b) Band structure of a photonic crystal with a contrast $n_{high}/n_{low}$ = 1.4. The index contrast produces a band gap. Shadowed areas are bands where electromagnetic waves can propagate, while frequency in the band gap gives evanescent waves.

Panel a shows the band structure of a homogeneous system with a fixed refractive index n = 1.454, while panel b reports the band structure of a crystal whose refractive index contrast $n_{high}/n_{low}$ = 1.4. The band gap opens because, having now layers with high and low refractive index, different configurations of energy density of the modes exist. The energy density could be concentrated in the high index regions or in the low index regions and the difference between these two cases justifies the opening of the gap. Therefore, we can state that the band gap is the result of the periodicity and materials of the photonic crystal. It is worth noticing that there are no electromagnetic modes whose frequency belongs to the band gap. If we illuminate the crystal with a frequency in the band gap what we obtain is a complex wave vector. Modes are evanescent, with an amplitude that decays in the crystal. They can now be written using Equation 1.3:

$$\mathbf{H}_{n,k_z,\boldsymbol{k}_\parallel}(\boldsymbol{r}) = e^{ik_z z}\boldsymbol{u}(z)e^{-\kappa z} \tag{1.3}$$

Equation 1.3 corresponds to Equation 1.1 when $k_z$ is complex and its imaginary part gives the length scale $1/\kappa$ of the decay as sketched in Figure 1.3.
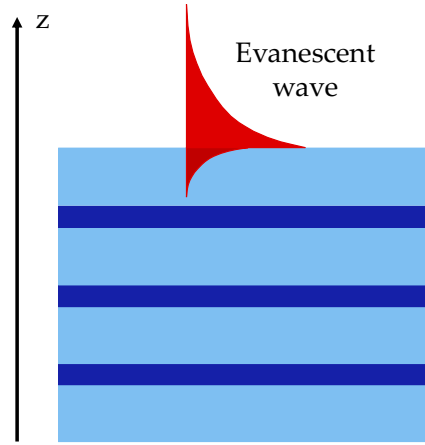
Figure 1.3. Sketch of the evanescent wave at the surface of a generic 1DPC

Even if states described by Equation 1.3 are solutions of the eigenvalue problem, when $z \to \pm\infty$ they become divergent, depending on the sign of $\kappa$. This means that it is not possible to excite those states an extended crystal in a physical way. A defect or an edge is needed to stop the exponential growth and to sustain the evanescent mode.[19] In this case a localized mode in the band gap is excited. If what breaks the exponential growth is the surface of a truncated crystal, we have the so-called surface modes. Localized states at the surface are possible only if two conditions are fulfilled: the frequency must be in the band gap and below the light line. This second condition is strictly related to the presence of the surface itself. In fact, to have an evanescent mode at the surface, it is necessary to illuminate the crystal with an angle that is above the critical angle from the Snell law, Equation 1.4:

$$n_{inc} \sin(\theta_{inc}) = n_{ext} \sin(\theta_{ext}) \tag{1.4}$$

In Equation 1.4, $n_{inc}$ is the refractive index of the incident medium and $\theta_{inc}$ is the angle of incidence of the illumination wave, taken with respect to the normal to the surface. $n_{ext}$ and $\theta_{ext}$ are the refractive index of the external medium and the angle of the transmitted beam referred to the normal to the surface. The critical angle is defined as the one at which the incoming beam is totally reflected, so $\sin(\theta_{ext}) = 1$. If the incident angle is above the critical one, corresponding to the total internal reflection condition, we have a complex $\mathbf{k}$ whose corresponding electromagnetic field decays exponentially away from the surface of the crystal. Total internal reflection also needs that $n_{ext} < n_{inc}$ meaning that the considered evanescent states are those below the light line. Let's now investigate the illumination with a fixed angle so that $\mathbf{k}_\parallel \neq 0$. In the $\mathbf{k}_\parallel = 0$ case the electric field is oriented in the x-y plane so if we consider two orthogonal polarizations, along x and along y, they are degenerate, reflecting the same symmetry of the crystal. Instead, if we consider a mode with $\mathbf{k}_\parallel \neq 0$ that property is no longer existing, so bands of modes polarized in the x direction (transverse magnetic TM) or in the y-z plane (transverse electric TE) are not degenerate. There is not any

relation between TE and TM dispersion relations so, in general, they have different frequencies.

## 1.2.  Numerical simulations

In this document, both experimental and numerical results are presented. From the simulation point of view, the transfer-matrix method (tmm) optics Python package[20] is used. The tmm suite can be used for computing reflection, transmission, absorption, and other relevant properties of thin and thick multilayer films. The analyzed structure must be homogeneous in the x-y plane while is a stack in the z-direction. The top and bottom layers are always set as semi-infinite, while all intermediate layers have defined thicknesses and can be set as "coherent" or "incoherent", a feature that we exploit during simulations of molecular binding on the surface since we deal with layers where light loses its coherence. It allows one to include layers with complex refractive index, so it is possible to consider absorbing films.  In a structure with N layers, the first (substrate) and the last (environment) are considered as semi-infinite and the code combines the amplitude of the waves propagating "forward" (from bottom to top) and "backward" (from top to bottom) with transmission and reflection coefficients at each interface. In this way the transfer matrix is calculated, and the code returns the transmitted and reflected power of a linear (s- or p-polarized) incident plane wave whose wavevector is in the x-z plane. Reflectivity curves and maps can be extrapolated with varying incident wavelength and angle of illumination.

## 1.3.  Design of a 1DPC

It is possible to evaluate the impact of the 1DPC design on modes' dispersion by considering for example the TE mode generated at the surface of a truncated periodic crystal and follow its evolution as the thickness of the high refractive index layer changes. Let's consider a 1DPC made by 3 layers of $SiO_2$ and 2 layers of $Ta_2O_5$ and let the thickness of the high refractive index layer $d_{high}$ vary between 70 nm and 130 nm with the $SiO_2$ layer with a fixed thickness of 310 nm as sketched in Figure 1.4.

Figure 1.4. Sketch of the simulated 1DPC

To simulate angular scans, the system is illuminated from the bottom with a light beam at 450 nm in the Kretschmann configuration. In this geometry, schematically represented in Fig. 1.5, the photonic crystal is in contact with the substrate (in this case BK7) and to generate a surface wave at the crystal/water interface an evanescent wave is created at the BK7/crystal interface exploiting the total internal reflection condition to have a complex wavevector inside the 1DPC.[21] Water is considered here as a typical external medium in a sensing experiment.
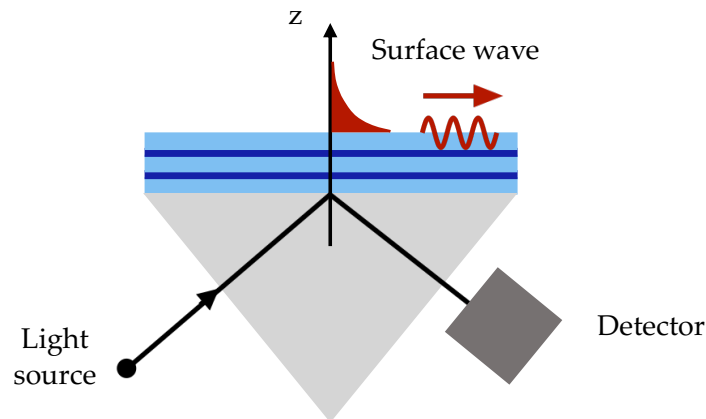


Figure 1.5. Sketch of the Kretschmann configuration

In this kind of configuration, the total reflected beam is collected, and the surface mode appears as a dip in the reflectivity signal. This is because what is collected is the radiation leakage of the surface mode, with also a contribution due to material absorption. We simulate dispersion relations of the TE mode and its angular scans obtained with different high refractive index layer thickness, as shown in Figure 1.6.
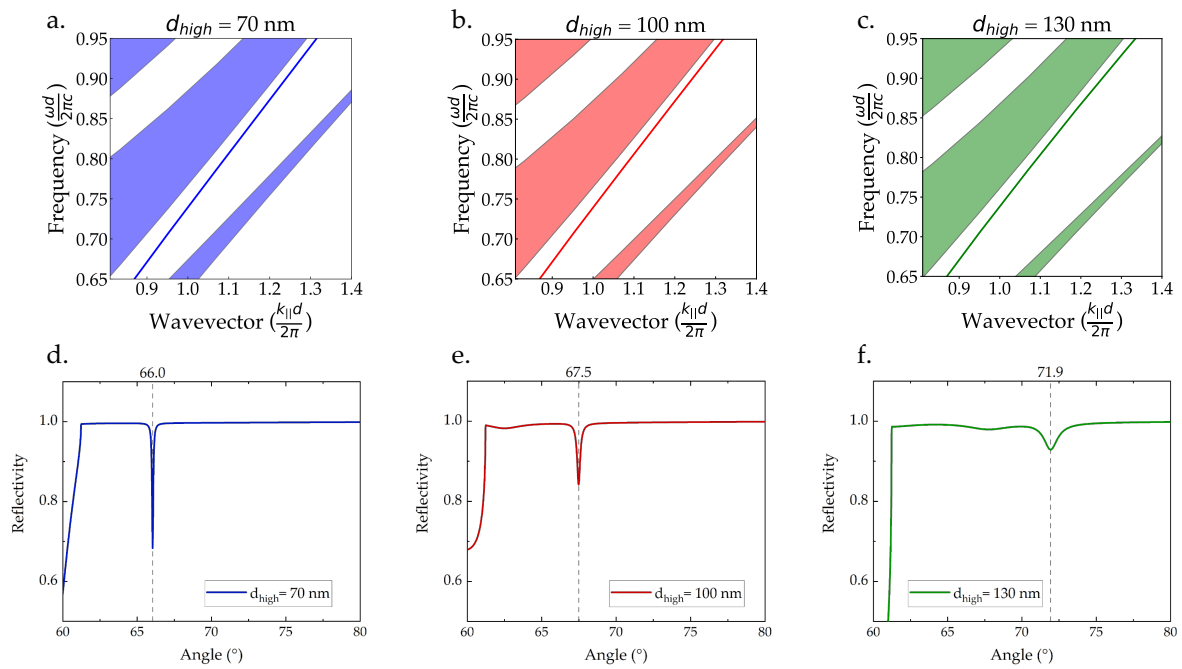
Figure 1.6. Panels a), b) and c): band structures and dispersion relations of the TE surface mode when the thickness of the high refractive index layers is respectively 70 nm, 100 nm and 130 nm. Panels d), e) and f): simulated angular scans at 450 nm wavelength when the thickness of the high refractive index layers is respectively 70 nm, 100 nm and 130 nm.

The thickness of the high refractive index layer acts on the angular position of the surface mode, as clear looking at angular scans in panels d, e and f for a fixed wavelength of 450 nm. Also, the shape of the mode is affected by the variation of this parameter since it depends on the distance from the band edge, so on radiation losses, and on the material losses. Another free parameter in the design of a 1DPC is the number of periods that constitute the platform but, differently from the optical path, this does not affect much the dispersion relations. In Figure 1.7 angular scans of the TE mode of a 1DPC as a function of the number of layers are shown.
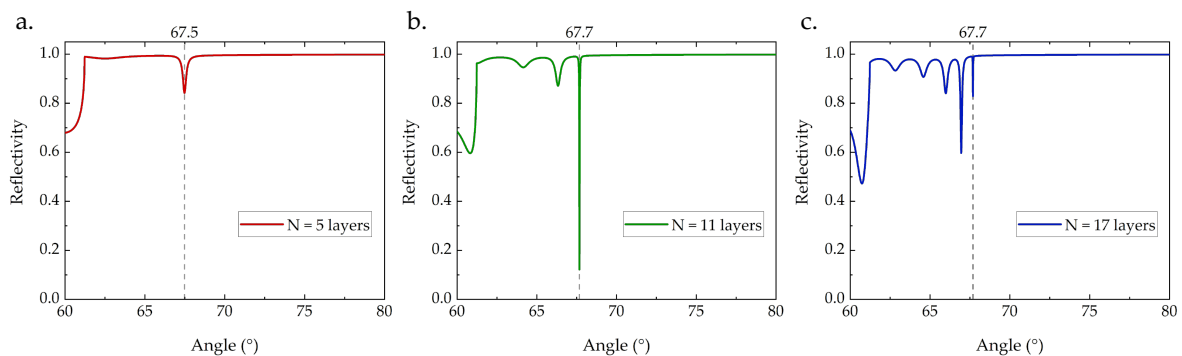


Figure 1.7. Comparison between surface modes sustained by 1DPC with different numbers of layers.

The thickness of the high and low periods is constant, with $d_{high}$ = 100 nm and $d_{low}$ = 310 nm. The shape of the resonance is the result of the combination of two parameters: radiation losses and coupling efficiency. The mode becomes more and

more narrow as we increase the number of layers, because we move from a condition of high radiation losses with 5 layers to a condition of minimum radiation losses considering 17 layers. The increase of the number of layers, however, ends in a lower coupling with radiation, so with 17 layers we have a narrow but weak resonance. The narrow and deep resonance obtained with 11 layers is the consequence of low radiation losses with a high coupling efficiency with the radiation. Instead, the excitation angle stays around the same angle, meaning that this is not a crucial parameter when acting on the spectral position of the resonance. Moreover, the addition of periods allows new guided modes that are visible as additional weaker dips in the spectra. Using these two examples, the importance of the structure of the platform for tuning resonances and the role played by every parameter in the crystal design should be clear. At this point it is interesting to consider both polarizations of the possible surface modes. As we pointed out in the discussion above, TE and TM modes have, in general, distinct dispersion relations. This means that TE and TM modes have different phase velocities during the propagation, and it is not possible to generate an arbitrary defined polarization state considering the combination of the two modes. In Figure 1.8 reflectivity maps for TE and TM modes belonging to a generic photonic crystal are reported, together with a cut at fixed wavelength. From here it is possible to evaluate how the different phase velocities of the modes translate into different angular and/or wavelength positions of the resonances.
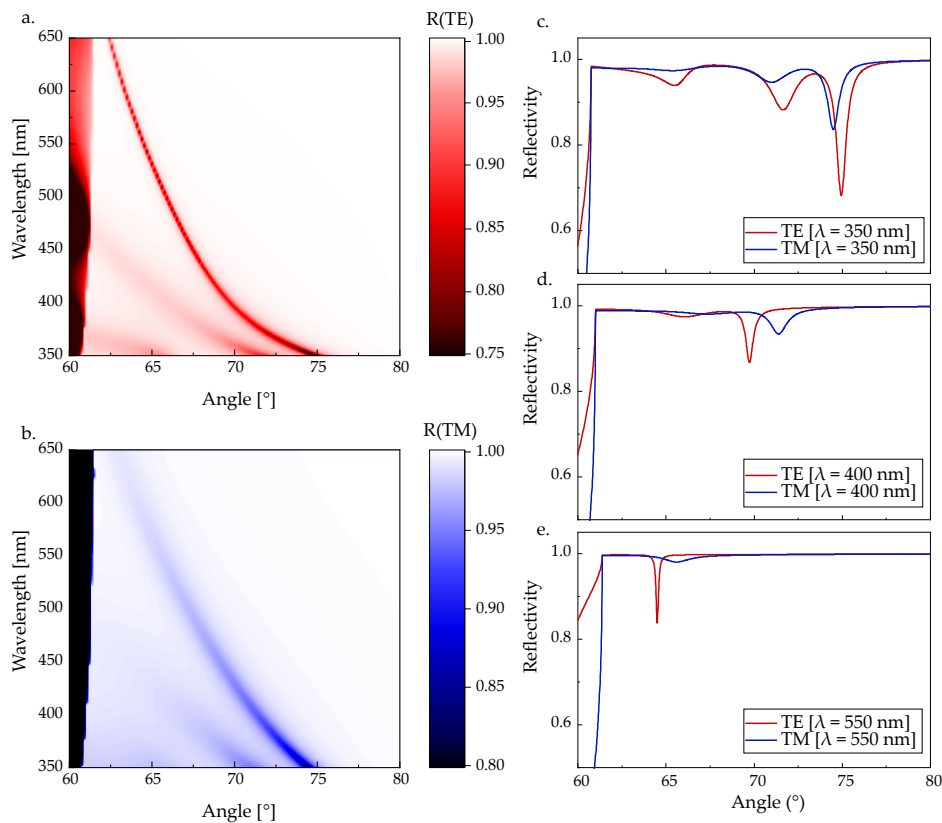
Figure 1.8. a) Reflectivity map when the generic 1DPC is illuminated with TE polarized light. The surface mode appears as a dip in the reflectivity signal. b) Reflectivity map when the 1DPC is illuminated with TM polarized light. c), d), e) cuts at fixed wavelengths of the TE and TM maps to show how surface modes do not have the same phase velocity, that means their relative position changes with wavelength.

Even if looking at reflectivity maps the two modes appear to have similar dispersions, scans at fixed wavelengths show that the relative position of the two resonances changes, demonstrating for a general case that it is not possible to control the polarization state of this combined surface mode over a broad spectral range. Therefore, with a perfectly periodic photonic crystal one could tune the spectral position of resonances but not generate a controlled polarization state of surface modes. A step further on this focus and in the surface-enhanced spectroscopy field would be the control over the BSW polarization state. This can be realized by engineering the structure of the photonic crystal to obtain overlapping dispersion relations for TE and TM modes. Surface modes have in this case the same phase velocity so TE and TM reflectivity measurements can be acquired simultaneously, at the same angle and at the same investigation wavelength, and the differential signal can be used for the investigation of the birefringence of a top molecular layer over a broadband spectral range, meaning that it would be possible, for example, to study the orientation of molecules anchored to the surface, as already customarily done in standard attenuated total internal reflection spectroscopy.[22,23] Moreover, the superposition of the TE and TM modes enables circular dichroism (CD) spectroscopy

since it is possible to combine them in a controlled way, to obtain for example circular or elliptical polarization states over a broadband spectral range.

## 1.4. Circular dichroism spectroscopy

Circular dichroism measures the differential absorption between left and right circularly polarized light, which represents one of the most common techniques to investigate chiral molecules. Chirality, the geometric lack of symmetry property of objects whose mirror images cannot be superimposed, is nowadays a hot topic because most biomolecules are chiral. The study of chirality could lead to applications in chemistry, molecular physics, medicine, and pharmacology.[24,25] In general, CD signals are very weak if compared to those of standard absorption spectroscopy, which makes the analysis of small amounts of chiral analytes extremely challenging. Moreover, the "extrinsic" chiral signal that could be generated by any broken symmetry in the geometry of the optical system can overwhelm the "intrinsic" signal coming from molecules.[26-28] This makes the design and commissioning of chiroptical setups and platforms extremely demanding. Recently, novel "superchiral" approaches have been introduced to enhance the CD signal by engineering the optical chirality of the electromagnetic field with the use of nanostructured systems.[29,30] The optical chirality is an electromagnetic field property defined as in Equation 1.5:

$$C = -\frac{\varepsilon_0 \omega}{2} Im(\widetilde{\boldsymbol{E}}^* \cdot \widetilde{\boldsymbol{B}})  \tag{1.5}$$

This quantity represents the helicity of a general electromagnetic field, and it is related to local electric ($\widetilde{\boldsymbol{E}}$) and magnetic ($\widetilde{\boldsymbol{B}}$) fields at the molecule. This can be deduced by looking at the absorption formula of a molecule for right (-) and left (+) circular polarized light, see Equation 1.6 (which is valid in a dipolar approximation):

$$A^{\pm} = \frac{\omega}{2}\left(\alpha'' |\widetilde{\boldsymbol{E}}|^2 + \chi'' |\widetilde{\boldsymbol{B}}|^2\right) \pm G'' \omega \, Im(\widetilde{\boldsymbol{E}}^* \cdot \widetilde{\boldsymbol{B}})  \tag{1.6}$$

The term $\omega$ represents the frequency of the electromagnetic field, $\alpha''$ is the imaginary part of the electric polarizability, $\chi''$ is the imaginary part of the magnetic susceptibility and $G''$ is the isotropic mixed electric-magnetic dipole polarizability. The first term does not involve chirality and refers to the electric dipole moment and its interaction with the electric field while the second term, that can be neglected since it is comparably small with respect to the previous one, represents the magnetic dipole moment and also does not depend on chirality. The last term considers chirality involving the interaction between the electric dipole moment and the magnetic field and *viceversa*. CD measures the differential absorption between those polarization-dependent absorptions through the dissymmetry factor, defined in Equation 1.7:

$$g \equiv 2 \frac{A^+ - A^-}{A^+ + A^-} \tag{1.7}$$

Putting the absorption formula into the g expression, it is possible to recover a form of the dissymmetry factor that can be split into molecular and light properties, as expressed in Equation 1.8:

$$g = -\left(\frac{G''}{\alpha''}\right)\left(\frac{2C}{\omega U_e}\right) \tag{1.8}$$

The first term contains only parameters dependent on the chemical properties of the molecule under investigation, while the second term is completely related to electromagnetic field properties that could be engineered. There are then two approaches for enhancing the chiral signal from the optical point of view: reducing the time-average electric energy density $U_e$ or increasing the optical chirality $C$. We focus on the optical chirality, whose value could be enhanced over the value obtained with plane waves, giving rise to a so called "superchiral" surface wave. Even if the term superchiral was originally used by the plasmonic community to indicate electromagnetic field configurations that allow one to detect larger dissymmetry factors from chiral molecules with respect to plane wave illumination, nowadays it is commonly used to describe electromagnetic fields exhibiting optical chirality larger than that of circularly polarized plane waves.

Thus, CD signals are defined as the differential absorptivity between left and right handedness, as reported in Equation 1.9:

$$\Delta\mathcal{A} := \mathcal{A}^+ - \mathcal{A}^- = log\left(\frac{I^-}{I^+}\right) \tag{1.9}$$

where $\mathcal{A}$ indicates the absorptivity while $I^\pm$ is the left/right polarized light intensity coming from the analyzed medium. This relation can be obtained starting from the Beer's law, stated in Equation 1.10, describing the attenuation of light intensity in a medium:

$$I = I_0 10^{-\epsilon l c_{mol}} \tag{1.10}$$

where $\epsilon$ is the molar extinction coefficient, $l$ is the path length and $c_{mol}$ is the concentration of the chiral analytes in moles per liter. From this expression it is possible to define the absorptivity as in Equation 1.11:

$$\mathcal{A} := \epsilon l c_{mol} = log\left(\frac{I_0}{I}\right) \tag{1.11}$$

This expression will be then exploited in Chapter 3 when investigating the molecular solution with a spectrophotometer to extract the molar extinction coefficient.

Another way to measure the CD signal is by using the ellipticity $\theta$, defined as in Equation 1.12:

$$\theta(\text{rad}) = \frac{\sqrt{I^-} - \sqrt{I^+}}{\sqrt{I^-} + \sqrt{I^+}} \tag{1.12}$$

where $I^\pm$ is the left/right polarized light intensity coming from the analyzed medium. Combining this definition with the absorptivity expression, it is possible to express the ellipticity as in Equation 1.13:

$$\theta(\text{rad}) \approx \Delta\mathcal{A}\frac{\ln(10)}{4} \tag{1.13}$$

which is valid only for small values of $\Delta\mathcal{A}$. It is possible then to convert this parameter into millidegrees, obtaining Equation 1.14:

$$\theta(\text{mdeg}) \approx 32982 \cdot \Delta\mathcal{A} \tag{1.13}$$

Millidegrees are the standard unit of measurements of circular dichroism signals and the common limit of detection for standard CD spectroscopies is around 1 mdeg.[31]

## 1.5. Our novel design of a one-dimensional photonic crystal

Many efforts have been devoted to exploit superchirality with approaches based on both metallic and dielectric nanostructures that generate hotspots of enhanced optical chirality.[32,33,42–51,34–41] In this framework, we propose a novel design of a 1DPC that allows for the generation of "superchiral" surface waves.[52] The design allows for the enhancement of the CD signal by more than two order of magnitudes (possibly down to the monolayer sensitivity), with a broadband spectral range and uniform surface fields, not limited to confined hot spots. The peculiar feature of the proposed 1DPC is the addition of a defect on top of an otherwise perfectly periodic crystal. This allows for the superposition of the dispersion relations of the TE and TM surface modes over a broadband spectral range from the visible up to the near UV. Since the modes keep the same phase velocity during propagation the polarization state obtained combining the two modes is always well-defined. This combination of surface modes is what generates the superchiral wave that would be then employed for CD measurements. In particular, the 1DPC originally proposed was made by 13 layers of alternating $SiO_2$ and $Ta_2O_5$ as shown in Figure 1.9.
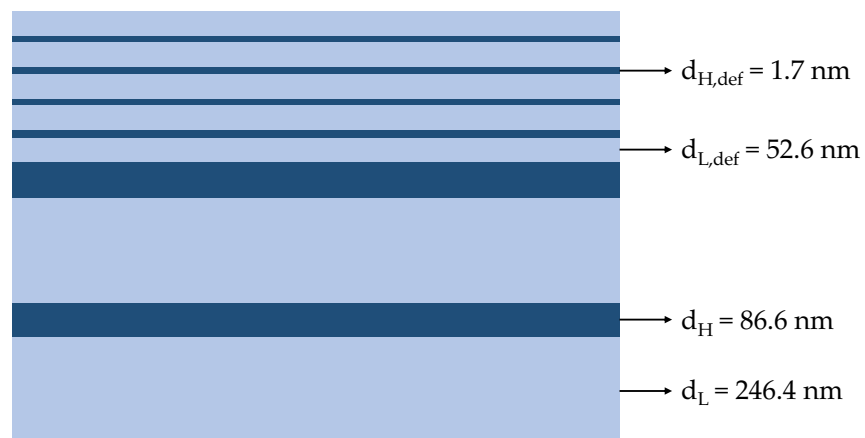
Figure 1.9. Sketch of the design of the 1DPC proposed in Ref. 52 for superchiral waves generation

In this design, 4 layers constitute the main body of the crystal while the remaining 9 form the surface defect that allows for mode superposition. A further step in the design of this platform is to reduce the number of layers of the defect keeping the same optical performance. For this reason, we propose a novel platform made by the same materials as in Ref. 52 but constituted by 7 layers: the surface defect is substituted by a high refractive index inclusion inside the upper low refractive index layer and thicknesses are adjusted to retrieve the TE-TM dispersion relations overlap.[53] In Figure 1.10 a sketch of the structure that maximizes the overlap of TE and TM modes in an aqueous-based environment is reported.
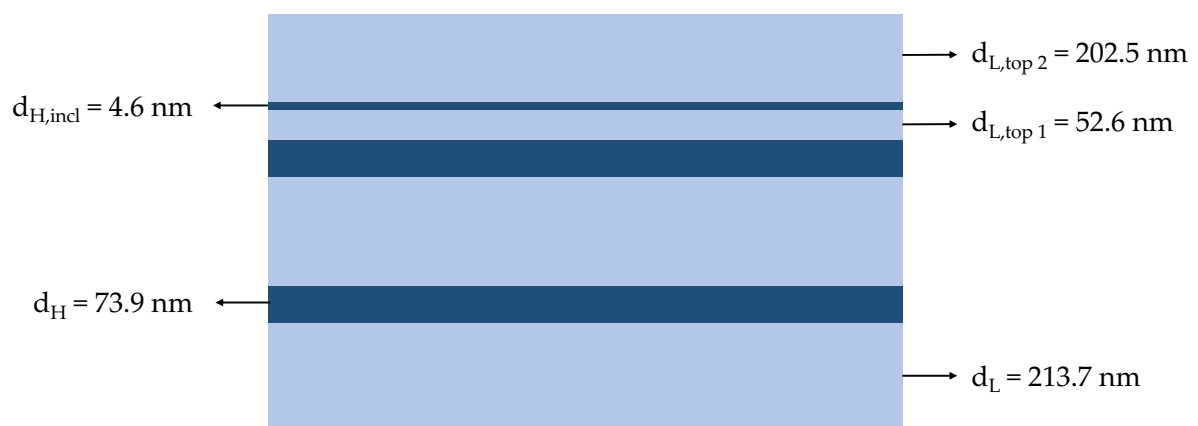


Figure 1.10. Sketch of the 1DPC proposed in Ref. 53 for superchiral waves generation with the specific goal to reduce the number of layers with respect to Ref. 52.

The optical constants of the chosen materials are retrieved from the literature.[54,55] The system is simulated using a Fresnel reflectivity model with the transfer matrix method, to capture the momentum matching with Kretschmann configuration.[56] We report in Figure 1.11 the simulated TE and TM reflectivity maps as a function of the illumination wavelength, set between 440 nm and 550 nm to focus on the visible part of the spectrum, and the angle of incidence of the illuminating beam onto a BK7 substrate.
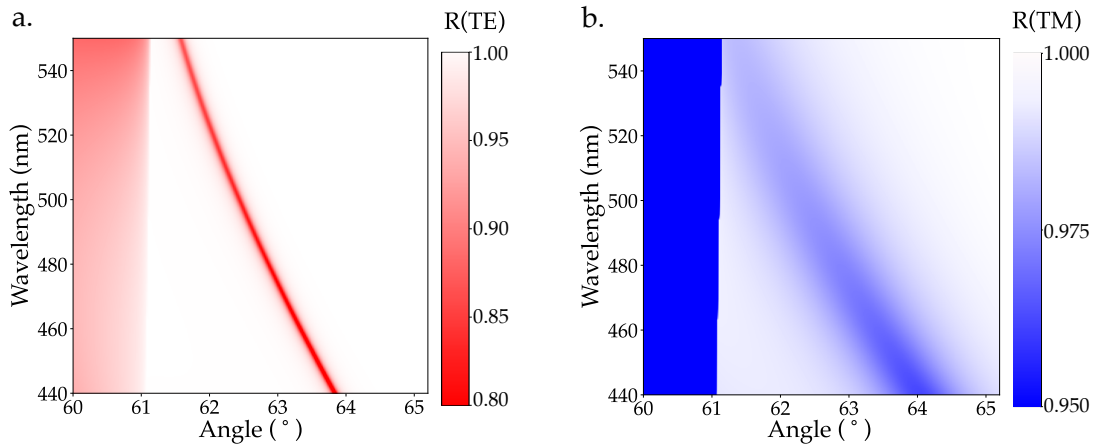
Figure 1.11. Simulated reflectivity maps for a) TE and b) TM illumination condition

Those maps highlight the different shape of the two modes, with the TE that appears narrow and deep while the TM shows up only like a halo. This can be justified looking at the dispersion relations in the band diagram of the two modes, shown in Figure 1.12.
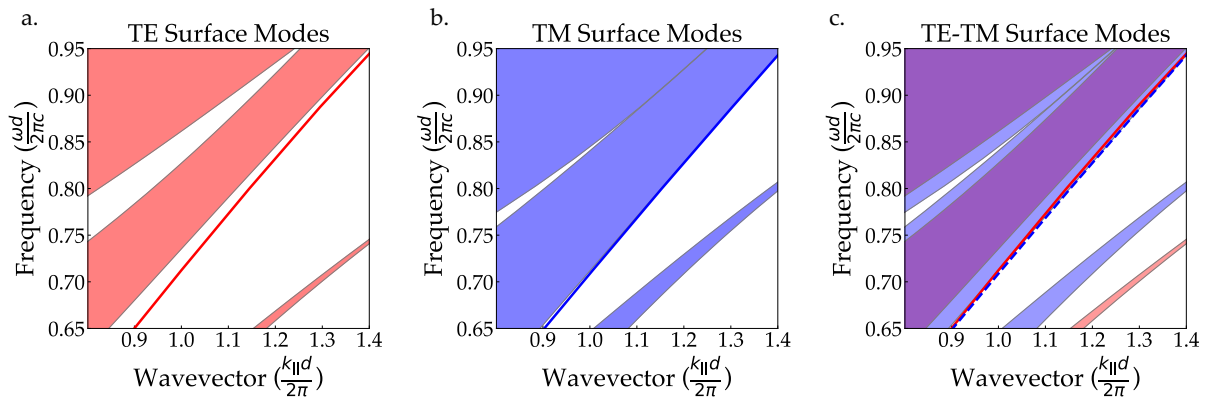


Figure 1.12. Band structures with dispersion relation of the surface mode for a) TE polarization and b) TM polarization. c) Graphically overlap of panel a) and b) to show surface modes superposition over the spectral range of interest.

The TM dispersion relation is shown in panel b and appears closer to the band edge with respect to the TE one, in panel a, meaning that we have more radiation losses and so a broader mode. From panel c the perfect overlap between dispersion relations is also evident, which translates into a superposition of surface modes when comparing reflectivity signals. One can look at reflectivity fixing one between the wavelength and the angle and notice that, in both cases, TE and TM features are overlapped. This characteristic is kept over a broadband spectral range and consequently for different angles, as shown in Figure 1.13 fixing three different wavelengths of investigation.
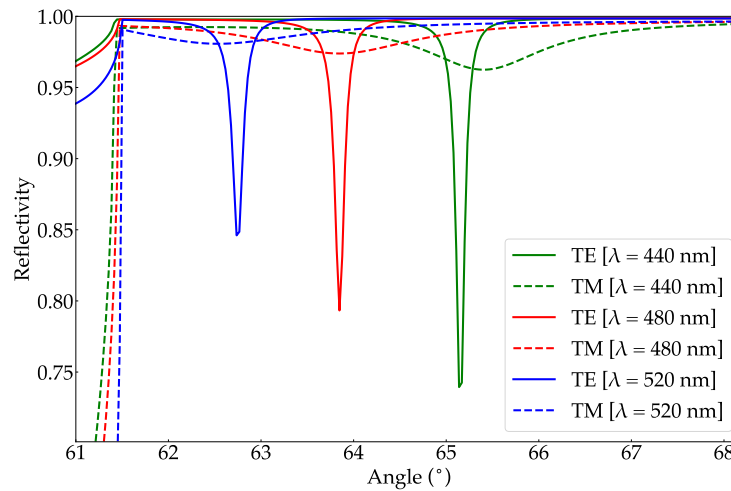
Figure 1.13. TE and TM reflectivity signals at different fixed wavelengths.

This extended overlap allows e.g. one to define the polarization state of the combination of the modes as circular (elliptical) and keep it even if the investigation wavelength changes. The optical performance of this platform is aligned with the request of optical chirality enhancement, keeping it slightly less than a factor $10^2$. This is reported in Figure 1.14, where the ratio between the predicted optical chirality of the platform C and the correspondent value that can obtained with plane wave illumination $C_{pw}$ is shown for different wavelengths.
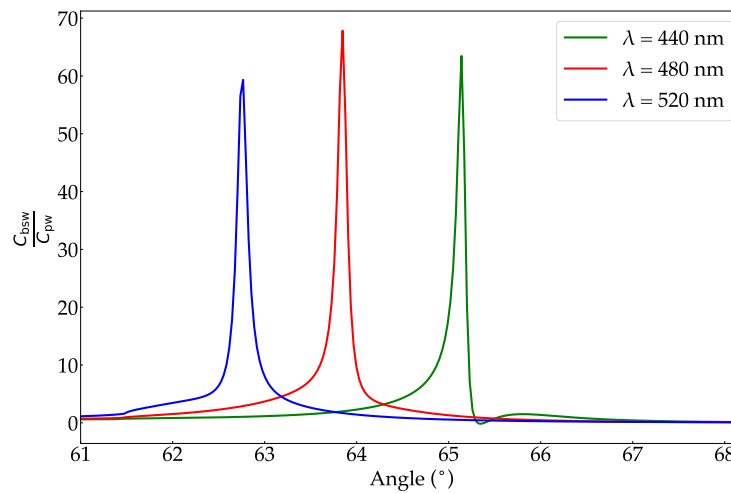


Figure 1.14. Optical chirality enhancement with respect to plane wave illumination. Results at different wavelengths are shown.

With this design we keep the target optical performance, so the platform is employed for preliminary chiral measurements and other applications described in the next Chapters that exploit surface mode polarization control.

## 1.6.   Surface Plasmon Polaritons

Bloch Waves are complementary to another well-known kind of surface waves: Surface Plasmon Polaritons. SPPs are electromagnetic surface waves resonantly coupled to collective oscillations of the electronic charge at the surface of a metal. There are two conditions for the excitation of SPPs: the first is that the sum of the dielectric functions of the incident media $\varepsilon_1(\omega)$ and external media $\varepsilon_2(\omega)$ is lower than zero, see Equation 1.14a, and the second is that the product of the dielectric functions is negative, see Equation 1.14b.

$$\varepsilon_1(\omega) + \varepsilon_2(\omega) < 0 \tag{1.14a}$$

$$\varepsilon_1(\omega) \cdot \varepsilon_2(\omega) < 0 \tag{1.14b}$$

The above conditions are impossible to satisfy with two materials with a real positive dielectric function. One of the two must have a negative dielectric constant, making metals perfect candidates. The optical response of a metal can be described using different models, the simplest is the Drude one. This description assumes a gas of free electrons (i.e., with negligible scattering) moving against a fixed background of positive ion cores and works for alkali metals up to the near UV and for many transition metals up to the visible – near IR. Looking at how those free electrons respond to a time-harmonic field it is possible to define a dielectric constant as in Equation 1.15:

$$\varepsilon_{free}(\omega) = 1 - \frac{\omega_p^2}{\omega^2} \tag{1.15}$$

where $\omega_p = \frac{nq_e^2}{\varepsilon_0 m_e}$, called plasma frequency, is dependent on the mass and charge of electrons $m_e$ and $q_e$ and on the number of carriers per unit volume $n$. The free electron dielectric function is real and $\omega_p$ represents the frequency below which electrons oscillate out of phase with the optical field. Optical frequencies are below $\omega_p$ for metals, meaning a negative $\varepsilon$ that describes their large reflectivity. Instead, losses due to scattering are missing in this model, so it is necessary to add some terms to the dielectric function that consider this damping effect. The Drude-Sommerfeld model includes electron-electron and electron-phonon scattering and gives the complex dielectric function of Equation 1.16:

$$\varepsilon_{Drude-Sommerfeld}(\omega) = 1 - \frac{\omega_p^2}{\omega^2 + \Gamma^2} + i \frac{\Gamma \, \omega_p^2}{\omega^2 + \Gamma^2} \tag{1.16}$$

$\omega_p$ is the plasma frequency of the Drude model but now a viscous damping term linked to $\Gamma$, is also considered. The significant imaginary part is related to Ohmic losses and therefore to a certain penetration of the optical field into the material. Even this model is not complete since it does not include interband transitions. In the Drude-

Lorentz model these transitions are taken into account as oscillations of bound electrons, and the additional term in the dielectric function is described by Equation 1.17:

$$\varepsilon_{Lorentz}(\omega) = 1 + \frac{\widetilde{\omega}_p^2}{(\omega_0^2 - \omega^2) - i\gamma\omega} \qquad (1.17)$$

where $\widetilde{\omega}_p$ is now a term with the same features of the plasma frequency, $\omega_0$ approximates the natural frequency and $\gamma$ is related with damping of bound electrons. With these models we are now able to describe the experimental data of metallic materials. For plasmonic applications we look for spectral regions without interband transitions where electrons can be considered as free so, for example, gold can be optimally used in the red – near IR part of the spectrum. A metal-dielectric interface can in principle guide a surface plasmon but there is also a condition on the illumination geometry to fulfill to excite an evanescent surface wave. The illumination beam must be TM polarized, because a TE polarized wave is not coupled to the electron plasma oscillations at the metal surface. Since SPPs have an evanescent behavior at the surface, they must be described with a complex wavevector, where $k_z$ is complex as in the case of BSWs. For $k_x$ conservation though, SPPs cannot be excited by far field illumination, but it is possible to excite them on the surface, for example, with the same Kretschmann configuration described for BSWs excitation. In this geometry, the thickness of the gold layer represents a key parameter in plasmon excitation since it determines the coupling efficiency and the radiation losses of the mode. Figure 1.15 shows with numerical simulations how the shape of the plasmon resonance feature varies as a function of the thickness of the gold layer (refractive index of gold taken from Ref. 57) on a BK7 substrate (refractive index taken from SCHOTT glass data sheets). The wavelength is fixed at 680 nm.
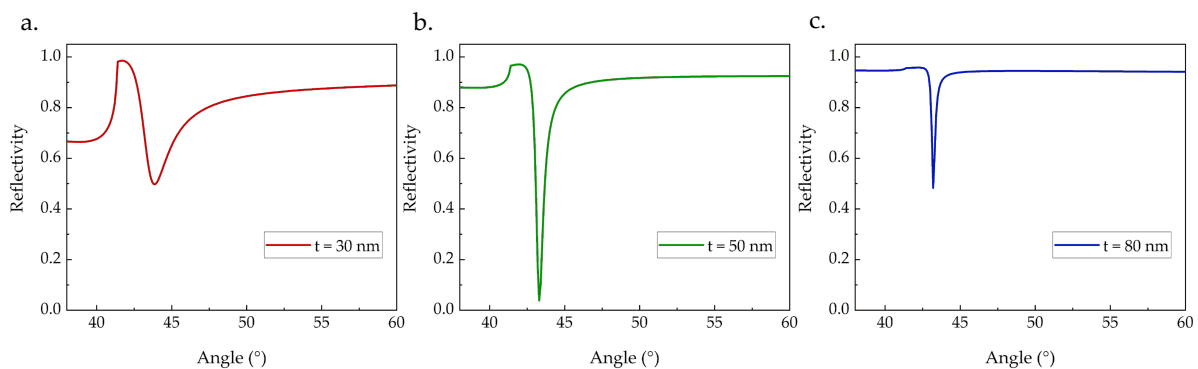


Figure 1.15.Surface plasmon resonance feature as a function of the thickness of the Au metallic layer: a) 30 nm, b) 50 nm (optimal condition), c) 80 nm

A thickness of 30 nm represents a layer too thin, where a strong radiation damping causes a broad feature, with a lot of leakage radiation into the glass substrate. Then, a thick layer of 80 nm is considered. In this case even if the resonance is narrower, the

excitation is again inefficient because only a small portion of the evanescent tale reaches the gold-BK7 interface, and this is reflected in the weakness of the resonance excitation. The optimal condition, with a narrow and deep near-to-zero resonance, is reached with a gold thickness of about 50 nm, making this thickness the standard for gold layers for sensing. Once set the ideal thickness of the gold layer, it is necessary to fix the best working wavelength that gives the highest sensitivity to local refractive index variations. A sensitivity analysis as a function of the excitation wavelength is shown in panel a of Figure 1.16.

a.

b.

c.
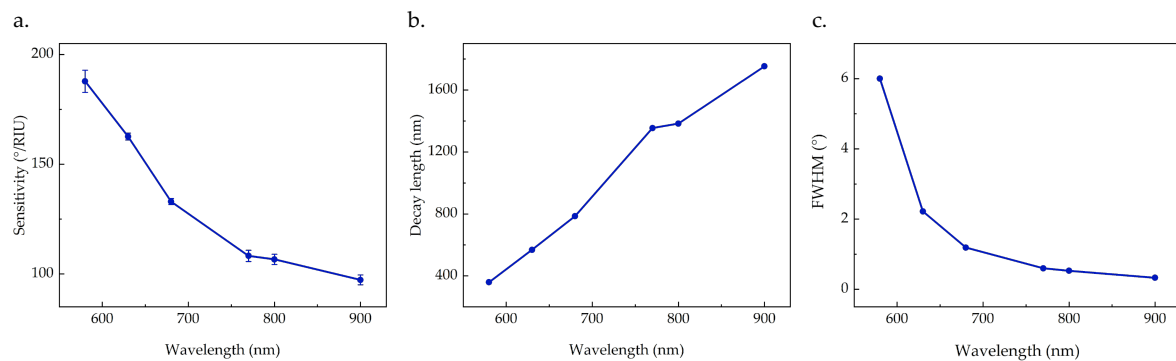
Figure 1.16. a) sensitivity of a 50 nm gold layer platform as function of the illumination wavelength. b) Decay length of the evanescent field at the surface of the gold layer as function of the illumination wavelength. c) FWHM of the surface mode as a function of the wavelength.

Angular scans at fixed wavelength are simulated setting the thickness of the gold layer at 50 nm. The refractive index is varied between 1.332 and 1.335 and the shift of the position of the minimum of the resonance is tracked. Then, using a linear fit, the sensitivity in °/RIU is extracted and plotted as a function of the wavelength. From panel a of Figure 16 one can notice that the best sensitivity is obtained at short wavelengths in the red region of the spectrum. This result is consistent if one also looks at the decay length of the evanescent field at the surface of the metallic layer, as in panel b of Figure 1.16. The decay length of the field has an opposite behavior with respect to the sensitivity, increasing as the illumination wavelength increases. The last investigated parameter for the optimization of the acquisition of SPPs is the full width at half maximum (FWHM) of the resonance, shown in panel c of Figure 1.16. Narrower surface modes allow for a better tracking of the surface mode, so in this case the best condition would be at longer wavelengths, a behavior in contrast with the previous parameters.

For these reasons, we experimentally employed a gold sample whose thickness is around 50 nm, while we choose as a compromise between the presented parameters an investigation wavelength around 680 nm.

## 1.7.   Bloch Surface Waves vs Surface Plasmon Polaritons

As discussed, a platform that can sustain SPP needs a metallic layer, gold is a common choice, while BSWs are sustained by dielectric platforms. Even if the structure generating those surface waves is different, BSW and SPP share some common points, starting from being both evanescent surface waves whose excitation can be observed as a dip in the reflectivity spectrum as shown in Figure 1.17.
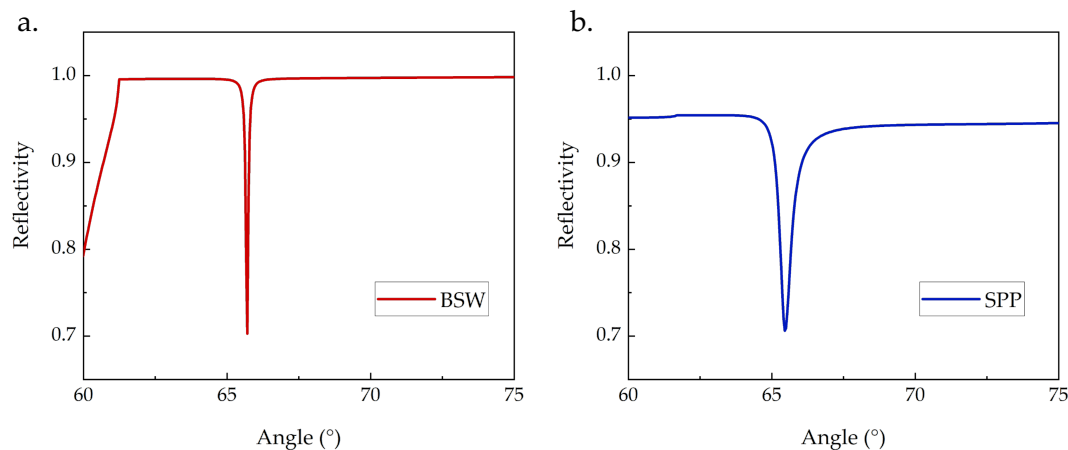


Figure 1.17. Comparison between a BSW and a SPP in specific conditions to have similar features to be compared.

Panel a. shows a surface mode sustained by a 1DPC made by 5 layers of alternating $SiO_2$ and $Ta_2O_5$ (refractive index of both materials taken from Ref. 55) on a BK7 substrate (refractive index taken from SCHOTT glass data sheets) in an aqueous environment. The thickness of the high refractive index layer is set to 60 nm while the thickness of the low refractive index layers is set to 310 nm. The polarization of illumination is set to be TE and the wavelength of investigation to 450 nm. Panel b shows instead a SPP obtained by putting 85 nm of gold (refractive index of gold taken from Ref. 57) on a BK7 substrate in aqueous environment. The polarization of illumination is the TM one, otherwise no plasmon can be excited, and the wavelength of investigation is set to 850 nm. Parameters are precisely chosen to obtain similar features to be compared. A field enhancement at the interface between the platform and the external medium is available in both cases, making those systems a well-established tool for surface-enhanced spectroscopies for analytes located at their surface.[5,52,58–64] The surface examination can be performed in the angular or in the spectral domain. In the angular investigation, the illuminating wavelength is fixed and a dip is observed in the reflectivity angular scan.[10–16,18] In a similar way, in the wavelength interrogation the angle of illumination is set near a resonant excitation angle and the reflectivity signal is collected as a function of the wavelength, with a dip corresponding to the resonance.[14,58,60,65–67] The first difference is then the polarization of the illuminating beam, with the photonic crystal able to sustain both TE and the TM modes while the gold layer is only compatible with the TM configuration to be coupled

with electron plasma oscillations at the surface.[68] So, only with BSWs it is possible to perform polarization-resolved spectroscopies studying e.g. the birefringence of a molecular layer as will be shown in Chapter 4. On the other side, to obtain a sharp BSW feature one must work on the design of the platform acting on the number of layers and on their thicknesses while with gold the optimum condition for SPP excitation is well-established. Here in fact the choice of 85 nm gives a worse performance with respect to the optimal one. The spectral position of the surface modes is also different, with the BSW excited also in the blue/UV while the SPP illuminated with NIR light, meaning that only BSWs allow for the resonant excitation of molecular electronic transitions. Going down to the UV is possible with a careful choice of materials, since non absorbing media with high purity level are needed.

# 2    Chapter two: The experimental setup

The two main experimental setups are described in this Chapter. The first one, based at Politecnico di Milano, allows for single wavelength reflectivity scans and circular dichroism measurements. Alignment criticalities are here discussed together with the design and realization of the optofluidic system for measurements with solutions. The second setup, based at the Austrian Institute of Technology of Tulln, enables for polychromatic light illumination and polarization resolved TE/TM signals acquisitions.

## 2.1.   Single-wavelength illumination setup

The setup assembled for single wavelength investigation of samples is based at Politecnico di Milano and depicted in Figure 2.1. It is used for the acquisition of reflectivity angular scans at fixed wavelength of 1DPCs and gold samples.
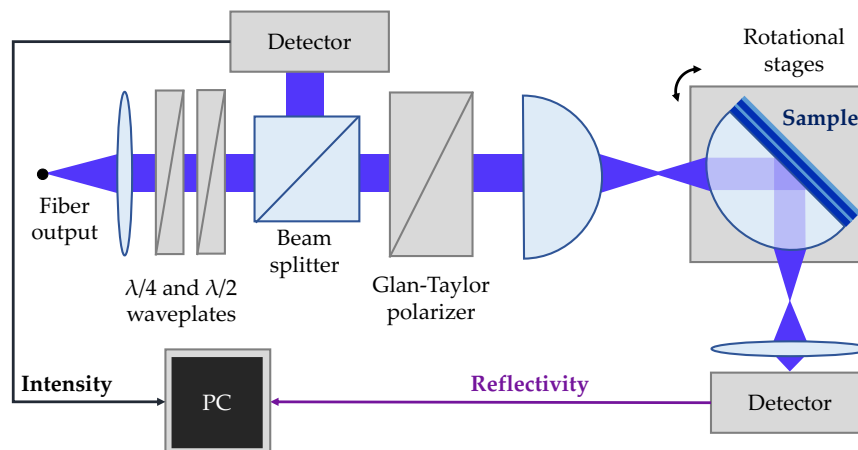


Figure 2.1. Sketch of the single-wavelength illumination setup

The illumination comes from different fiber-coupled laser sources. Photonic crystal measurements were performed in the visible range using a laser diode whose central wavelength is at 405 nm. For the plasmonic investigation described in Chapter 5, a high power automated femtosecond Ti:Sapphire laser is used coupled with a monomodal fiber. This laser can work between 680 nm and 1040 nm, while the region of interest is between 680 nm and 900 nm. The output power is maximum around

800 nm, making this the most stable region of work, while edges of the operating range have less stability introducing more noise in the illumination beam. The fiber output is collimated with a lens and propagates through a combination of a quarter waveplate and a half waveplate to maximize the intensity of the beam due to polarization changes in the fiber. Then a 50:50 beam splitter allows for the collection of the original beam before any interaction with optical elements. This signal is collected with a switchable gain silicon photodiode detector (model PDA36A-EC by Thorlabs), and it is used both to check the stability of the illuminating light and for measurements normalization. The transmitted beam instead reaches a Glan-Taylor polarizer that allows to set the polarization of the incident light and switch it between TE and TM conditions. Then, since samples are mounted on a semicylindrical BK7 substrate, which also acts as a lens, a first semicylindrical BK7 element is positioned to null the focusing effect and to ensure a collimated beam inside the sample, to have a well-defined angle of excitation of the surface wave and to ensure to work always at normal illumination of the surface. To guarantee precision in the alignment of the setup, this first semicylindrical element is provided with different degrees of freedom as shown in Figure 2.2.
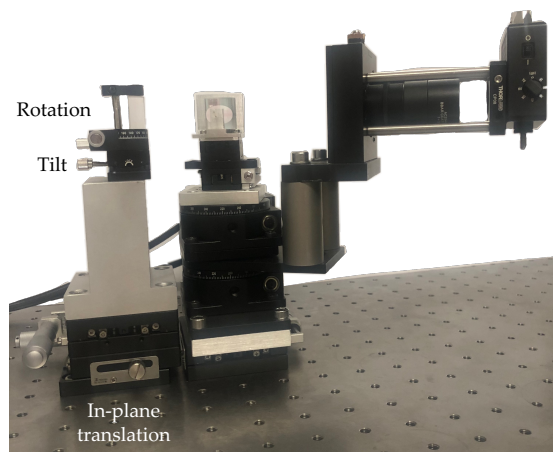


Figure 2.2. First semicylindrical lens platform with implemented degrees of freedom

Two micrometric-translators allow for the in-plane positioning to hit the center of the cylindrical element. A tilter and a mechanical rotational stage are also added to ensure normal incidence of the incoming beam. The entire set of degrees of freedom that we can control enables the precise alignment of the first lens with the second one that hosts the sample. The sample stage is designed to have several degrees of freedom, highlighted in Figure 2.3: two translational degrees, two rotational degrees around an axis perpendicular to the optical table that allow for the collection of the internal reflected signal in a θ-2θ configuration and one rotational degree to correct the tilt of the sample.
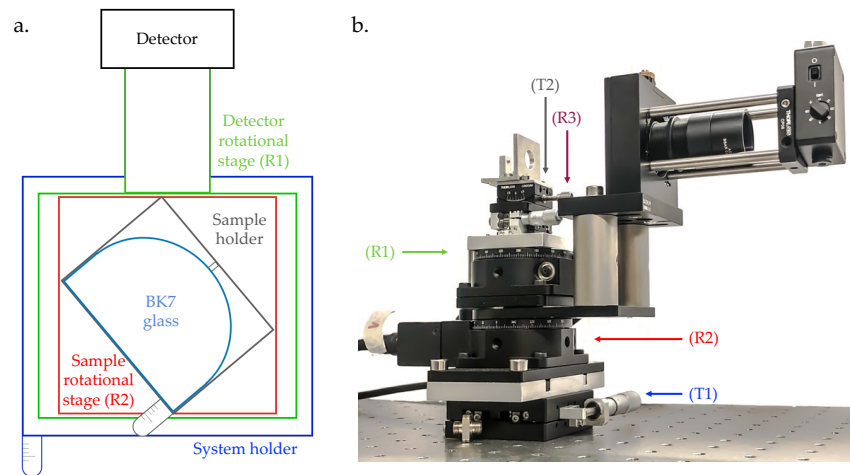
Figure 2.3. a) Scheme of the degrees if freedom of the sample stage. b) Picture of the experimental setup with highlighted degree of freedom of the sample stage

The translational stage (T1) allows for the motion in the direction perpendicular to the incident light and it used to align the system with respect to the incident beam. The rotational stages (R1) and (R2) are used to measure in a θ-2θ configuration the reflectivity signal. The excitation of surface waves happens then in the Kretschmann configuration: the light beam reaches the BK7 coupling prism, where the target sample is optically matched using immersion oil (n=1.51) and it is reflected back by the sample itself into the detection arm. The translator (T2) acts only on the sample holder and allows motion in the direction perpendicular to the flat face of the semicylindrical prism. The holder has been home designed to keep the sample fixed during the measurement, so there is a Teflon screw that pushes the sample against the back wall as shown in Figure 2.4.
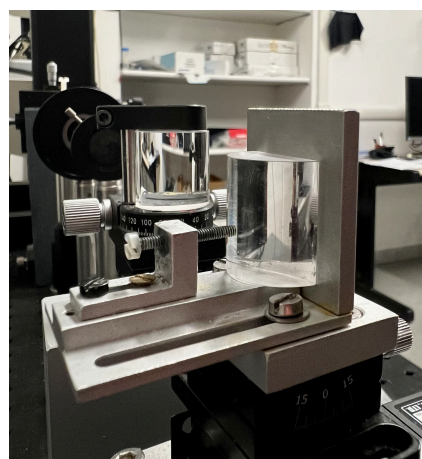


Figure 2.4. Picture of the home-designed sample holder. The screw pushes the sample against the back wall to fix it during rotations.

This last part is where the sample faces air, so where the propagating light is totally reflected. The translation of the sample holder allows one to move the center of

rotation of the sample. A good alignment occurs when the center of rotation of the sample corresponds to the axis around which stages are rotating and this matches also the point illuminated by the incident beam, as shown in Figure 2.5.
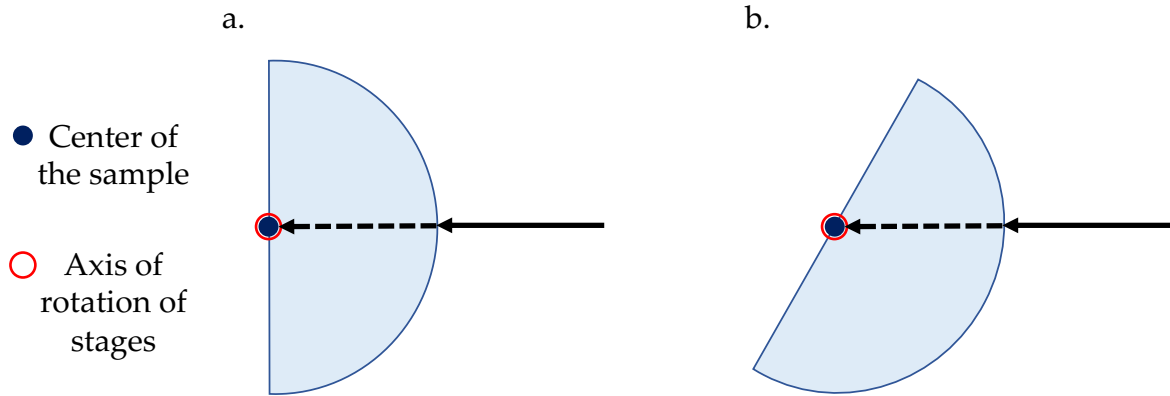


Figure 2.5. a) If the alignment is good, the incoming light hits the center of rotation of the semi-cylindrical sample. b) Also, when rotation occurs, the beam is not deviated and hits the center of rotation of the BK7 glass.

In this configuration, the centers of rotations of the prism and the stages (R1) and (R2) are correspondent to the illuminating point and this ensures that light is always reflected by the same site during rotations. When the entire sample stage is not properly aligned through the (T1) translator, an off-axis laser misalignment can occur. In this case the position where the laser hits the sample changes during the rotation as shown in Figure 2.6.
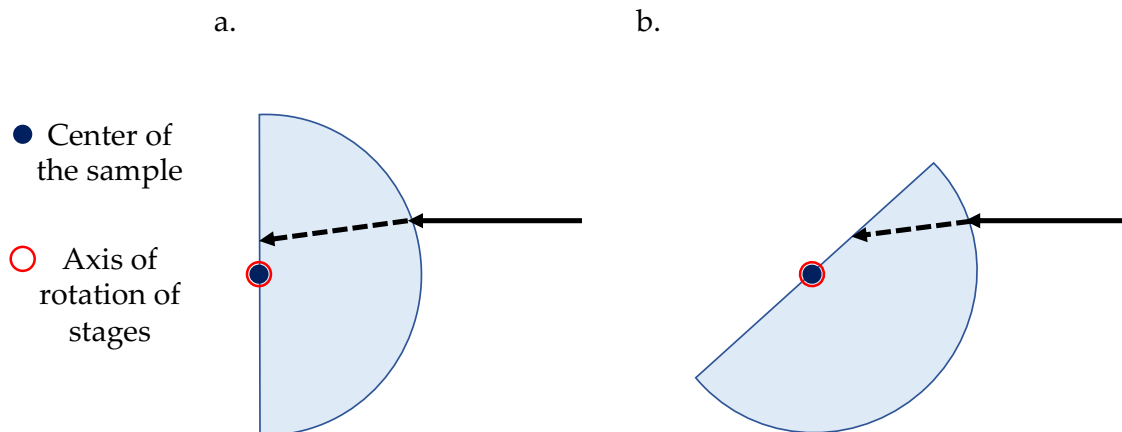


Figure 2.6. Off-axis laser misalignment example. a) When the BK7 glass is at 0° with respect to the incident beam, light hits the sample at normal incidence. b) When the semi-cylinder rotates, the incident light hits a different point of the surface.

In this geometry, the center of rotation of the sample corresponds to the axis of rotation of the stages (R1) and (R2), but the illuminating beam does not hit this spot. Consequently, the point where the beam is reflected moves as the rotation happens, affecting the reproducibility of the measurements and the alignment with the detector.

To avoid this issue, the first step in the alignment process is to check if the laser beam hits the sample in its center of rotation. This is done by rotating the sample until its flat surface is perpendicular to the incoming beam. Then, since the geometry of the holder does not allow for transmission measurements, the position of the sample stage is adjusted until the back reflected signal is superimposed to the incoming one ensuring the normal incidence. Another kind of misalignment can occur when the sample-holder (T2) is not correctly positioned. In this case, the center of rotation could be shifted with respect to the rotation axis of the system and moves during rotation, as shown in Figure 2.7.
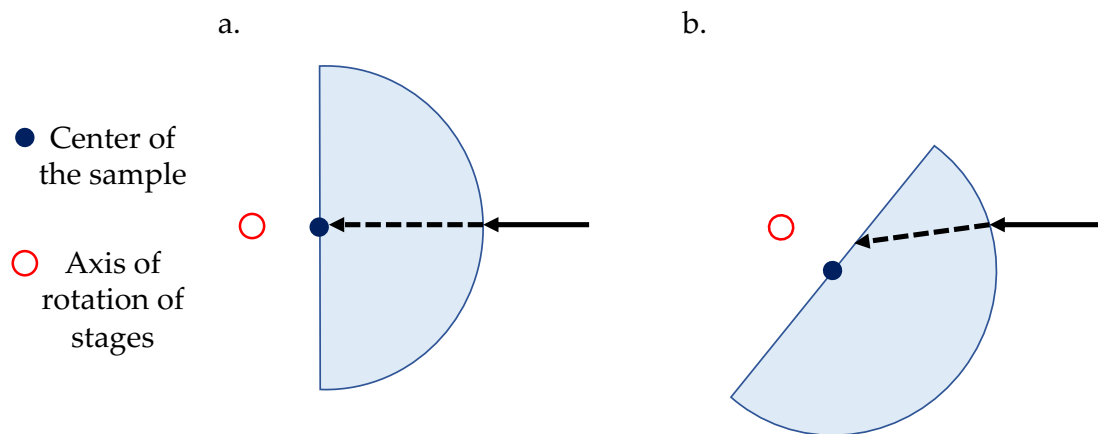


Figure 2.7. Off-axis sample misalignment example. a) When the BK7 glass is perpendicular to the incident laser beam, the light hits the axis of rotation of the stages without being deviated. b) When the sample rotates around its center, the light hits a different point of the semi-cylinder.

In this configuration, the center of rotation of the sample is misaligned with respect to the axis of rotation of stages (R1) and (R2). This issue does not allow one to illuminate the same sample position at different angles, affecting the quality of the measurement. This issue is taken under control by always checking that the angle at which the reflected beam exits from the sample corresponds to the angle at which the incoming light enters the prism. Since the holder does not ensure to always keep the same sample position in the mounting, every time the sample is removed and mounted those criticalities are checked. This is necessary also because samples under investigation have different dimensions, making the alignment control the first step before any acquisition. The intensity of the reflected beam is collected using a switchable gain silicon detector (model PDA36A-EC by Thorlabs). The angle of incidence of the light beam onto the 1DPC and the angular position of the collection arm are controlled using the rotational stages (R1) and (R2) in a θ-2θ configuration to measure the reflectivity scans. The control of the sample-detector rotation and the data acquisition of experimental points are regulated by a home developed LabView software. This experimental setup is used for the characterization of the photonic crystals in fluidic conditions, so a two-layer fluidic circuit is specifically designed in

collaboration with the CNR Institute for Photonics and Nanotechnologies of Milano (a representative picture of the system is reported in panel a of Figure 2.8).

a.                                      b.                                      c.
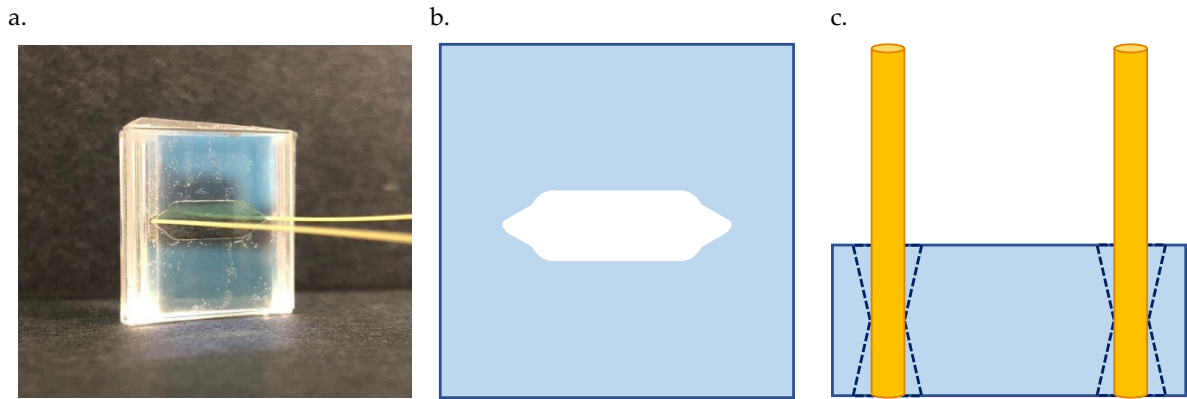


Figure 2.8. a) Picture of the assembled optofluidic chip. b) Sketch of the elongated geometry of the fluidic chamber. c) Sketch of the 3D clepsydra reservoirs for easy plug and unplug of fluidic tubes.

The intermediate layer of the fluidic system is a double-side polymeric tape (ARclad 8314-10, Adhesives Research, Inc., 193 μm thickness) with the fluidic chamber shaped in it using femtosecond laser (FemtoREGEN, High Q Laser GmbH, 1040 nm wavelength) micromachining.[69–71] Femtosecond laser microstructuring is a direct-write rapid prototyping technique, which shows great potential in lab-on-chip applications.[72] Ultrashort femtosecond laser pulses are delivered to the sample via nonlinear multiphoton absorption. The nonlinear interaction between ultrashort pulses and polymers allows for minimal thermal damage, enabling precisely ablated microchannels with minimal heat affected zones.[73,74] In particular, the output of the femtosecond laser passes through a power attenuator consisting of a half waveplate followed by a linear polarizer. A flipping mirror then allows the beam going through an optional second harmonic crystal for frequency doubling to achieve smaller spot size which leads to higher spatial resolution when working with fused silica.[75,76] The beam is then passed through beam shaping optics, which are typically used to correct for the asymmetric focal volume of the focused laser beam.[76] The profile of the chamber is ablated using the fundamental beam (100 kHz repetition rate) positioned on top of a computer-controlled transitional stage using a series of high-quality high-reflectance mirrors. The polymeric tape is placed on a horizontal plate fixed on translational stages and the laser beam approaches vertically from the top. The focusing lens (20× microscope objective, 0.35 numerical aperture, NA) is mounted onto an independent holder with micromanipulators for high precision displacement and tilt control. The final product is an elongated chamber (8 mm × 4 mm) with short inlet and outlet channels, as sketched in panel b of Figure 2.8. The top layer that closes the circuit is a fused silica coverslip (20 mm x 20 mm x 1 mm) with 3D clepsydra reservoirs, sketched in panel c of Figure 2.8, inscribed into it through femtosecond laser micromachining followed by chemical etching.[76] For the irradiation, the second harmonic of the same laser is used, at 1 MHz repetition rate focused by a 63× (0.75 NA)

microscope objective, a subsequent etching process in a 20% HF aqueous solution reveals the 3D reservoirs.

The clepsydra shape allows for an easy plug and unplug of inlet and outlet peek tubes (external diameter ≈ 360 μm) avoiding leakages during the filling process and the measurement. Layers are fabricated separately and then aligned and assembled to close the circuit before being mounted on the optical setup.

The described setup is also used for chirality investigation measurements by adding one optical element that allows one to have a chiral probe as shown in Figure 2.9.
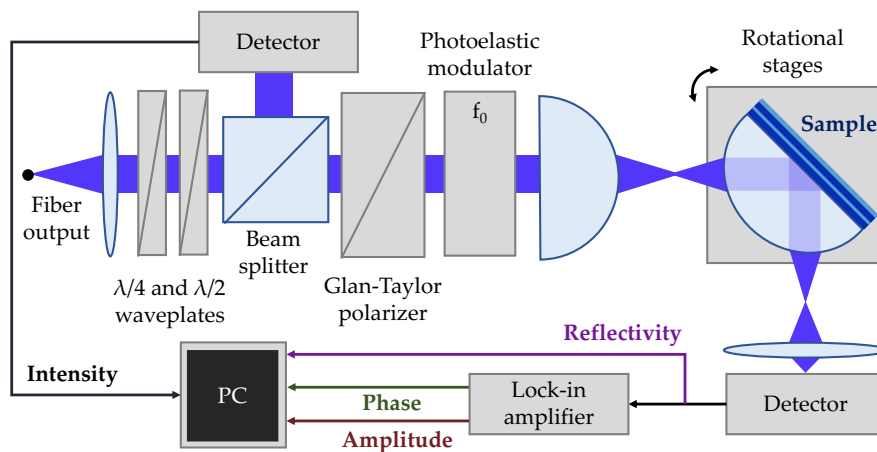


Figure 2.9. Experimental setup for circular dichroism measurements.

A photo elastic modulator (PEM) is therefore added after the Glan-Taylor polarizer. This element allows one to modulate at a fixed frequency of 50 kHz the polarization of the incoming light between right- and left-circular when the axis of the PEM makes an angle of 45° with the incident linear polarization. Since we have a modulated signal between opposite rotating circular polarization, we need to also add a lock-in amplifier to demodulate the detected response. Therefore, the collected total reflected intensity is sent directly to the PC for reflectivity signals but also demodulated to extrapolate its amplitude and phase components. For chiral measurements we have then three kinds of information: the reflectivity, that always acts as a check on the alignment and on the general quality of the investigation, the amplitude and the phase of the demodulated signal that, combined, will give the CD signal.

## 2.2. Polarization-resolved measurement setup

The second setup for the characterization of photonic crystals has been set at the Austrian Institute of Technology in Tulln. This system, schematically shown in Figure 2.10, is used for the acquisition of reflectivity maps as a function of the illumination wavelength and the angle of incidence inside the sample that will be shown in Chapter 3.
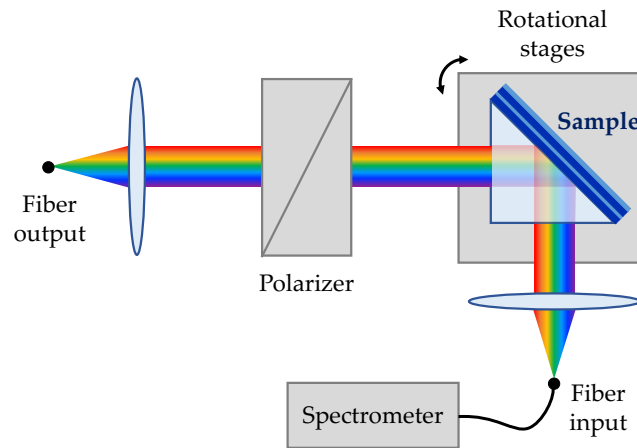
Figure 2.10. Scheme of the polychromatic illumination setup based at the Austrian Institute of Technology of Tulln.

The illumination source is an LED polychromatic light that allows one to investigate a spectral range between 430 nm and 600 nm. The output of the LED is coupled with a multimode optical fiber (core diameter: 50 μm, NA: 0.22) that brings the light to the optical path, where it is collimated with a lens. The beam then passes through a polarizer that allows to set the linear polarization of the light, switching between vertical (TE) and horizontal (TM) conditions. The incoming beam then reaches the sample, which is mounted on a LASF9 right-angle coupling prism and optically matched using immersion oil (refractive index n = 1.7). The illumination-collection geometry has a θ-2θ configuration, so both the sample arm and the detection arm are mounted on rotational stages controlled by a home-made LabView software. The intensity of the reflected beam is collected using a multimode fiber (core diameter: 200 μm) connected to a spectrometer (model FLMT06879 by Ocean Insight).

To exploit the mode superposition of photonic crystals we slightly modify the polychromatic illumination setup previously discussed to perform kinetic measurements collecting both TE and TM polarization simultaneously fixing the angle of illumination, as reported in Figure 2.11.
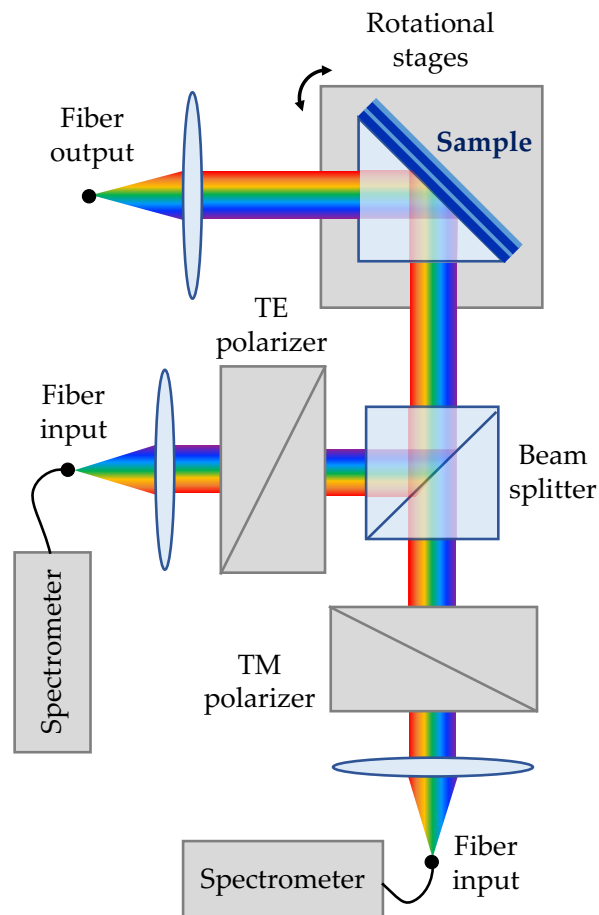
Figure 2.11. Scheme of the setup for polarization-resolved measurements.

The light beam is again a LED polychromatic source operating between 430 and 600 nm, but in this geometry the sample is directly illuminated with unpolarized light to excite both TE and TM modes. The angular position is fixed to investigate the spectral shift of the resonances. Since the two surface modes are spectrally superimposed, this configuration would work also with monochromatic illumination. In a general condition in fact the two modes have different excitation angles fixing the illumination wavelength, so the simultaneous investigation would not be possible. The selection of the observed polarization is performed after the sample, in the detection arm. A 50:50 beam splitter is used to divide the beam into two different parts, each one has its own polarizer that allows one to choose between TE and TM conditions. Then, the light from the polarization-selective branches is collected by 200 µm-core diameter multimode fibers that bring the signal to the respective spectrometer (model FLMT06879 by Ocean Insight). Finally, the spectrometer software extracts the spectral position of each resonance and plots it as a function of time. Polarization-resolved measurement performed with this setup are described in Chapter 4.

## 2.3.   Validation of the setup

A preliminary step in the employment of our setups is the validation part where we test our sensitivity in terms of angular and spectral variations. The first step is the acquisition of the reflectivity signal from a clean BK7 coverslip coupled with the substrate using the single-wavelength illumination setup. This allows us to check the overall quality of the alignment of the system and to evaluate the noise level affecting the measurements. One representative angular scan is shown in panel a of Figure 2.12.
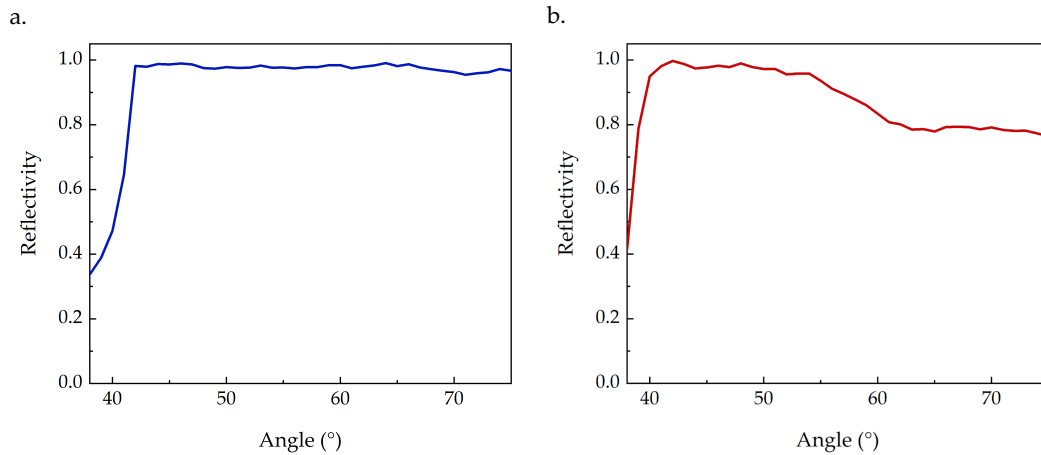


Figure 2.12. a) Reflectivity angular scan of a BK7 coverslip correctly aligned to the optical setup. b) Representative example of how the reflectivity signal is a fingerprint of the status of the alignment of the system. The curve does not show the flat behavior after the total internal reflection angle.

The illumination wavelength is set at 405 nm and the sample is kept in a dry environment. The curve shows a sharp onset of total internal reflection at the BK7-air critical angle, around 42° as expected, followed by a stable and flat behavior. When the sample is not properly aligned or cleaned, the total reflected signal presents some increasing or decreasing trend, specific footprint of something that needs to be checked, as representatively reported in panel b of Figure 2.12 when we intentionally misalign the sample. The total internal reflection signal is then used as a check point before running any experiment and the onset angle when the external medium is water acts also as a reference position when, during different measurements, samples are removed and mounted again, since it allows to compare their signals that can be slightly misaligned due to the unmounting/mounting process. The flat baseline in the total reflection regime, without any artifacts, also ensures that every feature appearing with 1DPCs or gold samples is coming from the mounted structures. The small intensity variations of the curve also confirm the optical stability and the low noise level of the setup. To certify the accuracy of the setup and validate the numerical analysis, we perform a standard refractometric characterization of one of the 1DPCs designed for CD measurements. We select the TE resonance and follow its angular position as a function of the variation of the refractive index of a glucose solution at 405 nm as reported in Fig 2.13.

a.

b.
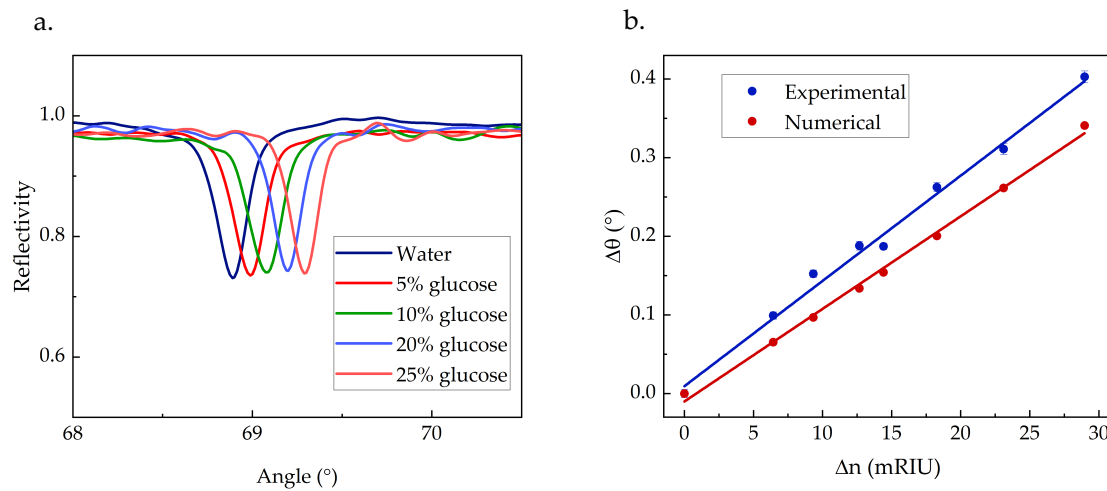
Figure 2.13. a) Angular scans belonging to different glucose concentrations. b) Plot of the variation of the angular position of the resonance as function of the refractive index of the solution. Experimental and numerical data points are shown together with their linear fit. Error bars when not visible are within the dimension of the data point.

The reference point is taken in water, then we let the refractive index change by increasing the concentration of glucose in the liquid at every step without removing the sample from the holder. We start with a concentration of 5% of glucose and reach a concentration of 25% that allows us to move from the water refractive index ($n_w = 1.33$ from refractiveindex.info) to a final refractive index of about 1.38 (refractive index of glucose are extracted using the Snell's law from the experimental position of the total internal reflection onset of each measurement). The position of the resonant dip with respect to the reference position is then plotted as a function of the variation of the refractive index in refractive index units (RIU). The experimental behavior nicely reproduces the numerical one, with a TE angular sensitivity of 13.4 °/RIU in very good accordance with numerical predictions of about 11.8°/RIU. A similar validation is performed to assess the accuracy of the polychromatic illumination setup. We focus on the TE resonance, as previously done for the glucose validation, and analyze the mode shift as a function of the variation of the refractive index of a sucrose solution flowed on top of the sample. Reflectivity maps are collected starting with water, then using sucrose solutions with concentrations around 4% and 8%, whose refractive indexes are tabulated in laboratory manuals. From the reflection maps, the angular signal at a fixed wavelength $\lambda = 430$ nm is isolated. From this curve, the position of the minimum of the resonance is extracted and plotted as a function of the variation of the refractive index, as shown in Figure 2.14.
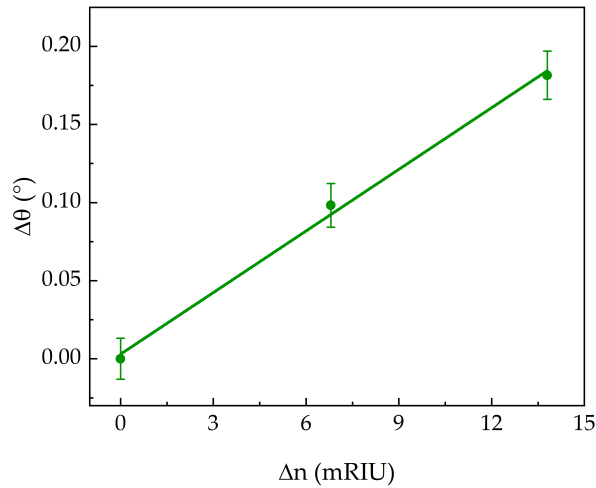
Figure 2.14. Sensitivity calculated by extrapolating the signal at fixed wavelength λ = 430 nm from reflectivity maps when sucrose solutions with concentrations 4% and 8% are brought in contact with the surface of the crystal.

The linear fit of the points gives an angular sensitivity of about 13.1 °/RIU, in accordance with the previous characterization, ensuring the compatibility between results coming from different setups. The same validation with sucrose solutions is performed with the kinetic signal acquisition to estimate the spectral sensitivity of the same sample. The validation is performed with of the polarization-sensitive setup, so fixing the angle of illumination, and focusing again on the TE mode using different concentrations of sucrose solutions as done before. A typical output signal is reported in panel a of Figure 2.15.
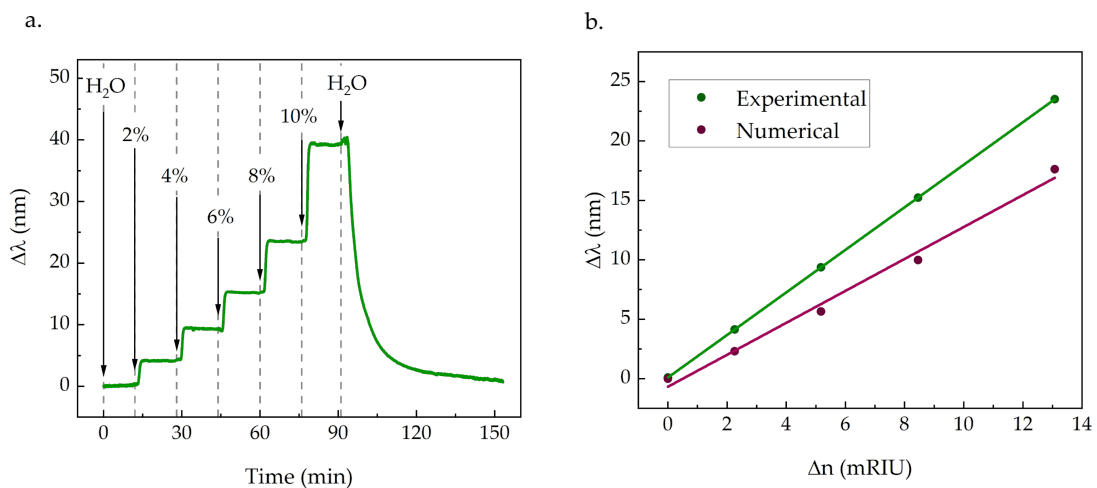


Figure 2.15. a) Time evolution of the spectral position of the TE resonance, plotted in Δλ, as function of the concentration of the sucrose solution that is in contact with the surface of the crystal. b) Experimental and numerical sensitivities of the analyzed sample. Experimental dots are extrapolated from the kinetic curve and error bars are within the dimension of the points.

The step-like curve is obtained bringing sucrose solutions in contact with the surface of the photonic crystal. The signal is obtained fixing the angle of investigation and

following the spectral shift of the TE mode dip, extrapolated through peak function fitting by the software in use, and plotting it as a function of time. Each step corresponds to a bulk refractive index variation due to the different sucrose concentration of the solution. The first and the last liquid that is in contact with the photonic crystal surface is water: at the beginning we start with water since it represents the reference solution for the crystal characterization while it is also flowed at the end to check if the position of the mode goes back to the original one, confirming the good quality of the measurement and that nothing is bounded to the surface during the measurement. From the kinetic curve it is possible to extrapolate the spectral shift of the mode and plot it as function of the refractive index variation, as shown in panel b of Figure 2.15. Each point represents the average shift due to the change of the solution on the surface of the crystal, with error bars that are within the dimension of the point. A linear fit is used to evaluate the experimental sensitivity of the sample, with an estimation of $S_{exp} \cong 1790$ nm/RIU. The sensor, that is not specifically designed to be an optimized refractometric platform, has however a very good sensitivity, with performance that is only slightly below plasmonic sensors.[61,77] The calibration is finally repeated numerically, with simulated points reported in panel b of Figure 2.15. The sensitivity is calculated with the linear fit of the resulting points and has a value $S_{num} = 1344$ nm/RIU, that is slightly below the experimental result but still compatible to it.

# 3 Chapter three: Experimental characterization of the 1DPC

In this chapter, the fabrication of 1DPCs is described, together with the optical characterization of the platforms. The growth was performed by Dr. J. Gil-Rostra and Dr. F. Yubero at the Instituto de Ciencia de Materiales de Sevilla, CSIC-Universidad de Sevilla. Microfluidics was then applied thanks to a collaboration with Dr. R. Martínez Vázquez and Dr. R. Osellame at the Institute for Photonics and Nanotechnologies of the CNR in Milano and with Prof. G. Simone from the Nortwestern Polytechnical University in Xi'an Shaanxi, People's Republic of China. We also acknowledge the collaboration with Dr. G. Pellegrini at the University of Pavia in the design and theoretical analysis of the multilayers. Different designs are investigated through the acquisition of reflectivity maps and angular scans at fixed wavelength in aqueous-based environment. Experimental results are compared with simulations. Preliminary CD measurements are finally shown.

## 3.1. Fabrication

The one-dimensional platform described in Ref. 53 and in Chapter 2 has been fabricated thanks to the collaboration with the Instituto de Ciencia de Materiales de Sevilla. A well-established process is employed: reactive magnetron sputtering.[78] In general, sputtering is defined as the procedure where atoms or clusters are ejected from a solid surface, called target, because of a bombardment of high energy particles. Materials are ejected from the target in a usable quantity which can directly coat a substrate. To obtain sputtering as a useful coating process several criteria must be satisfied.[79] First, ions of sufficient energy must be created and directed towards the surface of the target to eject atoms from the material. Then, emitted atoms must be able to move freely towards the object to be coated with little impedance to their movement. Sputtering is indeed a vacuum process: low pressures are required to maintain high ion energies and to prevent too many atom-gas collisions after ejection from the target. This requirement to work at low pressures is in contrast with the process of producing bombarding ions for the target, called plasma generation. One solution is to use a magnetic source that produces a specially shaped magnetic field steered to a diode sputtering target. The cathode surface is immersed in a magnetic field such that electrons are localized in a region close to the cathode where electron traps are created

so that drift currents close on themselves. In this way the probability of ionizing collision with a gas atom is increased and therefore also the ionization efficiency increases. This brings to a growth of the ion current density on the target which is proportional to the erosion rate of the target itself. In the simplest of applications, the magnetron is used to deposit metallic materials by DC sputtering. The DC magnetron is the cheapest magnetron processes because DC power supplies are simpler to manufacture than RF. In this operating mode the target is directly conducting electricity. DC magnetron therefore will not work with insulating targets because no sizeable current can flow through it. One expensive solution could be to use an alternating current at high frequency, called RF sputtering. On the other hand, most of the materials which can be sputtered by RF from compound targets can also be sputtered by DC magnetron sputtering but in a reactive gas atmosphere. This method, called reactive magnetron sputtering, allows for high deposition rates and on an industry scale.[80–83] During the process, argon gas is introduced as the carrier gas together with a small quantity of a second reactive gas into the chamber. The gas may be any gas that will react with the target atoms to form the desired compound.[83] Nitrogen and oxygen are common choices. In our case the process gas consisted of a mixture of Ar (40 sccm) and $O_2$ (4 sccm) at a pressure of $5.0 \cdot 10^{-3}$ mbar. Tantalum and silicon targets (75 mm diameter) are used with a source operated with a pulsed DC power supply (AE Pinnacle Plus, frequency 120 KHz, reverse time 2.5 μs). The desired compounds are formed both at the magnetron surface and at the substrate, depending on power and surface reactivity. By controlling the reactive gas flow rate, it is possible to control the stoichiometry of the growing film.[83] In our case, the multilayers were prepared at 150 °C and the magnetron target-substrate distance was approximately 10 cm. The sample holder was continuously rotated during the deposition process to achieve a homogeneous thickness distribution within the surface area of the platform. The base pressure of the deposition apparatus was $5.0 \cdot 10^{-8}$ mbar. Panel a of Figure 3.1 shows the SEM cross section image of one of the truncated 1DPCs manufactured on a polished silicon wafer.

a.



b.

| 165.3 nm | $n_L$ |
|---|---|
| 8.2 nm | $n_H$ |
| 56.6 nm | $n_L$ |
| 76 nm | $n_H$ |
| 244.6 nm | $n_L$ |
| 76 nm | $n_H$ |
| 244.6 nm | $n_L$ |
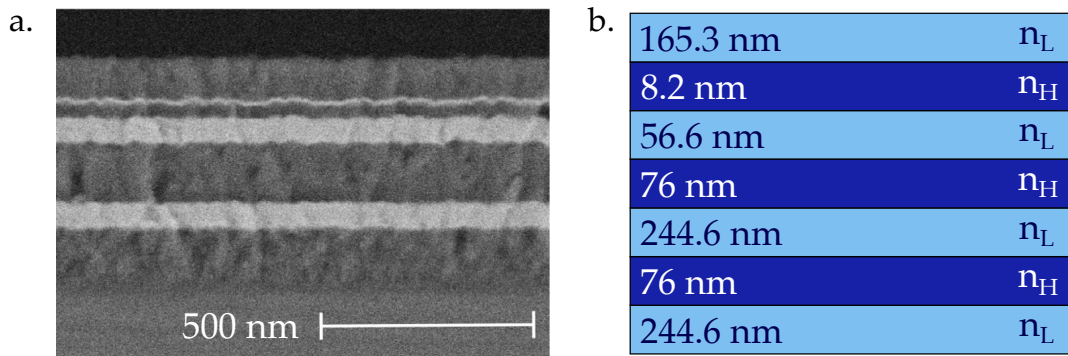
Figure 3.1. a) SEM image of one of the fabricated samples. b) Thicknesses of the fabricated multilayer adjusted after fitting of the experimental results.

The image shows compact deposited material and sharp interfaces between adjacent layers. Brightness contrast between layers is due to the different atomic weights of the $Ta_2O_5$ and $SiO_2$ layers. The calibration of the growth parameters was performed with a trial-and-error procedure against the simulated normal-incidence reflectance spectra of the nominal design, while controlling the deposited thickness with a quartz microbalance. A few bunches of samples are fabricated also slightly deviating from the nominal design to study how thickness variations affect the dispersion relations of surface modes. We end with a set of samples with the nominal thickness, a series where thicknesses of layers are incremented by 10% and some sets with decreased thicknesses. All the produced samples that we have experimentally characterized are reported in Table 3.1 together with their label. In this and the next Chapters, results from highlighted samples are presented.

| Label | Design | BK7 substrate | Samples |
|---|---|---|---|
| #DM1 | Nominal + 10% | Coverslips (x3) | **#DM1.1;** #DM1.2; **#DM1.3** |
| #DM2 | Nominal – 10% | Coverslips (x4) | #DM2.1; #DM2.2; #DM2.3; **#DM2.4** |
| #DM4 | Nominal – 10% | Coverslips (x4) | #DM4.1; #DM4.2; #DM4.3; #DM4.4 |
| #DM5 | Nominal – 10% | Semicylinder | #DM5.1; #DM5.2 |
| #DM6 | Nominal [53] | Coverslips (x4) | #DM6.1; #DM6.2; **#DM6.3;** DM6.4 |
| #DM7 | Nominal | Semicylinder | **#DM7.1;** #DM7.2 |
| #DM8 | Nominal – 20% | Coverslips (x3) | **#DM8.1; #DM8.2; #DM8.3** |
| #DM9 | Nominal – 20% | Semicylinder | #DM9.1; #DM9.2 |

Table 3.1. List of the available and characterized samples. Highlighted labels correspond to samples whose characterization is shown in this thesis.

After the characterization phase we adjust the simulation parameters to fit the experimental results that will be discussed in this Chapter. To reproduce the experimental spectra, we use a genetic optimization method. This kind of optimization imitates natural selection. It starts with a random population of candidate solutions and then picks the best ones, based on their fitness, to serve as the parents of the following generation. The procedure is usually continued until the fitness function converges to the specific target or for a predetermined number of generations. We specifically apply the differential evolution algorithm to minimize the least square difference between the numerical and experimental reflectance spectra. A typical fitting technique generates a population of about 4 times the number of layers for 200 generations. This brings to a variation of less than 15% compared with the thicknesses of the nominal optimized crystal presented in Chapter 2, so new thicknesses are reported in panel b of Figure 3.1.

## 3.2.  Demonstration of mode superposition

The peculiarity of the 1DPC proposed in Ref. 53 is the possible manipulation of the dispersion relations of the surface modes to make them overlapped over a broadband spectral range so the demonstration of such overlap is a key step for the research described in this thesis. In Figure 3.2 the simulated band structures for the TE (panel a) and TM (panel b) surface modes are reported, together with the dispersion relations, obtained with the fitted design of the sample, which act as a starting point for our investigation.
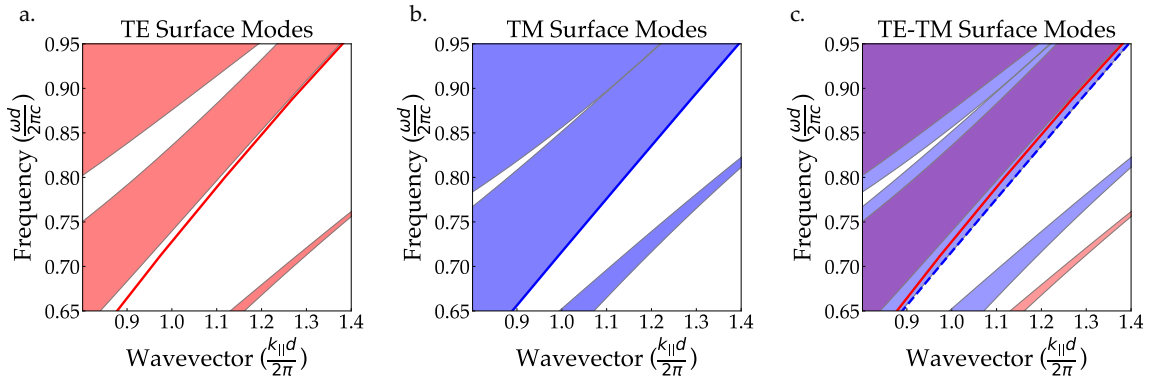


Figure 3.2. Band structures with respective dispersion relation of the surface mode. a) TE surface mode. b) TM surface mode. c) Graphically superimposed band structures of TE and TM modes to demonstrate the parallelism of the dispersion relations.

Photonic bands are represented as shadowed regions, while the TE and TM dispersion relations of the BSWs are indicated as solid lines. They are calculated with the supercell methods using the inverse master equation eigenproblem considering material thicknesses obtained fitting the experimental results that will be shown in this Chapter. The TE mode runs mainly far from the edge of the band gap, while the TM is localized

at the very edge, so additional radiative losses are expected, meaning larger spectral width of the mode. In panel c the TE and TM band structure are graphically superimposed, so the parallelism and partial overlap of dispersion lines are visible in contrast with the perfect superposition shown in Chapter 2 for the optimized crystal. There is a small misalignment between them over the considered energy range that will be then confirmed experimentally but this does not affect much the optical performance of the sample, that keeps an optical chirality enhancement of a factor 50, as shown in Figure 3.3, to be compared with an enhancement of about 70 for the nominal optimized structure discussed in Figure 1.14.
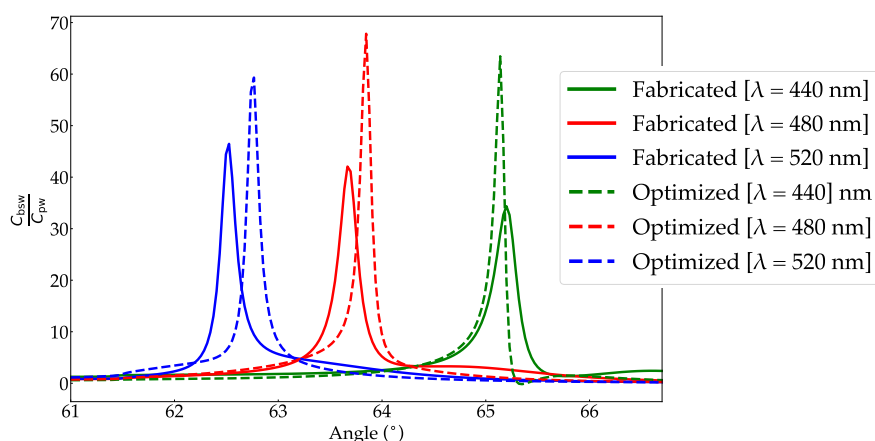


Figure 3.3. Comparison between the simulated optical chirality enhancement of the optimized design and the fabricated one.

Considering 3 different wavelengths, it is possible to observe an enhancement that is slightly lower than the optimized design but still sets to between one and two orders of magnitude, a good starting point for chiral molecule investigation. To validate the platform, reflectivity maps are collected as a function of the wavelength of illumination and the angle of incidence inside the BK7 substrate with respect to the surface normal. The experimental results are shown in Figure 3.4 for both TE (panel a) and TM (panel b) illumination conditions when the external medium is water.
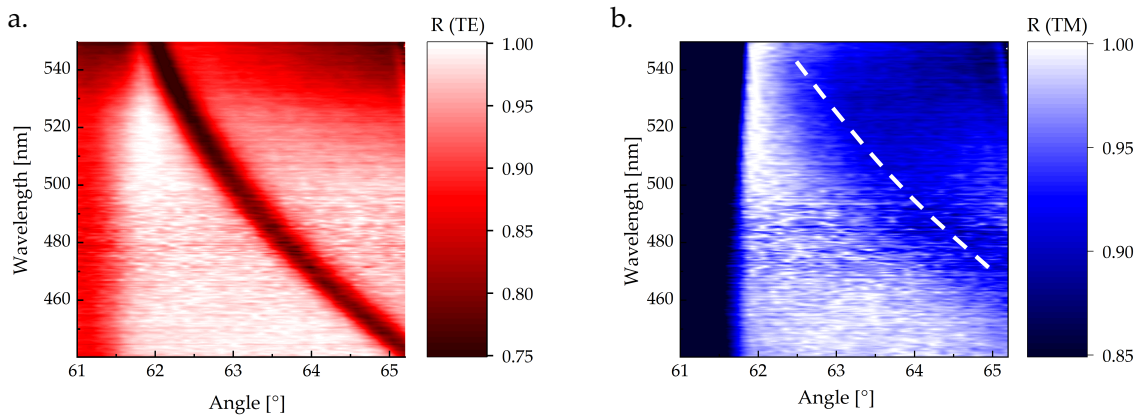
Figure 3.4. Experimental reflectivity maps. a) TE surface mode. b) TM surface mode as a function of the illumination wavelength and of the angle of incidence on the sample.

The surface mode appears as a dip in the reflection spectrum and that is clear looking at the TE map, where the mode dispersion is strongly visible and sets with an intensity decrease of about 30%. The TM mode, instead, appears only as a halo in the dispersion map, compatibly with the position of the mode at the edge of the band gap. Comparing the experimental behavior with simulations, shown in Figure 3.5, it is possible to recognize the weakness of the TM mode with respect to the TE one.
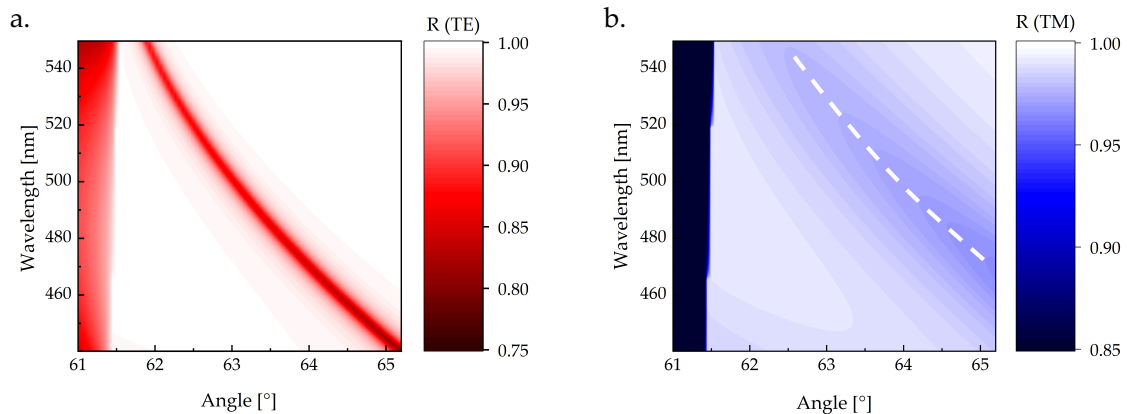


Figure 3.5. Numerical reflectivity maps. a) TE surface mode. b) TM surface mode as function of the wavelength illumination and of the angle of incidence on the sample.

Indeed, one can recognize a common behavior between the modes that upon increasing the wavelength, the excitation angle decreases moving towards the total internal reflection onset, as expected. For a better visualization of modes' overlap it is worth looking at angular reflectivity signals at fixed wavelength. In Figure 3.6 experimental angular scans are reported compared with the respective simulated curves.
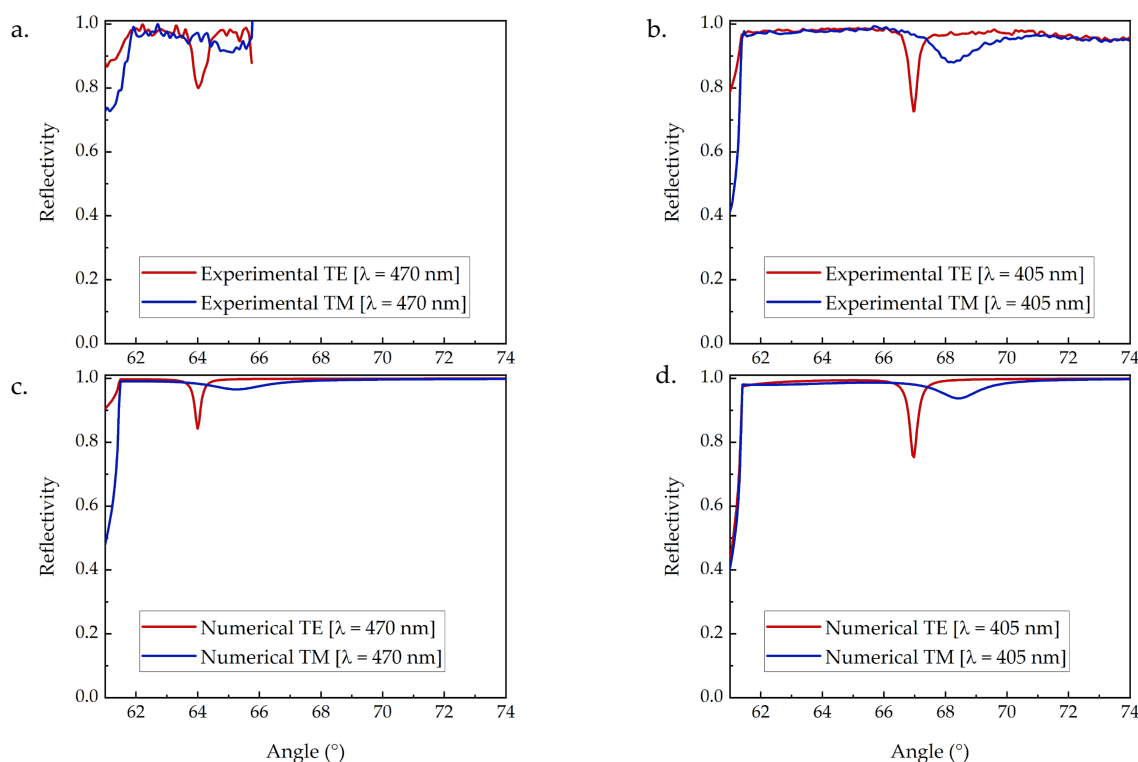
Figure 3.6. Comparison between experimental and numerical TE and TM surface modes at fixed wavelength. a) Experimental curve at 470 nm. b) Experimental curve at 405 nm. c) Numerical curve at 470 nm. d) Numerical curve at 405 nm.

In panel a, a cut at 470 nm wavelength of the reflectivity maps of both surface modes is shown, while in panel b the measurements with the laser diode at 405 nm are reported. The TE mode appears narrower and sharper with respect to the TM one, which is broad, weak but still recognizable. It is now clear that the overlap between the modes is not perfect, as predicted with the band structures, but it is also confirmed that the two dispersion relations run parallel over the spectral range of interest. Indeed, the relative position of the modes is conserved upon changing the wavelength. In panels c and d simulated curves at 470 nm and 405 nm are reported. The accordance between experimental data and numerical results is excellent both in terms of intensity of the modes and angular position, pointing out that the new fitting can give an accurate description of the behavior of the sample. The partial overlap of the modes, which still gives a good optical chirality enhancement around a factor of 50, see Figure 3.3, tells that there is still room for improvement but represents a good starting point for polarization-resolved spectroscopies. These results represent the first successful experimental demonstration in the literature of degenerate TE and TM BSWs over a broad spectral range.[53]

Since many samples are available with slightly different designs, we characterize with reflectivity maps also other samples, here we report other two results. The first one, shown in the left panels of Figure 3.7, has layers with thicknesses decreased of about

10% with respect to the reference one, while the second depicted sample, in panel b and d of Figure 3.7, has layers that are slightly thicker.
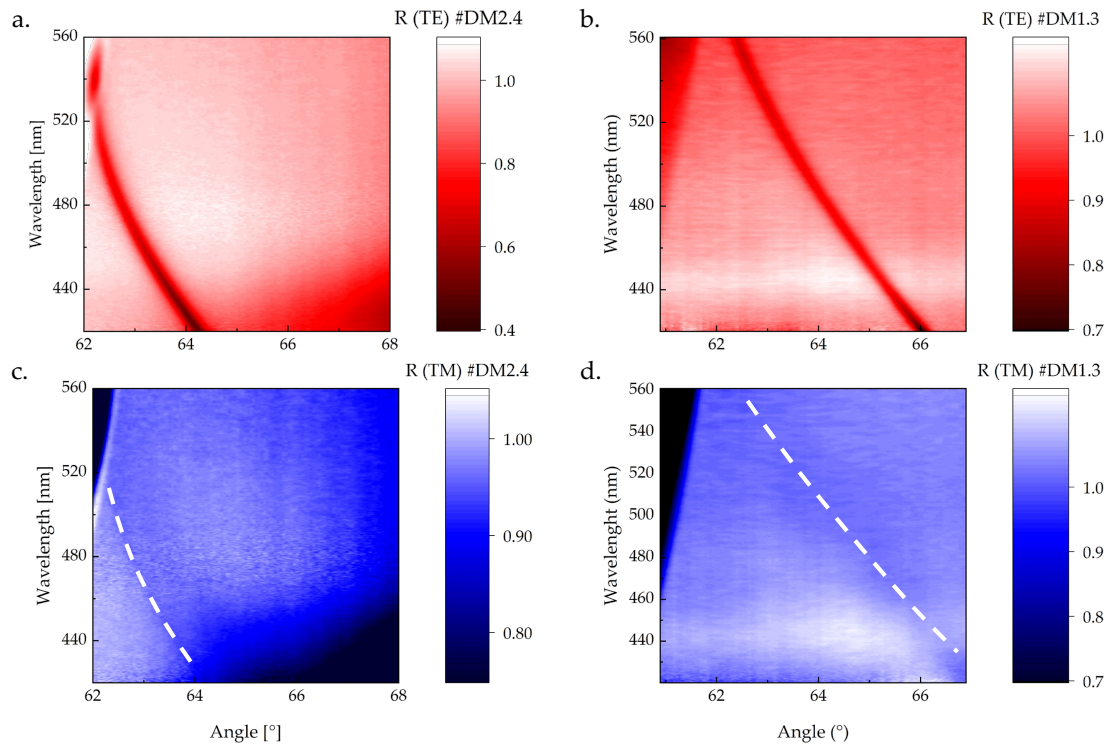


Figure 3.7. Experimental reflectivity maps of two different samples. a) TE reflectivity map of sample #DM2.4. b) TE reflectivity map of sample #DM1.3. c) TM reflectivity map of sample #DM2.4. d) TM reflectivity map of sample #DM1.3.

As for the previous sample, we can notice the strong TE mode that is recognizable and whose behavior is easily distinguishable from the background while the TM mode is always weak and becomes visible only looking at fixed wavelength angular plots. Examples of section lines from the dispersion maps of Figure 3.7 are shown below in Figure 3.8.
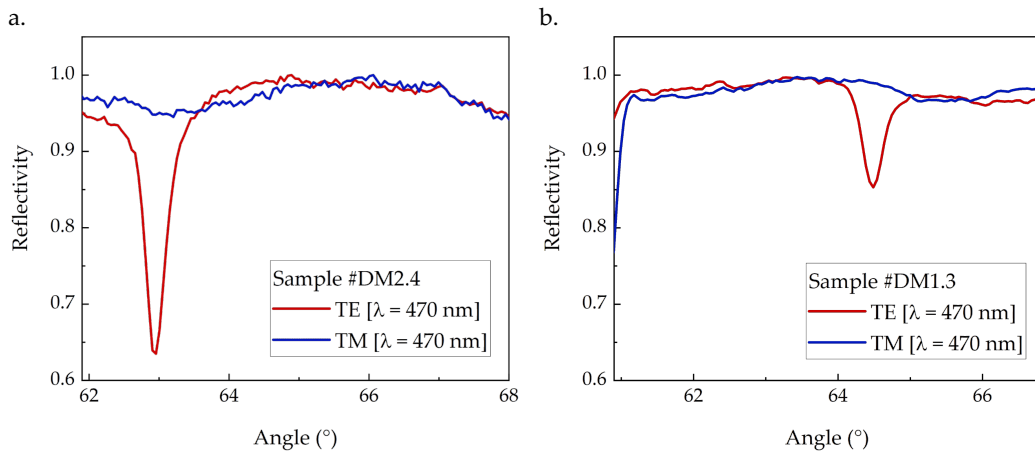
Figure 3.8. Experimental TE and TM curves extrapolated from the reflectivity map fixing the wavelength λ = 470 nm for a) sample #DM2.4 and b) sample #DM1.3.

These spectra confirm the behavior described before, with the TE mode positioned at the edge of the TM one. This kind of comparison suggests another analysis of samples as a function of the slight variation of thicknesses of the layers. It can be noticed in fact that, even if the relative position between the modes is conserved, the excitation angle of both TE and TM changes as we change the investigated design, with also a variation of the intensity of the modes. This is clear from angular scans of three different samples shown in Figure 3.9.
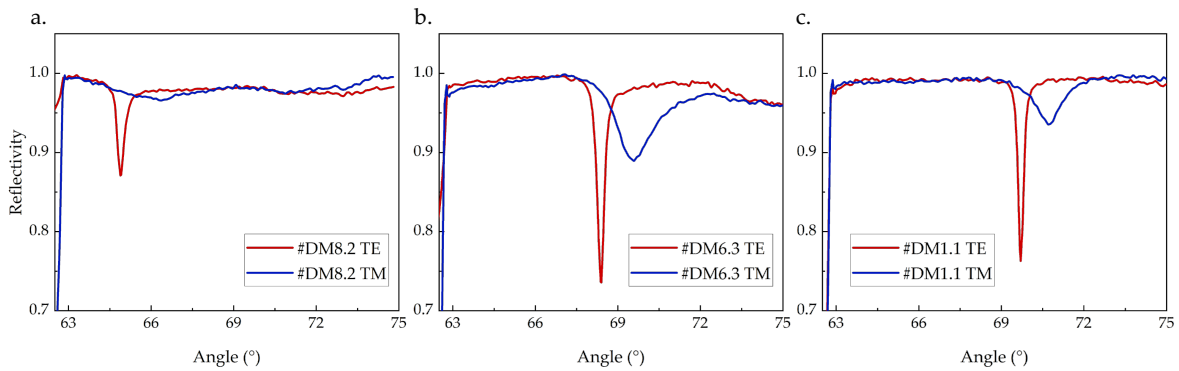


Figure 3.9. Experimental angular scans of both polarized modes at 405 nm of samples with different designs. a) Sample #DM8.2. b) Sample #DM6.3. c) Sample #DM1.1.

The central panel contains the angular scan of the reference sample,[53] on its left a sample with thinner layers and on its right a sample with thicker layers all at a wavelength of 405 nm. It can be noticed how, with a variation of about ± 20%, the overlap relation of the modes is the same but the excitation angle shifts towards smaller angles if we reduce the thicknesses and in the opposite direction if thicknesses are increased. This means that the scalability of the layer thickness is solid and so each of our investigated samples has the potentiality to work for chiral investigations. Another aspect that we have investigated is the reproducibility within a particular set of samples. During the fabrication phase, bunches of four samples are deposited

simultaneously so, in principle, have the same nominal thicknesses of the layers. It is then interesting to check optically the design of each sample of the set. We focus on samples labelled #DM8, whose design shows thinner layers with respect to the one described in Ref. 53. We investigate those three samples, fabricated at the same time, and check if the position of the excitation angle of surface mode is the same and compare the intensity of modes. Panels with the comparison between #DM8 samples are reported in Figure 3.10.
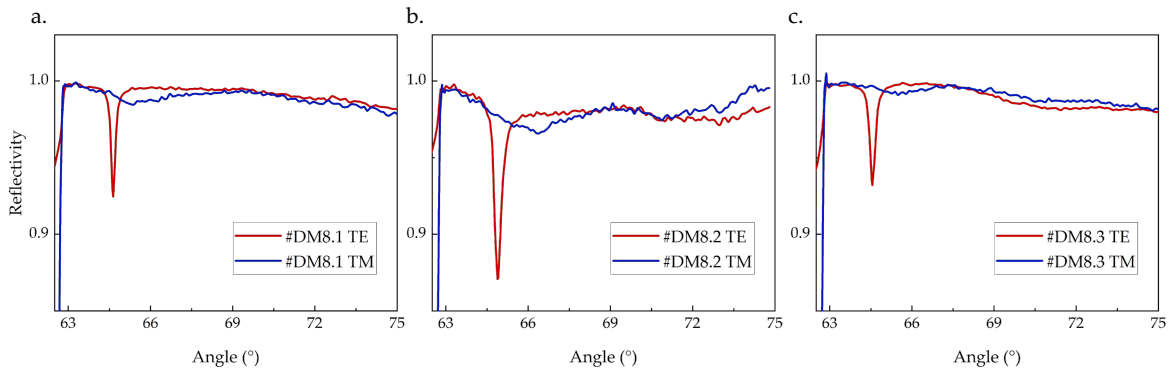


Figure 3.10. Angular scans of both polarized modes at 405 nm of samples with the same nominal design that are fabricated simultaneously. a) Sample #DM8.1. b) Sample #DM8.2. c) Sample #DM8.3.

Angular scans are taken at 405 nm wavelength in an aqueous environment. The general behavior belonging to this kind of photonic crystals is again reported: the TE mode is narrower and sharper with respect to the TM one even if those sample present, in general, weaker modes with respect to other samples shown before. However, it is possible to recognize both polarizations of the surface waves and compare them along different samples with the same design. All panels show TE modes that are excited at an angle around 65°, while the TM mode stays at slightly larger angles.

Once investigated the different possible designs of the crystal and confirmed that all could be valid for chiral investigation, we move to the study of the best geometry for the samples. The choice is between 1DPCs fabricated on BK7 glass coverslips (2 x 2 cm$^2$, to be matched with a coupling prism) or directly on BK7 semicylindrical substrates so that we avoid the coupling oil between the sample and the substrate. First, we check if one geometry is preferred in terms of optical signal. In Figure 3.11 a comparison between surface modes of a 1DPC grown on the coverslip and the respective fabricated on the semicylinder is shown.
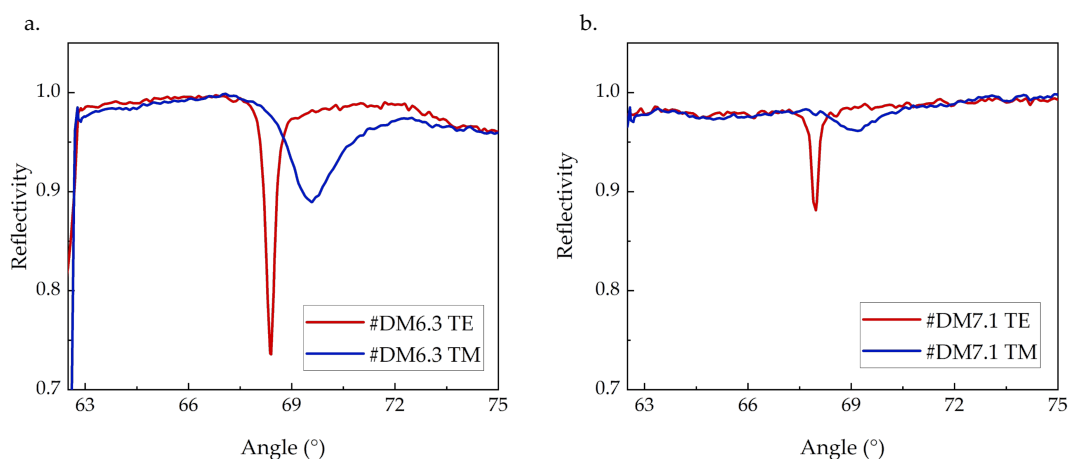
Figure 3.11. a) Experimental reflectivity angular scans of TE and TM modes of sample #DM6.3 grown on a BK7 coverslip. B) Experimental reflectivity angular scans of TE and TM modes of sample #DM7.1 grown on a BK7 semicylindrical substrate.

The #DM6.3 sample under investigation is the one proposed in Ref. 53 and the #DM7.1 is the same design fabricated directly on the semicylinder. The benchmark of the modes is clearly visible both for the coverslip and semicylindrical geometry, even if this last one has weaker modes. The excitation angle is the same, proving a good reproducibility of thicknesses during sample preparation, and the relative overlap between the two modes is conserved. This makes both samples good candidates for chiral molecules investigation, with the choice of the preferred geometry only due to setup issues. It is true in fact that with a semicylindrical substrate a coupling with immersion oil is not needed, avoiding issues due to leakages or air bubbles in the liquid with consequent artifacts in the signal, but this geometry makes the assembly of the fluidic part very challenging. Moreover, a squared coverslip is much more versatile from the application point of view, with the possibility to couple it to different systems, as we did with the samples employed between the Italian setup and the one based in Austria.

## 3.3. Preliminary chiral measurements

Once concluded the characterization phase, fundamental in the understanding how the fabrication influences the final design of the sample with the consequential slight variation of the position of the modes, we move to preliminary measurements using custom chiral molecules. We use the enantiomerically pure molecule o-MR-PEA (o-methyl red conjugates with chiral 1-pheniyl-ethykamine), whose structure is shown in Figure 3.12, synthetized at the Department of Chemistry, Materials and Chemical Engineering of Politecnico di Milano following the procedure described in the work of H. Yamamoto et al.[84]

a.

b.
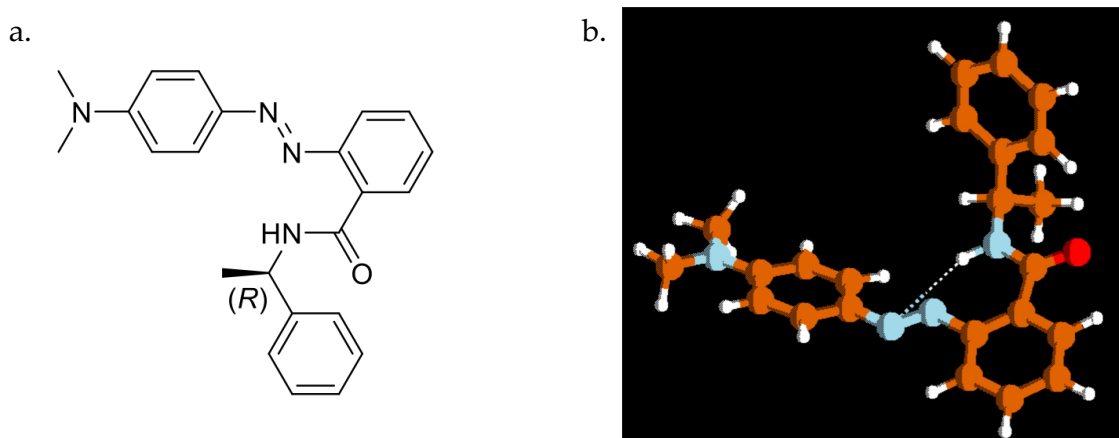


Figure 3.12. a) 2D representation of the o-MR-(R)-PEA molecule. b) 3D representation of the molecule.

This molecule is specifically selected to absorb in the blue region, the working range of our 1DPC, and requires very active solvents, not being soluble in water. The first investigated solutions used chloroform as solvent and were characterized in cuvette with a commercial spectrophotometer. In Figure 3.13 we show the molar extinction coefficient spectrum extrapolated from the absorption spectrum of a quartz cuvette filled with a 200 µM solution of the (R) enantiomer.
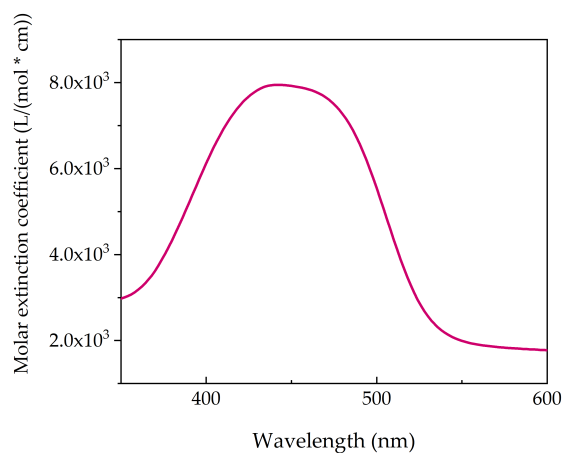


Figure 3.13. Molar extinction coefficient spectrum extrapolated from the absorption spectrum of a 200 µM solution of the (R) enantiomer.

The extinction coefficient peak is broad and centered in the spectral region of interest, between 400 and 500 nm. Due to the chemically active solvent, standard materials for fluidic chambers, like PDMS and the polymeric double-tape in use for aqueous characterization, could not be employed. So, less chemically active solvents were considered. We ended up with 3 choices: acetonitrile ($CH_3CN$), ethylene glycol ($OHCH_2OH$) and nitromethane ($CH_3NO_2$). These solvents are then characterized at the spectrophotometer to check their absorption in the spectral region of investigation, results are shown in Figure 3.14.
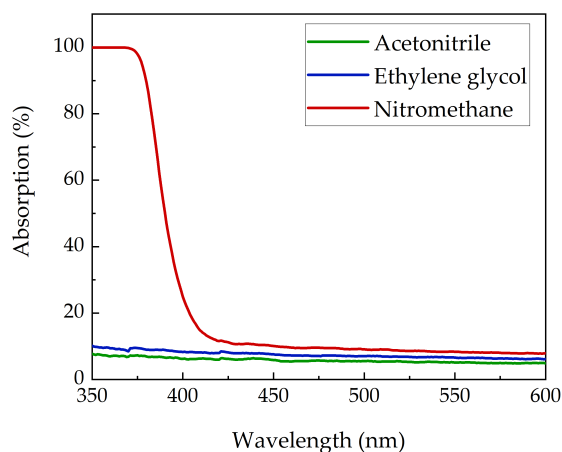
Figure 3.14. Absorption spectrum of the three investigated solvents: a) acetonitrile, b) ethylene glycol and c) nitromethane.

Nitromethane has a strong absorption at short wavelengths, so it is not compatible with our system and purpose. Ethylene glycol and acetonitrile have instead a very flat response without introducing significant absorption, being both good candidates for our molecules. The high viscosity of ethylene glycol then, represents a possible issue in the fluidic process, so we decide to choose acetonitrile as solvent. In principle, the double-sided polymeric tape used for fluidic chamber is compatible with the solvent and this was confirmed with an overnight test with the chamber filled with acetonitrile. Then we move to a dynamic test, and we notice that the solvent interacts with the edges of the chamber, detaching some tape residuals and obstructing the connections. Moreover, the damage of the main chamber translated into leakages and into the detaching of the tape from the crystal after some measurement time. Two microscope images of the chamber after this test are shown in Figure 3.15.
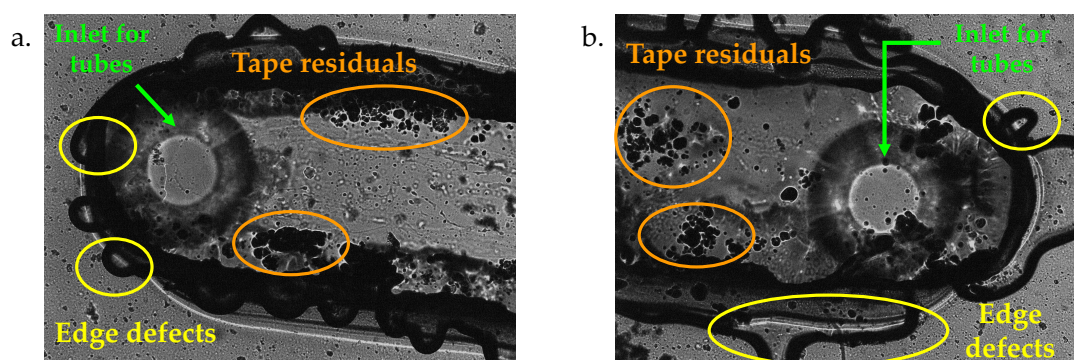


Figure 3.15. Microscope image of the polymeric tape after dynamic resistance test. Highlighted in yellow edge defects caused by leakages of the solvent. Highlighted in orange residuals of the polymeric tape inside the fluidic chamber. In green are indicated inlet/outlet holes for fluidic tubes.

Points highlighted in yellow are the modified edges of the chamber after the interaction with the solvent and they are visible also by eyes as red-colored boundaries that then could provide leakage channels for the solvent. In orange polymeric tape

residuals inside the fluidic chamber are instead indicated. We have therefore to move to another material that is not affected by the presence and by the flux of acetonitrile. The solution is the employment of the SU-8 photoresist, a well-established material for fluidic systems.[85–87] The chip, realized again in collaboration with the Institute of Photonics and Nanotechnology of the CNR in Milano, consists of three parts: the photonic crystal, the SU-8 layer and the top layer containing the reservoirs. The protocol to fabricate and assemble the platform starts with the production of the top fused silica glass that contains two clepsydra reservoirs separated center to center by 14 mm. The shape of the holes ensures an easy plug and unplug of input and output tubes whose internal diameter is 500 μm while the external one is slightly below 800 μm. This part is fabricated using femtosecond laser micromachining, as previously discussed in Chapter 2. Once the top layer is manufactured, it is wet etched with HF 20% in an ultrasonic bath at 35 °C for 1 hour. After that, the top layer is placed in a chromic bath for 12 hours to remove any possible organic residue. The following fabrication steps of the chamber are shown in Figure 3. 16.
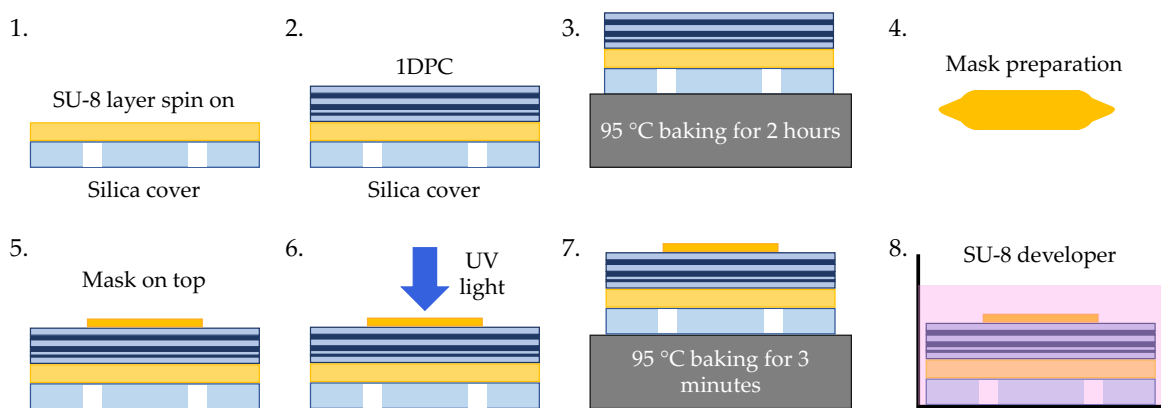


Figure 3.16. Schematic representation of steps for the fabrication of the optofluidic system made by SU-8 photoresist.

The surface of both the photonic crystal and the top layer that will be in contact with the resin are treated with plasma cleaning (in an oxygen atmosphere). This activates the surfaces and makes them more receptive to the resin. Then, SU-8 is deposited to cover the top layer, and it is spun up to a maximum of 2000 rpm with a spin coater, thus obtaining a quasi-uniform layer with a thickness of around 100 μm. The photonic crystal is placed on top and a soft baking at 95 °C is done for 2 hours. Afterwards, the region of the SU-8 layer that will not be the microfluidic chamber has to be polymerized with UV light. For this, the mask with the chamber geometry (with a fused silica plate with a thickness of 2 mm) is fabricated with femtosecond laser micromachining and coated with an 80 nm gold layer. Placing the mask in the correct area of the top layer, the chip is polymerized with UV light for 1 minute. A post exposure baking at 95 °C is then done for 3 minutes. Finally, the uncured resin is removed from the chip through the reservoirs using SU8 developer for 12 hours. A picture of the fluidic chip is reported in Figure 3.17.
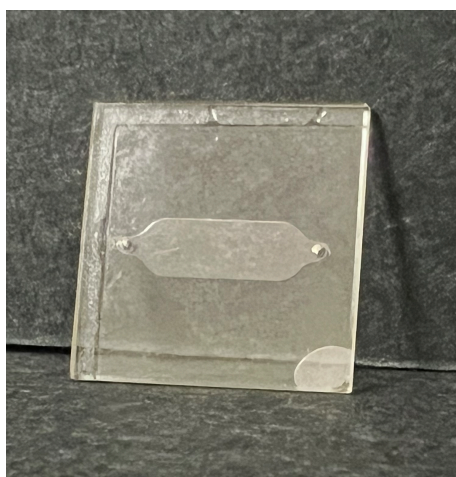
Figure 3.17. Picture of the fabricated fluidic chip using the SU-8 photoresist.

The chip is again tested leaving acetonitrile inside the chamber overnight and after flowing the solvent many times. Then, microscope images are taken and reported in Figure 3.18.
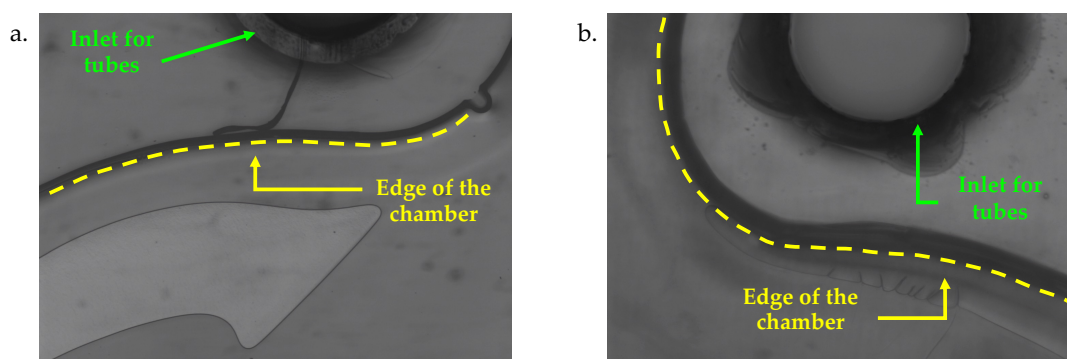


Figure 3.18. Microscope images of the SU-8 chip after testing its resistance to the solvent. Edges are well-defined without defects or indications of damaging. There is not any residual in the chamber.

This time the test is successful since no defects appear at the edges of the chamber, that is then employed for a first set of measurements with chiral solutions. We decide to start with a photonic crystal that comes from the same set of the one of Ref. 53 since we have a full characterization of the design, and it has strong visible modes to refer to. The following measurements have the goal to distinguish the chiral signal from opposite enantiomers of the o-MR-(R)-PEA molecule, so the illumination is now with circular light modulated with the PEM and then demodulated into the amplitude and phase components by the lock-in amplifier. The first step is the acquisition of the baseline signal of the solvent alone. This preliminary test of the setup is crucial since sizeable extrinsic chirality could be introduced by the birefringence of the photonic crystal, information that is not visible when acquiring only the reflectivity signal. We have investigated how the tilt of a different sample affects the amplitude signal in dry condition to optimize the position and to minimize this baseline signal that ideally

should be flat. Examples of curves that can be obtained slightly changing the angle of tilt of the sample are shown in Figure 3.19.
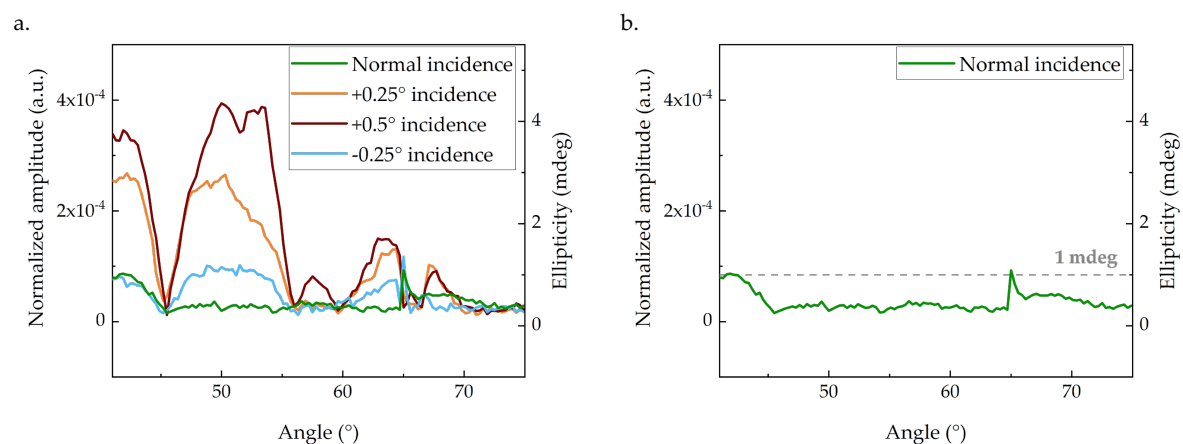


Figure 3.19. a) Amplitude signals of the crystal without chiral element on top. Variations of the tilt position affect the amount of the baseline. b) Optimal condition with a mainly flat baseline.

The tilt position has been rotated by less than 1° to underline the strong dependance of the signal on this parameter, as shown in panel a of Figure 3.19. In particular, a first strong feature appears at low angles when the tilt is not optimized. The small feature around 65° corresponds to the excitation angle of surface waves of the sample under investigation, that for this example is the #DM7.1. At the normal incidence condition, isolated in panel b, the baseline is mainly flat and stays always under a value of ellipticity of 1 mdeg, that represents the common limit of detection of standard CD spectroscopies.[31,88–90] Considering the fluidic environment of work, we decide to optimize further the alignment of the sample when the chamber is filled with acetonitrile. In panel a of Figure 3.20 we show two amplitude signals of the solvent for distinct value of the tilt of the #DM6.1 sample.
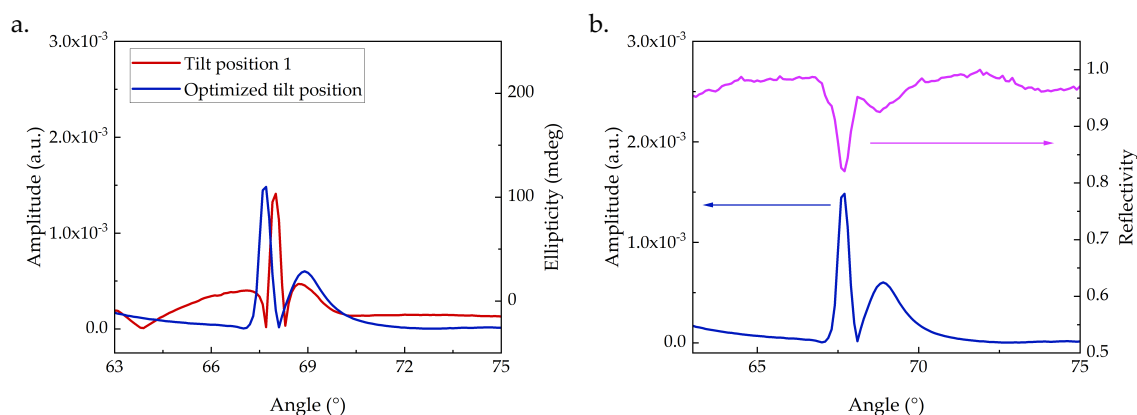


Figure 3.20. a) Variation of the amplitude signal with the tilt. b) Correspondence between amplitude features and surface modes footprint in the reflectivity signal.

The reported behavior is correspondent to two different tilt positions obtained by manually acting on this parameter. One effect of the tilt is the introduction of the red

feature at low angles that, optimizing the position, disappears as happened in the evaluation shown in Figure 3.19. The order of magnitude of the baseline is however significantly worse than the signal acquired and optimized with the photonic crystal alone shown in Figure 3.19, because of the introduction of an absorbing external medium like the solvent but also for the different sample in use, that shows originally more intense modes. The other strong features are, in fact, linked to the two peaks related to the TE and TM surface modes, as is pointed out in panel b, where the angular correspondence between amplitude peaks and dips in the reflectivity is reported. From this second panel one can notice how, with a circular illumination of the platform, both modes are clearly present and partially overlapped, as recorded with separate polarization measurements. The other effect is to slightly change the position of this features, that oscillates around 0.2°. Since the intensity of peaks connected to surface waves seems not to be affected by the tilt optimization, we set the sample position as the one corresponding to the blue curve, with no additional features. Due to the strong response of the solvent, we tentatively decide to use a very high concentrated solution of chiral molecules, set to 20 mM, two orders of magnitude higher with respect to the solutions characterized at the spectrometer, so a higher absorption is expected. Amplitude and phase signals from chiral molecules are reported in Figure 3.21.
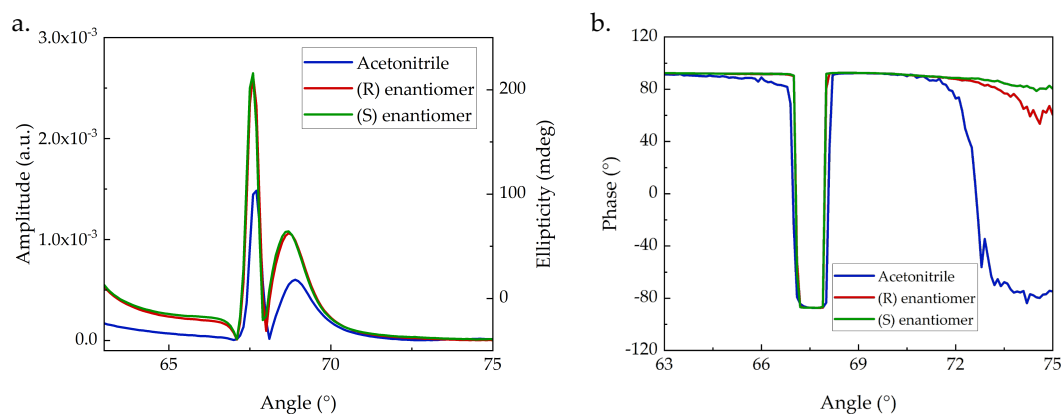


Figure 3.21. a) Amplitude signal comparison between solvent and enantiomers. b) Phase signals of acetonitrile and chiral molecules.

Panel a reports the amplitude signal that, for both enantiomers, is higher than the solvent. (R) and (S) molecules gives the same shape of the amplitude and the phase signals, that are in fact overlapped. This gives CD responses that are overlapped too, as shown in Figure 3.22.
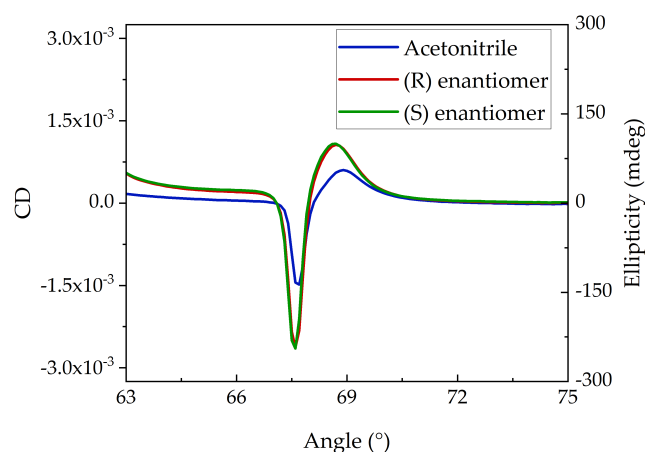
Figure 3.22. CD signal from solvent and chiral molecules.

From here it is possible to distinguish a variation of the signal due to the presence of chiral molecules that can be related to the absorption of the molecular solution. The fact that there are not any differences between the signals from the two enantiomers means that we are still overwhelmed by artifacts, that are themselves enhanced by the absorption of the solution. Since the propagation length of the 1DPC surface modes is around a hundred of micrometers and the diameter of the illumination beam is around 1 mm, the surface mode we collect is only due to the absorption of the materials of the crystal and of the external medium. These preliminary results come from measurements performed on the last days of the PhD activity, leaving the door open to further develop the acquisition technique. One possible solution to collect the CD signal would be for example to reduce the concentration of the molecular solution, to decrease the level of absorption of the external medium. With the high contribution collected with acetonitrile then, it may be possible to obtain only a small improvement. The less concentrated solution can be then tested with a crystal with less intense modes, so that the extrinsic chirality from the platform is limited and the intrinsic chirality of molecules can emerge. The choice of the crystal for the chiral investigation is therefore crucial: from one side, visible and sharp modes are the optimal choice for the optical characterization of surface modes and for the proof of working principle of the platform but probably do not represent the best choice when investigating CD signals. The employment of photonic crystals has still room for improvement and investigation and will be object of study for the near future.

# 4 Chapter four: polarization-resolved spectroscopies

In this chapter, we exploit the simultaneous detection of the TE and TM modes. We first characterize the photonic crystals through a sucrose calibration acquisition curve that determines their sensitivity. Then we work on the immobilization of a relevant blood component on the surface to test our ability to create selective binding sites. We exploit the simultaneous presence of the TE and TM modes by following the layer-by-layer formation of an opposite charged film and finally we test a single-stranded DNA layer, where birefringence is expected, to exploit the possibility to investigate this property thanks to the peculiar polarization of the surface states. All measurements have been performed in collaboration with the group of Biophotonic Sensors and Materials (P.I. Dr. Jakub Dostálek) at the Austrian Institute of Technology.

## 4.1. Sample characterization

The overlap between the dispersion relations of surface modes represents a powerful tool for polarization-resolved spectroscopies because it allows us to investigate the birefringence of adsorbed molecular layers even with a single wavelength of illumination. In fact, having modes superimposed over a broadband spectral range allows one to sense a molecular layer anchored on top of the platform fixing both the angle of investigation and the illuminating wavelength and collecting the response of both modes. This translates into the possibility to distinguish between molecules randomly oriented on the crystal and molecules with an ordered disposition on the surface. The possibility to investigate the orientation of molecules on the surface could lead to different medical applications, for example in the diagnostic field, since many biological tissue components, such as proteins, myosin and elastin can be described as birefringent fibrils.[91] Before going into biologically relevant applications, it is necessary to fully characterize the sensitivity and performance of the 1DPC in use. We selected two samples from the available ones that show a strong TE mode and where the TM is well-recognizable to facilitate the fitting and tracking of resonances. The first sample under investigation, which will be employed for the measurements described in section 4.2, is labelled #DM2.4 and has a design with thicknesses decreased by a factor 10% with respect to the reference sample in Ref. 53 (see Table 1 in Chapter 3). The

mode characterization of the sample in an aqueous environment is discussed in Chapter 3, where both reflectivity maps and angular scans at fixed wavelength are shown. The sensitivity of the samples is estimated through a refractometric calibration using solutions with well-known refractive index. For this purpose, we use home-made sucrose solutions of different concentrations and whose refractive index is tabulated in laboratory manuals. The calibration is shown in Figure 4.1 where home-made sucrose solutions whose concentration spans from 1% to 10% are used.
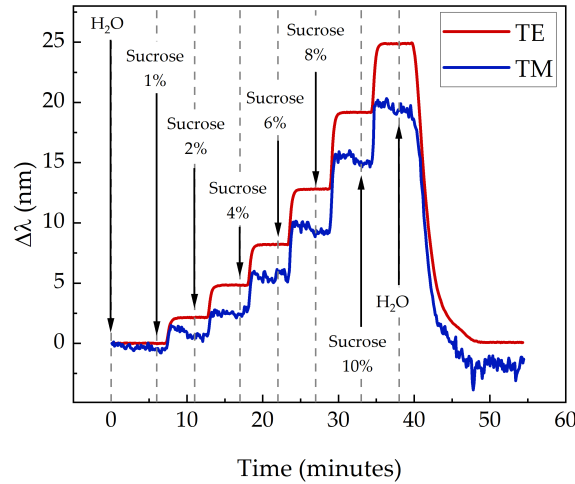


Figure 4.1. Sucrose calibration of sample #DM2.4. The curve is obtained by spectrally following the position of the TE and TM modes and then plotting the shift relative to the initial position in water as a function of time. Arrows indicates the moment when the solution is injected into the fluidic pump.

The step-like curve is obtained fixing the angle of illumination at $\theta = 66.7°$ so that the TE mode is positioned around 450 nm and the TM one has the resonance around 465 nm due to the only partial overlap of the two modes. The measurement consists in following the spectral position of the minimum of the TE and TM resonances in time, as a function of the sucrose solution in the fluidic chamber. Each step corresponds to a variation of the refractive index of the solution. The sharp changes in the position of the resonances correspond to bulk refractive index variations, meaning that the entire tail of the evanescent field in the direction perpendicular to the surface is covered. Each solution is then kept for around 5 minutes in the chamber, till the stabilization of the signal. Then, the time evolution of the TE and TM mode dips is plotted in terms of $\Delta\lambda$, where the reference position is the one in water. Looking at the curves, one can notice how the TE signal has a better signal to noise ratio with respect to the TM one, which is related to the different intensity and shape of the modes. The TE one, narrower and more intense, is easier to follow and fit with respect to the weak TM, introducing different levels of noise. The noise level is however always lower that the signal, making the two curves reliable for the calibration. From this kind of curve, it is possible to estimate the bulk sensitivity of the platform in terms of nm/RIU. This is shown in Figure 4.2, where the experimental sensitivity is compared to the numerical one.
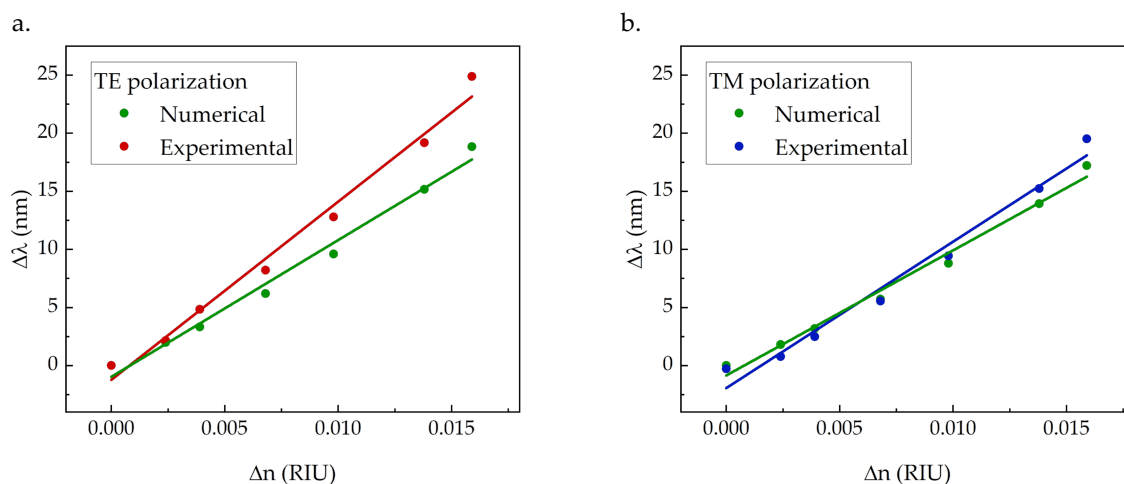
Figure 4.2. a) Comparison between experimental and numerical sensitivities of the TE mode. b) Comparison between experimental and numerical sensitivities of the TM mode.

The experimental sensitivity is extracted by averaging the $\Delta\lambda$ of the calibration curve over the flat part of each step, then plotted as a function of the nominal variation of the refractive index in the solution. The numerical sensitivity is obtained by simulating reflectivity spectra at fixed angle and then fitting the resonance with a Lorentzian curve, extracting the minimum position. Thicknesses of the simulated layers are taken from the ellipsometry characterization of the sample performed immediately after the fabrication step. Both experimental and numerical sensitivities are then found by linear fitting of discrete points. Experimental sensitivities are 1534 nm/RIU for the TE mode and 1260 nm/RIU for the TM mode, while numerical simulations give 1176 nm/RIU as TE sensitivity and 1076 nm/RIU as TM sensitivity. In general, the TE mode is more sensitive with respect to the TM mode as experimentally collected and the numerical sensitivity is slightly lower with respect to the experimental one, but values are comparable, ensuring the reliability of the modeling of this sample. Moreover, looking at both experimental and numerical points, a non-perfect linearity can be noticed, which can be ascribed to a wavelength dependance of the sensitivity, as it will pointed out later in this Chapter. The other platform under investigation is the #DM1.3, whose design has thicknesses of layers slightly larger than the reference sample described in Ref. 53 and whose applications are described in sections 4.3 and 4.4. We performed the same calibration of this sample at two different angles, as shown in Figure 4.3.
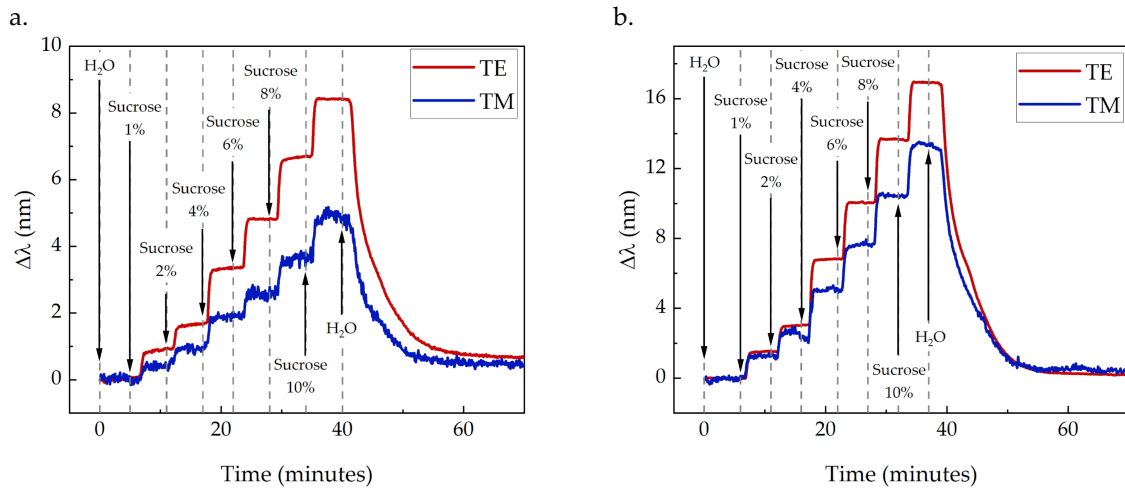
Figure 4.3. a) Sucrose calibration of sample #DM1.3 fixing the angle of illumination at θ = 73.5°. b) Sucrose calibration of sample #DM1.3 fixing the angle of illumination at θ = 68.7°.

Panel a shows the curve when the angle of illumination is fixed at θ = 73.5°. The excitation wavelength of the resonances is around 420 nm for the TE mode and around 470 nm for the TM mode. It is worth noticing that the mode superposition of this sample is worse than the #DM2.4 one, where the misalignment of the modes is only about 15 nm, but this underlines the high dependance of the quality of the sample on the design and fabrication process. Moreover, it is possible to notice that the sensitivities of the two samples are remarkably dissimilar, and this can be related to the distinction of samples but also on the different angle of illumination, linked to the wavelength of investigation. To observe the wavelength dependance of the calibration, one can look at panel b, which reports the curve obtained following the same calibration process but fixing the angle of illumination at θ = 68.7° corresponding to an initial wavelength of the TE mode around 470 nm and the TM resonance around 510 nm. If the qualitative behavior of the modes keeps its trend, with the TE mode that is more sensitive than the TM one and whose signal to noise ratio is higher, comparing panel a and b it is possible to notice that the sensitivity of both modes increases with the wavelength. In fact, we move from a sensitivity of 595 nm/RIU for the TE mode around 420 nm to a sensitivity of about 1320 nm/RIU when we move to about 470 nm. The same happens for the TM sensitivity, which increases from about 340 nm/RIU to 910 nm/RIU. The acquisition of calibration curves then allows assessing the sensitivity of the samples under investigations and also points out that this parameter has a strong wavelength dependance, that will be further explored in section 4.4 of this Chapter.

## 4.2.  Layer-by-layer measurement

The first investigation to approach polarization-sensitive spectroscopy of biological samples is the validation of the ability of our platform to monitor mass density

variations at the surface. This refractometric verification is performed through a well-established technique for plasmonic sensor validation: a layer-by-layer (LbL) assembly of PDADMAC and PSS layers.[92,93] It consists in the sequential input of (+) and (−) charged solutions to create layers thanks to the coulombic interaction. This kind of surface geometry allows one to have a controlled bottom-up modification of the surface, and it was already tested with different substrates.[93–95] The experimental curve is shown in Figure 4.4 where PDADMAC (+) and PSS (-) charged solutions, with a 1 mg/mL concentration, are flown on top of the #DM2.4 1DPC surface.
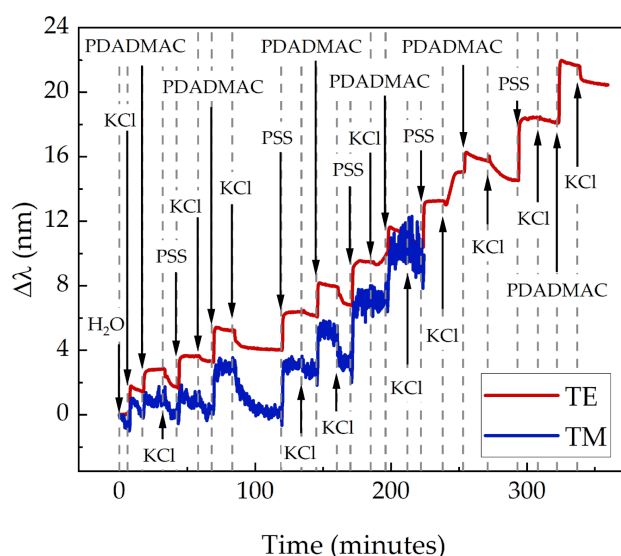


Figure 4.4. Layer-by-layer assembly of PDADMAC and PSS charged layers on top of the 1DPC surface. The spectral shift of the TE and TM modes is reported taking their spectral position in water as reference. The TM mode is visible up to the seventh layer, while the TE mode is tracked up to the eleventh, and the measurement stops only because of a matter of time.

The figure shows the evolution of the position of the TE and the TM resonance when tracked simultaneously in time fixing the angle of illumination at $\theta = 66.7°$ and plotting the result using the spectral position in water as a reference. The first point is in fact acquired filling the fluidic chamber with water and taken as reference since it corresponds to the external medium used for the characterization of samples. The second step is the addition to the chamber of the buffer of the two charged solutions, that is KCl 100 mM. The buffer has the task to keep the PH of the solution constant, otherwise it could affect the optical and chemical properties of the solutes. So, the KCl buffer solution is kept in the chamber for 10 minutes, until the signal saturates. Then, the two charged solutions are alternatively put in contact with the photonic crystal surface for 15 minutes until the saturation of the signal, which corresponds to the formation of the charged layer. After each association phase, which corresponds to a step in the kinetic signal, the buffer solution is again flown into the chamber for 10 minutes to remove elements that are not bound to the surface. Even if the step-like behavior of the curve is the same for the TE and TM curve, the signal to noise ratio is very different, with the TM noisier with respect to the TE one. This is something that

we have already observed with the sucrose calibration, and it is due to the broad and weak shape of the TM resonance. Consequently, it is possible to follow the formation of up to 11 charged layers with the TE mode (only limited by the duration of the measurement, that lasts for about 8 hours) while only 7 layers can be investigated with the TM mode due to its progressive weakening as the wavelength increases as we already observe with simulations. So, focusing on the first 7 layers where both modes are acquired, it is possible to distinguish between the two charged solution association/dissociation phases by looking at the shape of the curves. If the positive PDADMAC produces a sharp saturation of the curve, with also a sharp decrease of the signal at the beginning of the dissociation phase, the negative PSS solution responds with a smoother saturation of the signal, followed by another smooth transition with the buffer solution. Starting from this curve, it is possible to evaluate the thickness of each immobilized layer by fixing the average refractive index of the two solutions equal to 1.476 (as estimated in Ref. 92 for a wavelength of 633 nm). Numerical simulations are performed by calculating reflectivity signals at fixed angle of the sample and extrapolating the minimum of the resonances by Lorentzian fit. Layers with refractive index of 1.476 are then sequentially added setting their thickness as a free parameter. For each of the 7 simulated layers, the thickness is varied until the numerical spectral shift recollects the experimental one. With this kind of analysis, we obtain an average thickness of each formed layer of about 1.3 nm, slightly overestimated with respect to Ref. 92. This discrepancy could be due to the different spectral region of investigation, since the shift depends on the combination between refractive index and thickness, and we use the refractive index estimated with red light. This evaluation gives an idea of the sensitivity to surface variations instead of bulk variations of the refractive index, tests the ability of the platform to sense thickness variations of about 1 nm and shows the ability to distinguish between different association and dissociation processes.

## 4.3.   Thrombin immobilization measurement

The first measurement performed on sample #DM1.3 aims to test the optical performance of our platform by tracking a biologically relevant process: the immobilization of thrombin on top of the dielectric surface. As a crucial enzyme for hemostasis, thrombin controls bleeding in healthy people by starting coagulation. Its imbalance could result in thrombosis or hemorrhage, which are serious disorders accompanied by excessive bleeding, pulmonary embolism, stroke, or myocardial infarction.[96,97] As a result, in clinical practice, the blood's thrombin concentration is a crucial measurement. It specifies the anticoagulant approach to be used when patients are undergoing heart surgery, extracorporeal membrane oxygenation treatment, or even dialysis. Notably, administering excessive dosages of anticoagulants directly derives from the lack of tools to detect shifts in the concentration of this biomarker. The patient may experience hemorrhages for a period after starting the

anticoagulation, even though it may be later reversed (if an indirect test reveals that the levels of thrombin are too low). To minimize hemostatic consequences and customize anticoagulant medication, new biosensor technologies for quick thrombin measurement represent a potential approach. One of the most limiting obstacle impeding their advancement in clinical applications is the unspecific interaction of blood-derived elements with the surface of affinity biosensors (fouling) because it prevents the reading of the specific sensor signal.[98] The specific detection of elements in an untreated blood sample is therefore the final goal. We decide to employ the photonic platform to test its ability of specific sensing of thrombin using DNA aptamers since they can be created in a test tube, generated in large quantities by chemical synthesis and represent an appealing substitute to protein recognition elements. We refer to the work in Ref. 99 where the thrombin binding is sensed using a surface plasmon-based sensor made of gold. The first difference is then in the material of the surface under investigation. Since the surface of the 1DPC is made by $SiO_2$, that is a dielectric material without free charges on the surface and without any specific binding site, we need to prepare the surface to accommodate the DNA aptamer. To this aim, ozone cleaning is performed for 30 minutes to activate the surface, creating negative charges that allow for the coulombic interaction with flowed components. After the activation, the sample is mounted on the experimental setup and the first reference point is taken by flowing water inside the fluidic chamber. Every shift of the resonance is then referred to this point. For this investigation of biological interest and to test our ability to immobilize biological components on the 1DPC surface we decide to use only the TE mode because of its better signal to noise ratio. The first kinetic curve is shown in Figure 4.5 and follows a protocol of immobilization with few steps guided by the work described in Ref. 99.

a.



b.
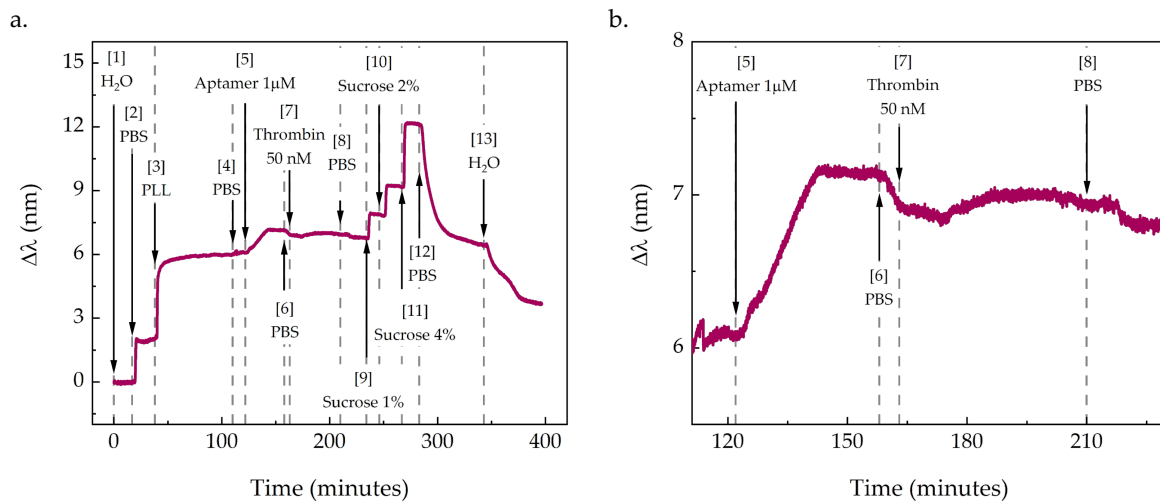


Figure 4.5. a) Spectral response of the TE mode when the protocol of surface preparation and thrombin immobilization are performed. Steps are indicated with numbers and arrows are referred to the moment when the solution is injected in the fluidic pump. b) Zoom of the signal around the specific time interval when thrombin is tentatively immobilized to the surface.

After collecting the water reference, indicated as step 1 in Figure 4.5, for about 15 minutes to check the stability of the signal, we switch to the PBS (phosphate buffer saline) solution (step 2). This is a common buffer solution for biological research that has an almost neutral PH. The sharp change of the signal after injecting the new solution corresponds to a bulk change in the refractive index, meaning that we simply change the external medium. We let the signal stabilize, then we move to the first immobilized layer on the surface, made by poly-L-lysine (PLL, molecular weight between 15 and 30 kDa) (step 3), a positively charged amino acid polymer specifically modified as in Ref. 100 to have additional functional groups.[100] Thanks to the coulombic interaction between the activated surface and the PLL (in PBS) solution, we can form a positive layer on the $SiO_2$ surface. We let the PLL solution flow for about one hour, noting a sharp variation of the signal but with a smooth saturation part with respect to the pure buffer, since now we have the PLL adsorbing onto the surface creating a new layer in our structure. After the PLL signal saturates, meaning that the adsorption process is concluded, we wash the surface with PBS (step 4) to remove all the unbound components. Since the signal remains constant without any negative shift, we can conclude that the PLL is correctly formed. Then we move to the thrombin aptamers (step 5), which were custom synthesized by Integrated DNA Technologies with an amine terminal group called HD22 that would link with PLL modified functional groups. The aptamer solution has a concentration of 1 μM and we let it flow in contact with the surface for 30 minutes, until the saturation of the signal. The kinetics of the binding of HD22 with the PLL layer is completely different from the bulk change that we collect with PBS and PLL, with a first linear increase that then saturates in around 10 minutes. This behavior correctly resembles the one measured in the reference publication 99 using the HD22 aptamer, so we move to the next step flowing

the 50 nM thrombin solution (step 7). We flow the target solution for 30 minutes to let the reaction happen, but we collect a very small shift of the mode. Comparing this shift with the one of Ref. 99, we notice that the variation with the 1DPC is less than expected. This could mean that the thrombin on the surface is bound only in an unspecific way, with random binding and unbinding events on the surface, and not exclusively to aptamer sites that should give the higher response due to the specific immobilization of the protein. One of the possible reasons behind this behavior is the strong coulombic interaction between the aptamer and the PLL layer. Those two components have in fact opposite charges, so the aptamer could lie down on the surface instead of standing on top of it exposing the thrombin specific binding sites. After washing with PBS (step 8), we flow some sucrose solutions (steps 9-10-11) to calibrate the curve and, finally, we go back to PBS (step 12) and water (step 13). One possible solution to the orientation of the aptamer on the surface is to add to our protocol one molecule that prevents this disposition on the surface. Bovine-serum albumin (BSA) is a well-known anti-fouling molecule thanks to its big dimension and high affinity with almost all materials.[101] We try to also exploit its negative charge[102] to help the aptamer to stand on the surface. So, as depicted in Figure 4.6, we repeat the first steps of the characterization till the aptamer flowing but then, before the thrombin, we bring to the surface a 1 mg/ml BSA in PBS solution.
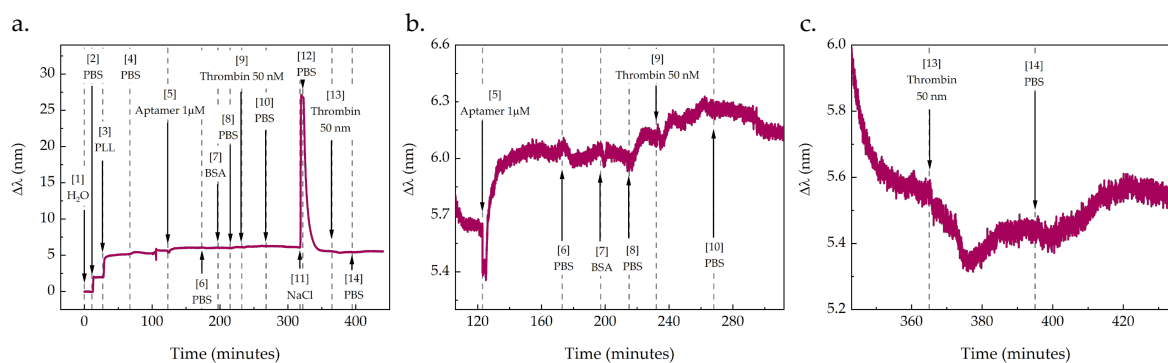


Figure 4.6. a) Spectral response of the TE mode when the protocol of surface preparation and thrombin immobilization are performed with the addition of the BSA molecule. Steps are indicated with numbers and arrows are referred to the moment when the solution is injected in the fluidic pump. b) Zoom of the signal around the specific time interval when thrombin is tentatively immobilized to the surface. c) Zoom of the signal after surface regeneration using NaCl.

The rationale behind this idea is that the repulsive interaction between the two components might help the aptamer stand on the surface while the BSA occupies the free binding sites of the positive PLL layer. However, the near-to-zero variation in the kinetic curve after BSA injection (step 7) suggests that it is not linking on the surface, rather it is probably completely rejected by the negative aptamer layer. Consequently, even this time the signal variation produced by adding the thrombin to the surface is negligible. One other solution then is to regenerate the surface using a 2 M NaCl (step 11) solution. NaCl can break the thrombin-aptamer bond[102] and the charge of the $Na^+$ ions attract aptamers to stand. Even with the surface regeneration, 50 nM thrombin

(step 13) is not giving the expected signal, meaning that there is still something that prevents the specific binding of thrombin despite the high affinity with the aptamer. As a last test, we switch from PBS buffer to PBST, i.e. we add the surfactant Tween 20 to the saline solution, and add BSA to the buffer. With this we directly flow the BSA before the aptamer, hoping that its large dimension can cover the surface and allow only standing aptamers to link on the surface. The resulting curve is shown in Figure 4.7.
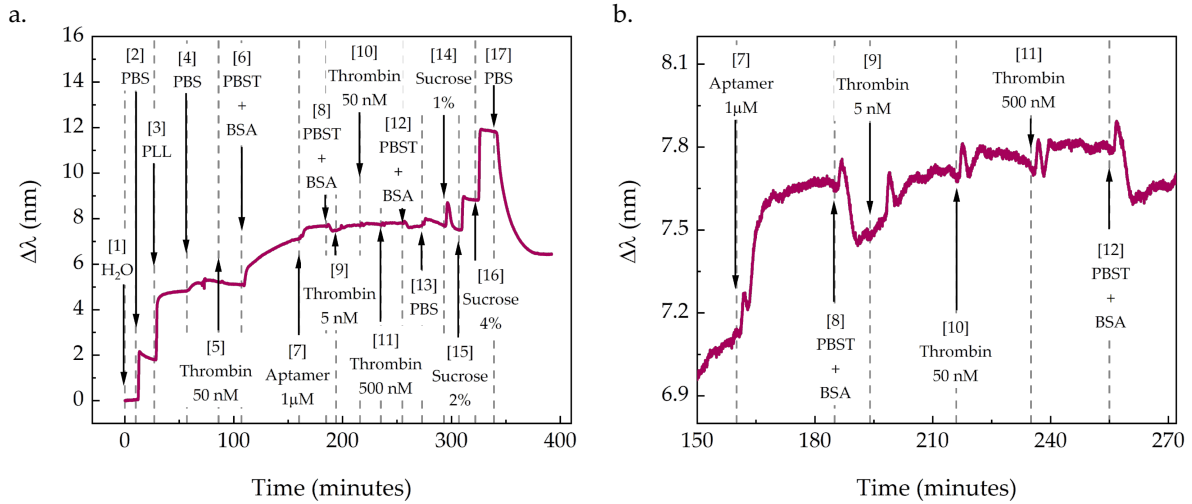


Figure 4.7. a) Spectral response of the TE mode when the protocol of surface preparation and thrombin immobilization are performed switching to the PBST + BSA buffer. Steps are indicated with numbers and arrows are referred to the moment when the solution is injected in the fluidic pump. b) Zoom of the signal around the specific time interval when different concentrations of thrombin solutions are tentatively immobilized to the surface.

The first significant behavior is at correspondence with the flowing of the new composed buffer PBST + BSA (step 6). Here, the curve is not saturating suggesting that multiple layers of BSA are forming on the surface. We decide to stop flowing the buffer after about 30 minutes and switch to the aptamer (step 7). We can still see the typical behavior of aptamer bonding, with small jumps at correspondence with changing of solutions due to fluidic pump issues. When we tried different concentrations of thrombin (steps 9-10-11), the result is again a small increase of the curve probably due to unspecific binding. This time what could have happened is that the thick BSA layer allows the aptamer to bind onto the surface but BSA completely covers the thrombin specific binding sites of the aptamer. The presented results suggest that, even if it seems to be possible to immobilize biomolecules on the surface of a dielectric platform, it is challenging to control the orientation of each biological component to ensure the right affinity and binding, leaving the door open for further investigations on this aspect.

## 4.4.    Rolling Circle Amplification measurement

A further activity we inspect to exploit the simultaneous presence of TE and TM surface mode is a process called "Rolling Circle Amplification" (RCA) that consists in the development of single-stranded DNA (ss-DNA) brushes on top of a surface.[103] All cells contain DNA, also known as deoxyribonucleic acid, which is the genetic material. When cells divide and when organisms reproduce, DNA is passed on and offers the instructions for creating, maintaining, and controlling the cells and organisms. DNA exists in the form of a double helix,[104] which means that every DNA molecule has two intertwined strands. Each chain of the double helix is made by repeated units called nucleotides. Every nucleotide has 3 functional groups: a sugar, a triphosphate and a base. Due to differences in the bases that compose the nucleotides, we have complementary nucleotides that tend to bind, and this interaction is at the basis of the RCA process, where one strand of DNA is developed thanks to a reaction that involves complementary nucleotides. The ss-DNA layer generated with this process is expected to be birefringent[105–107] and so suitable to be investigated by the orthogonal polarization of TE and TM surface modes. The first step of the RCA procedure happens *ex-situ* and it is sketched in Figure 4.8.
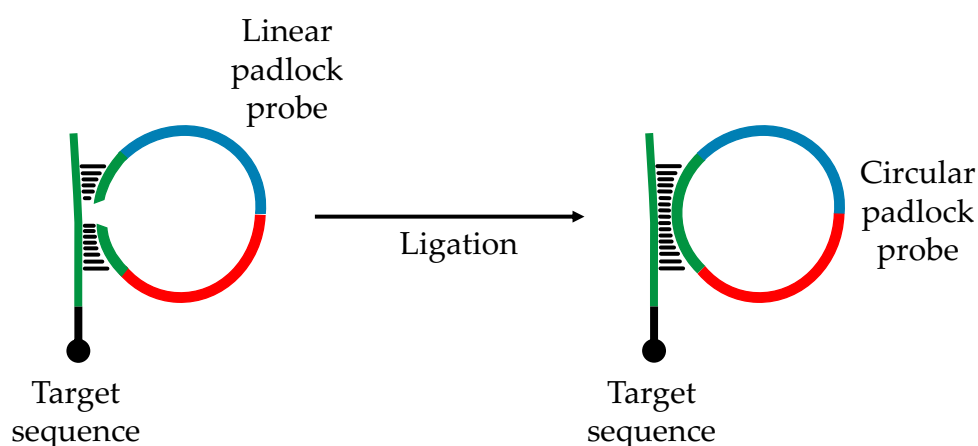


Figure 4.8. Schematic representation of padlock probe preparation through ligation process.

It consists in the preparation of the primer linear probe, a chain of 3 different nucleotides, which is then brought near to a target, made by one complementary group of the primer. This brings to a process called ligation, where the primer closes onto itself into a circle thanks to the interaction with the target. This circular element is called circular padlock probe (PLP) and will be sent onto the surface for the development of ss-DNA. In Figure 4.9 the RCA process on the surface is illustrated.
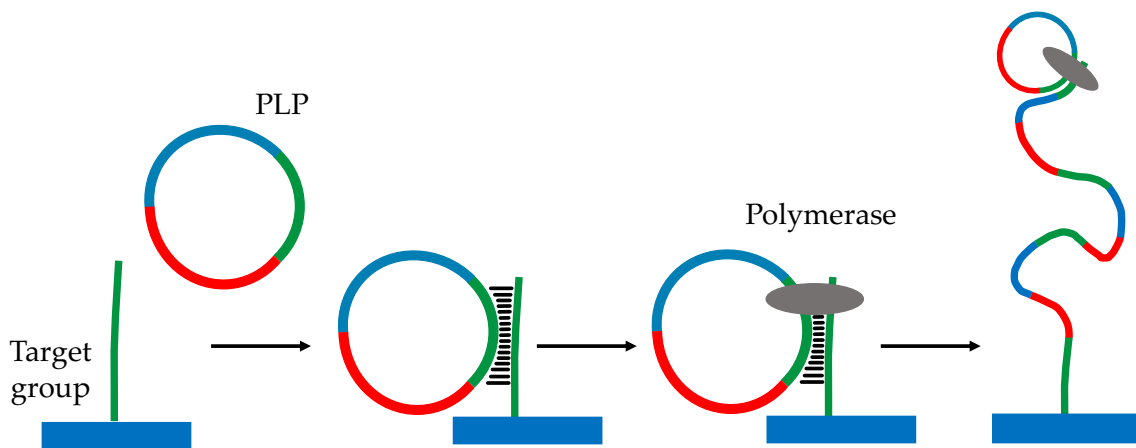
Figure 4.9. Schematic representation of the RCA steps. First, a single target group is immobilized onto the surface. Then the padlock probe links to this group. Afterwards, an enzyme called polymerase is added and it will activate the process. Finally, other nucleotide groups are added and they start to aggregate thanks to the action of the padlock and the enzyme.

The starting point is the immobilization of a first nucleotide group onto the surface. This must belong to the complementary set with respect to the padlock, since it is their interaction that gives rise to the RCA process. The following step is the addition of the PLP to the environment, which links to the target nucleotide thanks to the presence of its complementary component. At this point the growth of ss-DNA is not possible yet; we need to add an enzyme, called polymerase, that fixes the padlock to the target group on the surface and activates the chain reaction. The last step is the addition of nucleotides to the environment solution that allow for the beginning of the reaction. In the first phase in fact DNA brushes are not defined but then, when complementary groups start to aggregate with the padlock thanks to the polymerase, it is possible to grow very long oriented brushes, up to the μm scale. The process is monitored through the acquisition of both TE and TM resonances and then looking at the time evolution of their spectral positions to investigate the expected birefringence of the DNA layer but also to investigate the differences arising in each step of the process. A birefringence of any layer in fact would correspond to a different refractometric response between the TE and the TM mode. The resulting curve is shown in Figure 4.10.
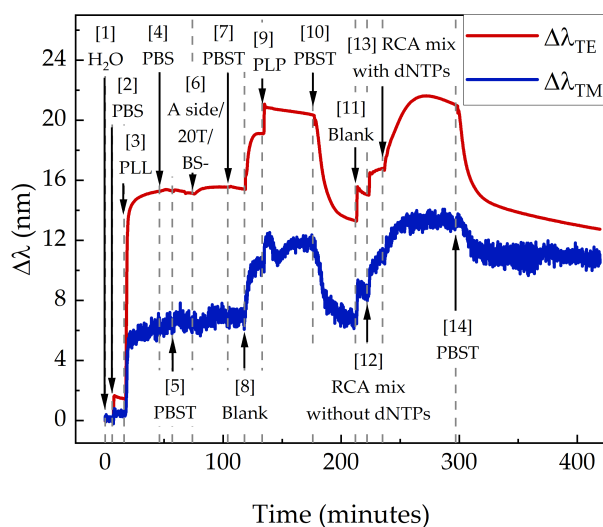
Figure 4.10. Optical signal obtained from the tracking of the TE and TM modes during the RCA process and plotting the spectral shift referred to the first acquisition step in water. Steps of the process are enumerated, and arrows indicate the moment when the solution is injected into the fluidic pump.

The first point is taken as usual in water (step 1), and it acts as a reference for all the spectral shifts induced by the addition of new elements to the surface. Then, we switch to the PBS solution (step 2), which is the buffer for this part of the process. We let the signal stabilize for 10 minutes and then, even if we register a slight drift of the TE curve, we move to the PLL immobilization (step 3). In fact, as for the thrombin immobilization process, also here we need to create some binding sites on the surface to let the first target group stick onto the platform. We use a 0.5 mg/mL solution of PLL flowed on the surface for 30 minutes, then we wash with PBS (step 4) to get rid of unbound elements. At this point we introduce the new buffer PBST (step 5), obtained by the addition of the Tween-20 surfactant, and the first target sequence, called BS- through the A side/20T/BS- 40 nM solution (step 6). It contains the A side group that is specifically chosen to link to the PLL layer thanks to the affinity with specific binding groups of PLL, 20 T means that we are adding on average 20 nucleotides per primer sequence, which could give an idea of the occupied space on the surface, while BS- is the target group that we are immobilizing and that will get in contact with the padlock to start the process. This step takes about 25 minutes and the shape of the curve that we can observe is very different with respect to previous steps. Indeed, we do not have a sharp variation due to a bulk change of the refractive index, but we can see how, step by step, we saturate the surface with the BS- target groups. Afterwards, we wash with the PBST buffer for 15 minutes (step 7) to get rid of all the unbound elements. Then we switch to the new buffer (step 8), the environment of the padlock, which gives a sharp change in the signal since we are now changing the refractive index of the external environment. After 15 minutes the signal is stable, and we introduce the padlock for 40 minutes (step 9) to let it bind to the target group on the surface. We see a sharp change in the signal for both TE and TM modes but then, if the TM mode seems to

saturate, the TE one is decreasing following probably the initial drift. However, after a fixed time of 40 minutes, we wash with PBST for 35 minutes (step 10). In this phase again the TE mode has a significant shift towards shorter wavelengths, going below the wavelength reached after the BS- immobilization. This is probably linked to the initial drift, but we are confident that the padlock is on the surface by looking at the concurrent TM behavior. Then we have again to switch the buffer (step 11) since different components live in different environments, so we observe a further step in the optical signal. At this point the polymerase is added to the surface (step 12). The role of this enzyme is to trigger the binding of new nucleotides to the first target group thanks to the padlock action. Now we have all the ingredients to start the RCA process, which takes place only when we add other nucleotides to the environment (step 13). In this way the padlock catches complementary groups and, while rolling, links them to the first target group thanks to the action of the polymerase. We fix the time of observation of this process to 1 hour, but in principle it could last for a longer time developing longer brushes of the order of micrometers. This is also the part of the signal that we mainly expect to give different responses from TE and TM investigations due to the oriented DNA brushes. At the first sight the shapes of the two curves appear different: the TE mode sharply moves to longer wavelengths, but we do not have a full saturation, with the curve that starts to decrease probably due again to the drift in the detection of the mode. Looking at the blue curve, we see a slower increase of the signal that then saturates, meaning that we have reached the end of the evanescent tail that allows us to detect surface variations. The analysis of this curve shows some points where the shifts from TE and TM modes are different, a good indication that birefringence might be effectively present in some layers. To state something about this property it is however necessary to switch the y-axis of Figure 4.10 from $\Delta\lambda$ to $\Delta n$ using the sensitivity extracted from the sucrose solution reported in Figure 4.3. The resulting curves are shown in panel a of Figure 4.11.
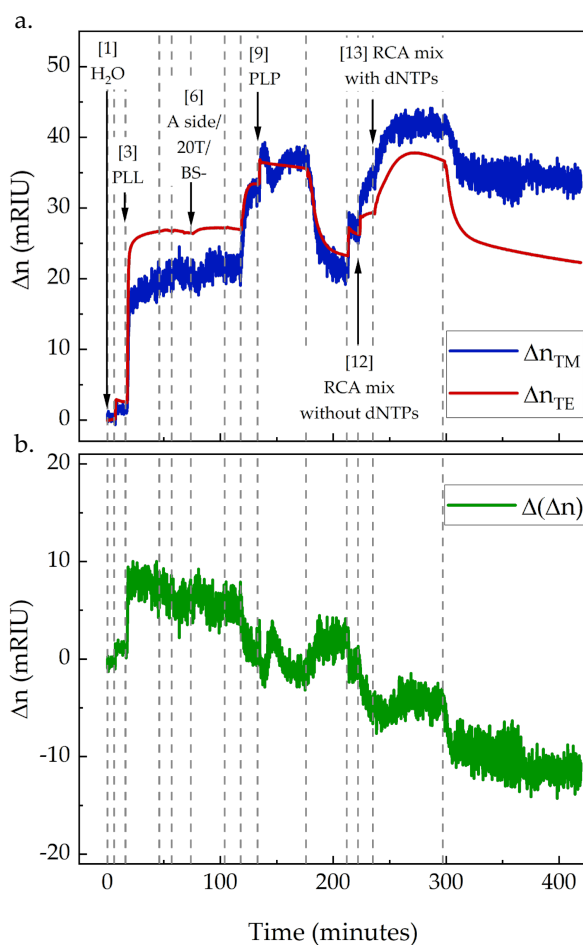
Figure 4.11. a) RCA curve of both TE and TM modes plotted as a function of the refractive index variation and calibrated using the experimental sensitivity extracted from the sucrose characterization of the resonances. b) Differential signal obtained by subtracting the TM response from the TE one. This curve allows to visualize steps where an anisotropic effective index is detected.

We obtain two curves that can be now compared to investigate the birefringence of each immobilized top layer. The difference can be better visualized through the analysis of the $\Delta(\Delta n) = \Delta n_{TE} - \Delta n_{TM}$ signal, as reported in panel b of Figure 4.11. A first remarkable difference comes after the PLL injection (step 3), where it is possible to notice a TE mode response that is stronger than the TM one. This suggests an anisotropy of the PLL layer, that can be related to its helix-like structure and to the standing orientation that this element can assume.[108–110] Then, we have an anisotropic response also after the injection of the blank of the padlock (step 8), that produces a bigger variation in the TM signal with respect to the TE one: this translates into a negative variation in the $\Delta(\Delta n)$ function. The addition of the padlock (step 9) keeps this trend but then, when PBST is used for rinsing (step 10) we have again a positive $\Delta(\Delta n)$ variation. This behavior may be due to changes in the configuration of the molecular layer caused by the flowing of the buffer solutions. The last birefringent response comes from the ss-DNA development (step 13) where the anisotropic response is reverted with respect to the PLL layer (step 3). How the two modes are

propagating inside the different layers depend on the density of elements on the surface and on their orientation. Even if the biological interpretation of this result is still open and a theme of further discussion, it points out the ability of our platform to explore the anisotropic effective index of layers immobilized on its surface. An additional analysis of the curves obtained with the observation of the RCA process is then performed to possibly refine the analysis. To this purpose, we consider through simulations some parameters that can be relevant for the interpretation of the experimental results. So, we start with the numerical fitting of an experimental reflectivity curve to model the photonic crystal. Referring to the experimental results shown in panel a of Figure 4.12, we obtain a design as shown in panel b of the same figure.
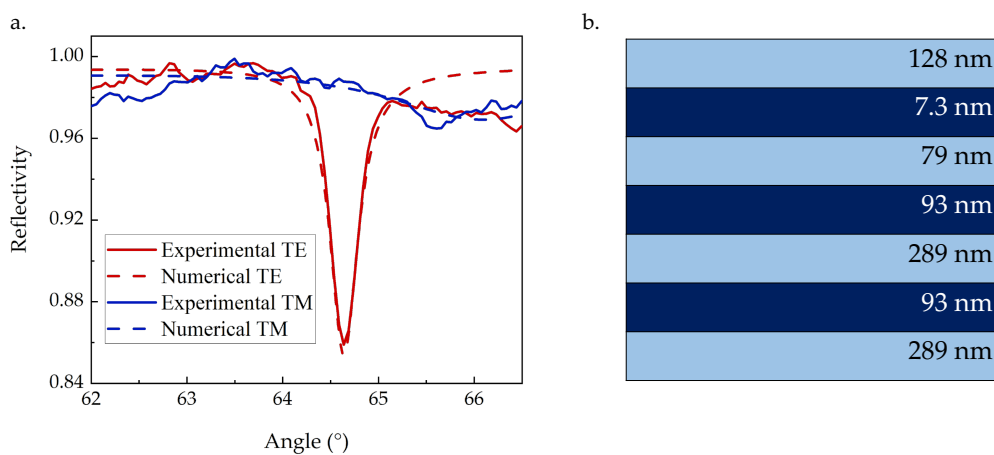


Figure 4.12. a) Sold lines: experimental reflectivity curves obtained by selecting the wavelength of 480 nm from reflectivity maps reported in Chapter 3 for the #DM1.3 sample. Dotted lines: numerical curves that fit the experimental data and give modelled thicknesses of the sample under investigation, as reported in panel b.

Through the genetic algorithm already discussed in Chapter 3, we model the sample under investigation using thicknesses of the layers reported in panel b of Figure 4.12. The parameter we decide to focus on with our simulations is the sensitivity, since we already experienced a strong dependance on this parameter on the wavelength of illumination, as pointed out in section 4.1. We start then from the experimental conversion of the signal from $\Delta\lambda$ to $\Delta n$, that was performed using the sensitivity extrapolated from the sucrose calibration curve of the sample. This sensitivity refers to variation of the refractive index of the external medium of the platform, that we refer to as "bulk", while in the initial steps of the process we immobilize elements whose thicknesses are of the order of few nanometers. This suggests a study of the "surface" sensitivity of the platform, which is discussed in Figure 4.13.
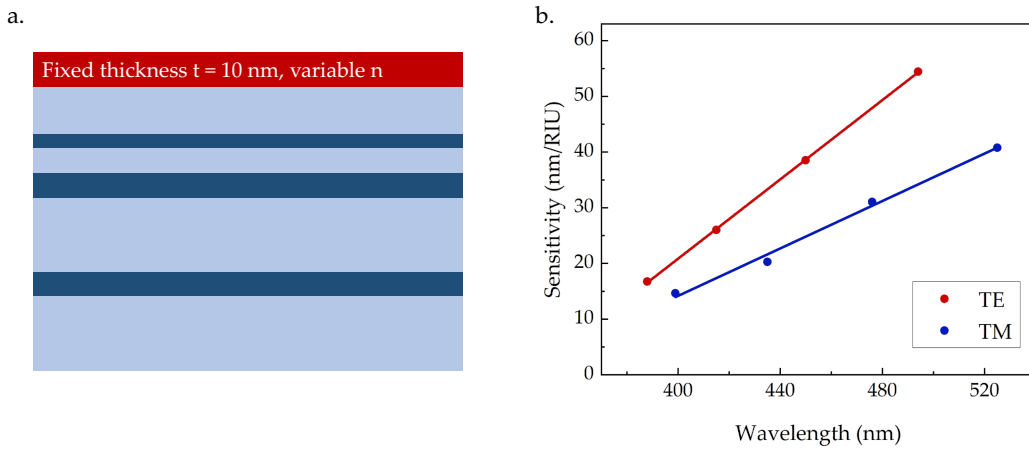
Figure 4.13. a) Sketch of the simulated system. b) Evaluation of the wavelength dependance of the sensitivity through linear fitting.

Panel a shows a sketch of the simulated system, with a top layer with a fixed thickness of t = 10 nm, whose refractive index is changed to evaluate the sensitivity at different distinctive wavelengths. TE and TM sensitivities are plotted as a function of the wavelength of investigation and eventually all data points are linearly fitted. From Figure 4.13 it is evident how the wavelength affects the sensitivity, where a small change of about 10 nm in wavelength could end in a significant variation in the sensitivity. To include this behavior into our data analysis, we extrapolate a conversion formula that allows us to move from the excitation wavelength of the resonance to the variation of the refractive index of the top layer with respect to the reference point in water. So, starting from the definition of sensitivity reported in Equation 4.1:

$$S(\lambda) = \frac{d\lambda}{dn} \tag{4.1}$$

and the linear equation of the fitting of TE and TM sensitivities, generalized in Equation 4.2:

$$S(\lambda) = q + m\lambda \tag{4.2}$$

we combine them to obtain the conversion formula, different for TE and TM investigation, reported in Equation 4.3:

$$n - n_{water} = \Delta n = \frac{1}{m} ln \left( \frac{q + m\lambda}{q + m\lambda_{water}} \right) \tag{4.3}$$

This conversion formula will be used later in this section for the analysis of the experimental RCA curves. Another kind of analysis of the sensitivity can be performed looking at its behavior as a function of the thickness of the top layer. This is because we want to evaluate how the sensitivity of the platform varies during the RCA process. So, we run a new set of simulations where the refractive index of a first top layer is

fixed at 1.45 but the thickness is variable, while a second 10 nm top layer is added with a variable refractive index that allows for sensitivity estimation at a given distance from the crystal surface. A sketch of the simulated system is reported in panel a of Figure 4.14.
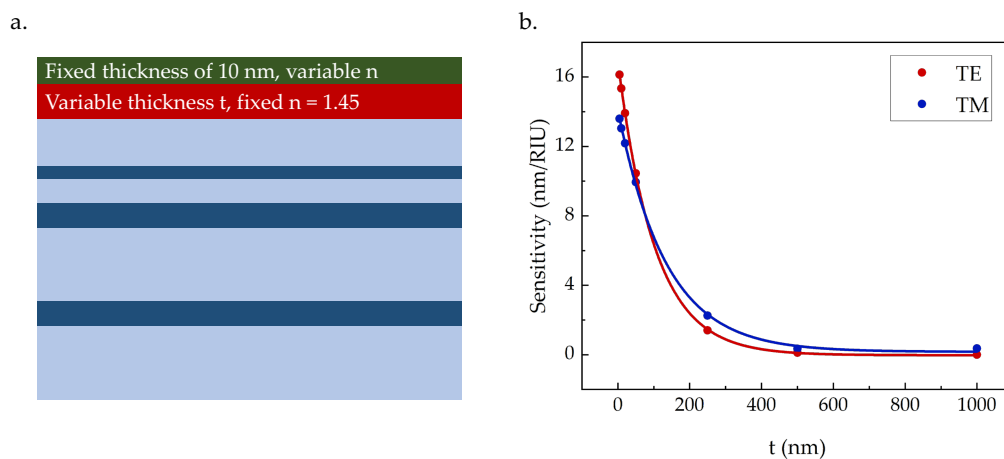


Figure 4.14. a) Sketch of the simulated system. A first top layer has variable thickness t while its refractive index is fixed to 1.45. The second layer has a fixed thickness of 10 nm and variable refractive index, used for evaluating the sensitivity at fixed t values. b) Behavior of the sensitivity as function of the thickness of a first top layer on the crystal surface.

Panel b shows how the sensitivity decreases for both modes as we increase the thickness of the first top layer (colored in red in panel a). With this analysis we point out that the previous knowledge of either the thickness of the immobilized layer or the value of the refractive index is needed to look at acquired signals in absolute quantitative terms. Without knowing one of these parameters, one can work only on the combined effect of the two parameters. With these considerations, we tried to first implement the sensitivity function obtained in Equation 4.3 to recalibrate the RCA curve. The result is shown in Figure 4.15.
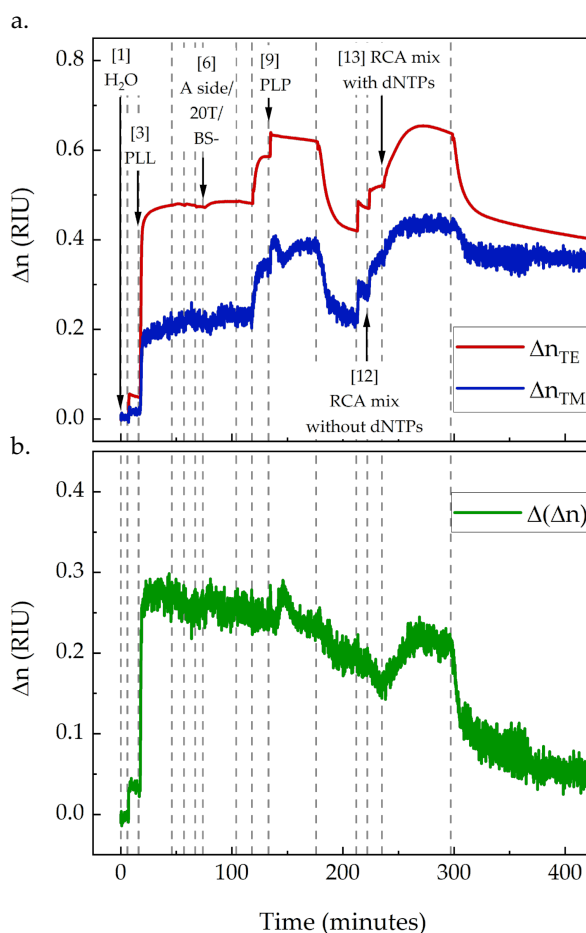
Figure 4.15. Calibration of the RCA curve using the sensitivity calculated in Equation 4.3. TE and TM responses are shown in panel a, together with the difference of the two signals reported in panel b, used for emphasizing steps where birefringence is present.

The curve appears quite different to the one shown in Figure 4.11, obtained with the standard bulk calibration employed in the sensing community. First, the order of magnitude of the variation of the refractive index is higher, in the RIU order. This comes from the fact that now we are using a sensitivity that considers a reduced thickness of the layers, so each spectral shift has a huge variation in the refractive index counterpart. The other difference comes looking at the birefringence of the layers, whose visualization is again facilitated by plotting the $\Delta(\Delta n)$ signal. If in Figure 4.11 we have an opposite behavior at the PLL and the ss-DNA stage, here we have a difference in TE and TM signals that keeps a positive value along the entire acquisition. At the PLL stage the anisotropy has the same trend as in Figure 4.11, with the TE more responsive than the TM, with a positive step in the $\Delta(\Delta n)$ function. It is reasonable to relate it to a standing orientation of molecules with the available binding side protruding through the external medium. Then the $\Delta(\Delta n)$ signal drifts following the TE signal and we have the second positive jump at the correspondence with the ss-DNA growth, where birefringence is effectively expected.[105–107] Differently from Figure 4.11, we collect this time a stronger response of the TE mode, so a positive value of the

Δ(Δn) signal. This discrepancy between the two analysis suggests that still there is room of discussion for including into the analysis of surface signals other parameters like the wavelength- and the distance- dependance of the sensitivity. Even with the described differences, the common point between the different analysis is that the platform detects birefringence in the top molecular layers. This paves the way for a further investigation with polarization resolved spectroscopies. The huge advantage that this platform can introduce, that is not completely exploited here, is the possibility to perform this kind of characterization with monochromatic light, since surface modes are overlapped so fixing the angle of illumination one can follow their kinetic evolution gaining also in temporal resolution of the measurement.

# 5　Chapter five: Optical validation of an EG-FET biosensor

The same optical setup used for the 1DPC optical characterization is employed here in collaboration with the group of Printed and Molecular Electronics (P.I. Dr. Mario Caironi) at the Center for Nano Science and Technology of the Italian Institute of Technology for the validation of a prototype of the transducer of an EG-FET biosensor using Surface Plasmon Resonance (SPR) investigation.

## 5.1.　Motivations and protocol under investigation

The study of biological samples is of great importance for physics, chemistry, medicine and life science.[111,112] In particular, the development of ultrasensitive biosensors could lead to a more sophisticated study of diseases, for examples Parkinson[113] and Alzheimer,[114] on which our knowledge is far from complete. A biosensor is a device that allows one to translate the signal from a biological sample (for example blood) into an electronic signal carrying relevant information for the user. Indeed, the sensor is made by a transducer and an electronic system: the transducer is made by an electronic surface and a bioreceptor and acts as a bridge between the bio analyte and the electronic system that, with a signal amplifier and a signal processor, elaborates the information and show it to the user through a display. In this field, electrolyte gated field-effect transistors (EG-FETs) have attracted increasing attention thanks to their potential for the use in compact and cost-efficient analytical devices.[115–117] An EG-FET biosensor, as sketched in Figure 5.1, is a particular kind of transistor where the dielectric component that passes charges to the semiconductor channel is an electrolyte and the gate acts as the transducer for the biological signal.
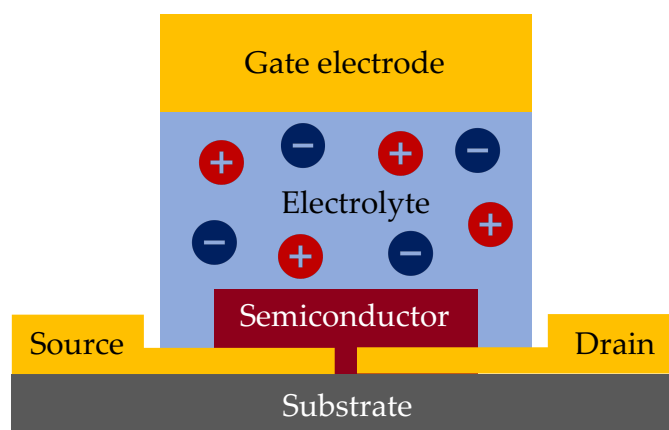
Figure 5.1. Sketch of an electrolyte gated field-effect transistors.

Voltages are usually applied to the drain ($V_D$) and to the gate ($V_G$), while the source is typically set to ground ($V_S = 0$). Depending on the polarity and magnitude of the applied gate voltage, ions drift to the gate or to the semiconductor channel. The semiconductor channel, depending on the type of doping of the material, has enhanced or depleted electronic charges. In both cases, the ionic-electronic modulation produces a variation of the channel conductivity that translates into an electronic current flowing from the source to the drain through the semiconductor. The employment of an EG-FET has many advantages such as a simple device architecture combined with an electronic readout principle, scalable and cost-efficient production, low power consumption (they can operate at low voltages around 1 V thanks to the sub-nanometer scale dimensions of the ions interacting with the gate and channel materials, which results in a large electrostatic interaction at the gate/electrolyte and electrolyte/channel interfaces) and the easy integration as arrays in living systems.[92,118] Moreover, the electrolyte represents a plus since the semiconductor channel is directly immersed in the biological relevant fluid and operations in aqueous electrolytes ensure stability.[119] EG-FETs are already used in many bio-applications such as electroceuticals,[120] bioelectric signal recording[121,122] and biosensors.[123,124] In the field of EG-FET biosensors, the device under investigation in our work has the aim to selectively identify specific antigens in blood. It has gold terminals and belongs to the class of ion-impermeable semiconductor EG-FETs: it allows for the ionic-electronic interaction to happen only at the electrolyte-semiconductor interface. The charged layer collected at this interface is referred to as electronic double layer (EDL). The architecture of the EG-FET under investigation is named "floating gate" and illustrated in Figure 5.2.
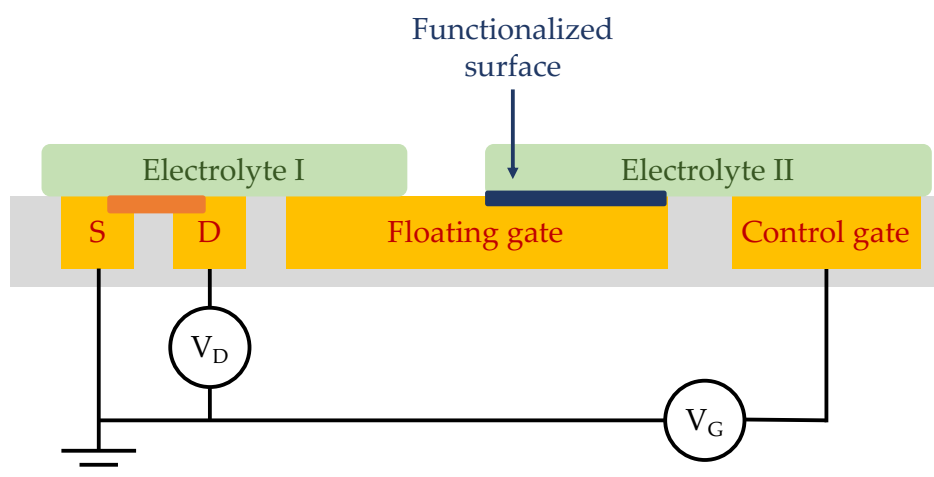
Figure 5.2. Schematic representation of the "floating gate" architecture of an EG-FET.

A floating gate is a gold electrode with two pads that are connected to two distinct electrolyte compartments (I and II). Through the electrolytes, the control gate, where $V_G$ is applied,[125] and the semiconductor channel are capacitively linked to the floating gate. The floating gate configuration has been employed for various sensing applications, such as the transmission of cell electroactivity, although it is most frequently used for biological or chemical sensing.[126–129] For biological sensing applications, capture molecules are fixed in the region of the floating gate in contact with the electrolyte compartment II. The introduced target molecules attach to the functionalized pad and generate an EGT signal in compartment II. The two compartments prevent the target molecules from coming into direct contact with the semiconductor channel in compartment I, preventing in this way non-specific adsorption to it. The floating gate is functionalized with a biorecognition group to be the transducer of the sensor.[130] In particular, the approach used for functionalization includes two bio components: protein G and the IgG antibody. Protein G is used as a binding site for the antibody because it ensures an oriented immobilization on the gold surface.[131] In fact, IgG are Y-shaped molecules with the two fragments that are specific binding sites for antigens.[132] A random orientation of the receptors could result in a loss of the biological activity and a consequent reduction of the transmitted information. IgG molecules, as antibodies in general, are characterized by a large specificity and affinity, that allow binding only selected assays even in a mixture.[133]

Before employing such a platform in an actual biorecognition experiment, it is necessary to validate the transducer functionalization using a well-established technique: Surface Plasmon Resonance. SPR is a very common tool in refractometric sensing thanks to the high sensitivity to refractive index variations on the metallic surface. It manifests itself as a dip in the reflectivity angular spectrum and the efficiency of the excitation is given by the intensity of the dip. Experimentally, the working spectral region of the Ti:Sapphire laser in use is between 680 nm and 1040 nm, with a power peak at 800 nm and a progressive decrease of power and stability at the edges of the region. So as the best compromise the illumination wavelength is set to 680 nm for angular spectra acquisition. The experimental analysis is then performed on a prototype of the actual EG-FET gate, sketched in Figure 5.3: a 50 nm thick gold patch (2 mm x 2 mm) grown on top of a BK7 glass coverslip with the same thermal evaporation setup used for the gate of the EG-FET device.
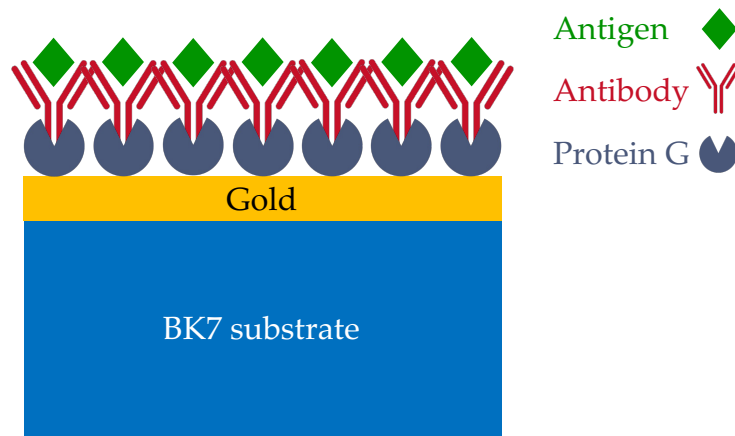


Figure 5.3. Scheme of the immobilized elements on top of the gold prototype gate of the EG-FET under investigation.

To validate the functionalization of the surface, after each step of the immobilization protocol the sample is mounted on the optical setup and angular spectra are acquired. Looking at the shift of the plasmon resonance one can confirm if the binding process was successful and move on with the next step.

## 5.2.  Surface cleaning and protein G addition

A preliminary and important activity is the cleaning of the gold surface. This process plays a key role for the immobilization of assays since the presence of organic components on the surface can lead to artifacts and inefficiency of the functionalization process. In this case the gold chip is treated using sonication in acetone and isopropyl solution followed by plasma oxygen cleaning. This first step also provides the signal from the clean substrate that is then used for referencing the acquired spectra after any immobilization process. The functionalization occurs ex situ, so after each optical step it is necessary to remove the sample from the holder, perform the chemical steps, and

mount it back for the next characterization. This introduces a small misalignment, less than half a degree, in the angular position of the acquired scans, that is post corrected by the alignment of the total internal reflection onset angle, that acts as a reference point during the entire process. In panel a of Figure 5.4 the angular spectrum for the clean bare gold electrode is reported.

a.

b.
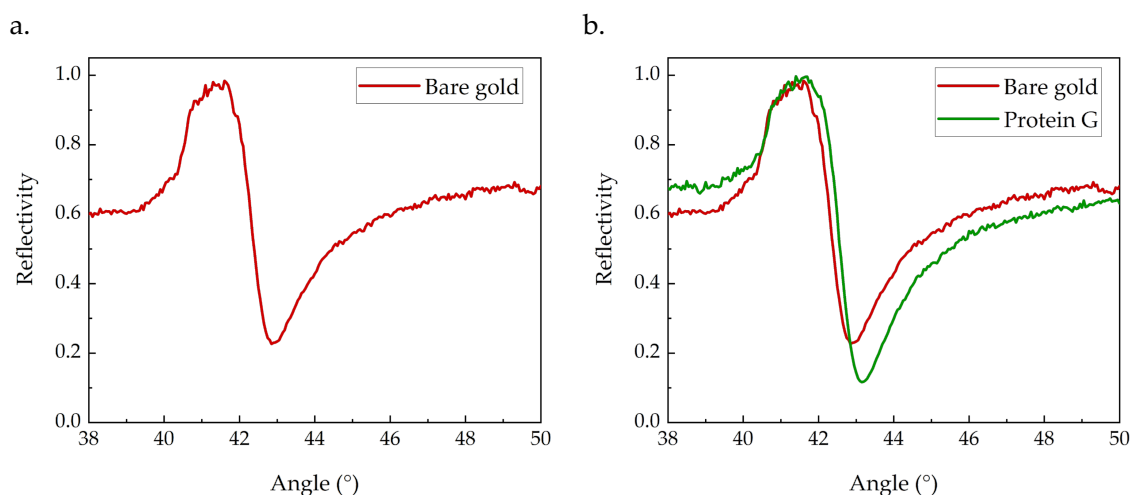
Figure 5.4. a) Reflectivity signal of the bare gold surface after cleaning. This curve acts as the reference angular position for functionalization curves. b) Comparison between the bare gold curve and the one collected after protein G immobilization. A shift of about 0.2° is detected.

One can see the total internal reflection onset around 40.5° and the dip angle related to the excitation of the surface plasmon around 43°. It is the shift of this SPP feature that allows for the tracking of surface refractive index variations and to which all shifts are referred to. After acquiring the reference, a solution of 5 mg/ml of protein G in PBS is drop casted onto the sensor surface and then incubated at room temperature for 4 hours. The binding of protein G onto the gold surface is permitted thanks to the cystine group of the protein, containing sulfur, that has a high affinity with gold. After the incubation of the protein, the sample is rinsed to remove all the unbound elements and it is again optically measured. The acquired spectrum compared to the reference one is reported in panel b of Figure 5.4. Even if small, the shift of the curve is visible and measured to be about 0.2°. It confirms the increase of the refractive index of the top layer due to the immobilization of the protein on the surface and it is a value compatible with previous measurements in literature.[134–136] To further validate the sensing of the immobilized layer, numerical simulations of the system are performed assuming the immobilized protein G as a compact homogeneous layer. The thickness of the protein layer is estimated referring to the documented dimensions of the respective antibody and their molecular weight. The height of an IgG antibody standing on the surface is around 14 nm and its molecular weight is around 150 kDa.[137] Assuming that the dimension of biological elements scales with their molecular weight, the thickness of the protein G layer can be estimated around 2 nm since its molecular weight is 22.6 kDa.[135] Fixing the dimension of the layer and letting the

refractive index change, the shift induced after the protein G immobilization is nicely reproduced with $n = 1.7$, as shown in Figure 5.5, that is compatible with protein refractive indexes that are usually included between 1.5 and 1.7.[138,139]
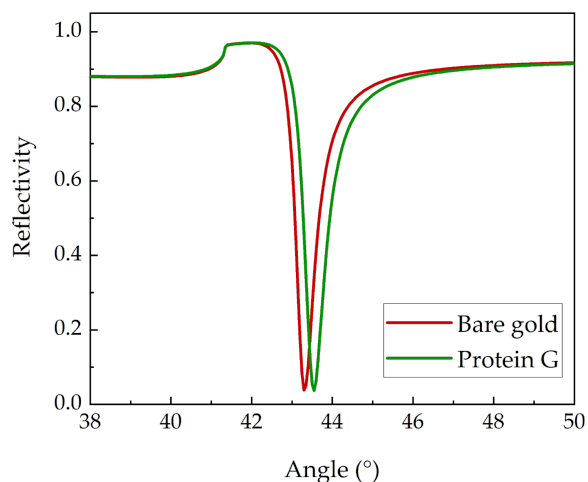


Figure 5.5. Simulated reflectivity curves for a 50 nm thick bare gold surface (red line) and its response after the addition of a 2 nm thick layer with refractive index n = 1.7, resembling the protein G layer (red curve).

Regarding the shape of the resonance, the experimental one is wider with respect to the simulated one. This could be linked to propagation losses of the mode that could be influenced by the material quality, such as the roughness and defects of the surface, and also by ohmic dissipation in the metal, that could be slightly different from the one introduced with the simulated dielectric function.[57] Instead, the bandwidth of the Ti:Sapphire laser, around 15 nm, does not significantly contribute to the broadening of the experimental mode since the contribution that such bandwidth can add is less than 0.2°, negligible with respect to the 1.2° width of the measured resonance.

## 5.3.   Antibody addition

The following step is the addition of IgG antibodies. A 0.1 mg/ml IgG in PBS solution is again drop casted on the prototype gate already functionalized with protein G and incubated at room temperature for 2 hours. After the incubation time the sample is rinsed to remove antibodies that are not bound to protein G sites. The angular scan is then acquired and referred to the bare gold signal, previously taken, as depicted in Figure 5.6 for two different samples.
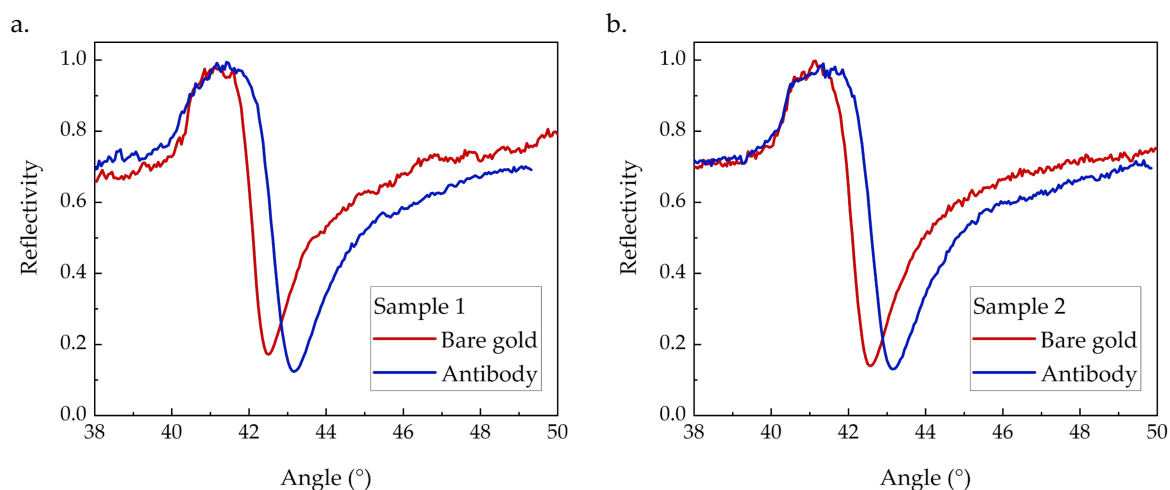
Figure 5.6. Comparison between the responses of two distinct samples (panel a and b) to the addition of the antibody layer on the surface. The red line is acquired with the clean gold surface, while blue lines are referred to the sample functionalized with both protein G and the respective IgG antibody.

The antibody binding produces a larger shift of the resonance with respect to protein G due to the different mass of the component (about 22.6 kDa for protein G while IgG antibodies have a mass of approximately 150 kDa).[137] The collected shift is about 0.6° for both samples, confirming the presence of antibodies on the surface.[134–136] The antibody functionalization analysis also gives the possibility to confirm the sensitivity wavelength dependance previously discussed in Chapter 1. The antibody layer is investigated at 4 different wavelengths: $\lambda = 680$ nm, $\lambda = 770$ nm, $\lambda = 800$ nm and $\lambda = 900$ nm, as shown in Figure 5.7.
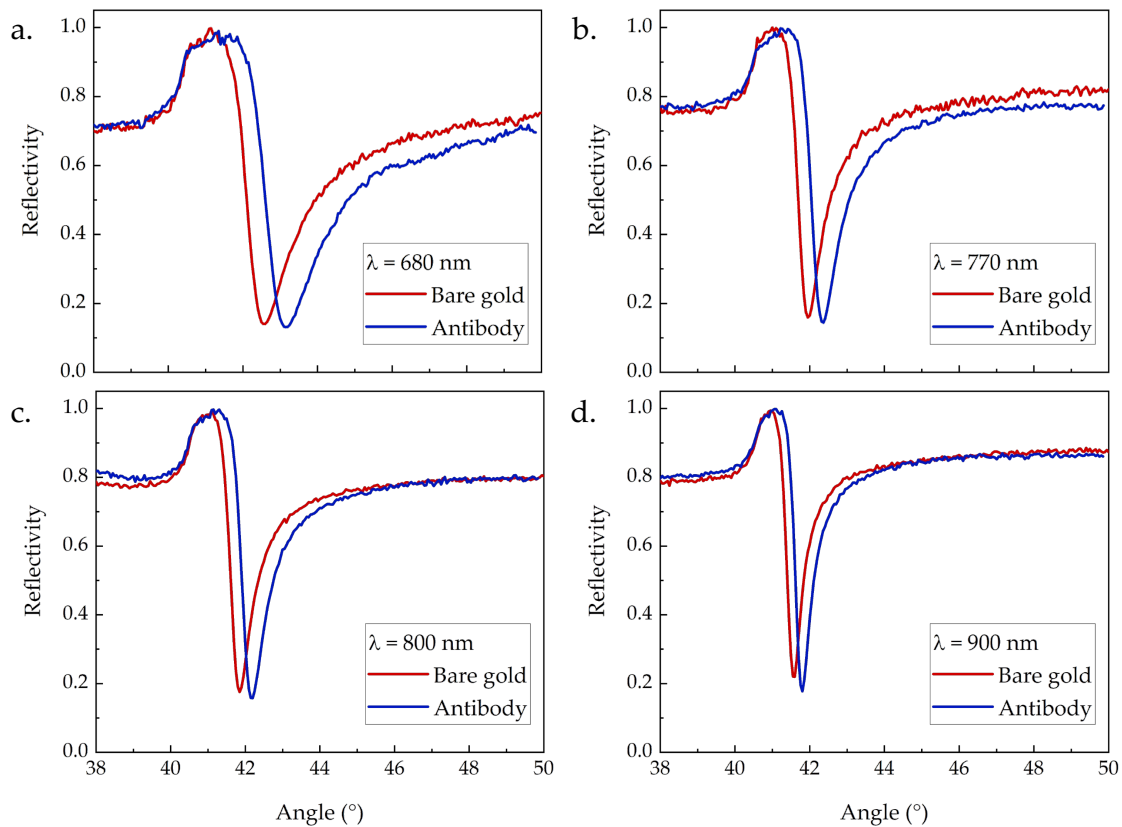
Figure 5.7. Comparison between the bare gold resonance (red line) and the antibody signal (blue line) at a) λ = 680 nm, b) λ = 770 nm, c) λ = 800 nm and d) λ = 900 nm. The shift of the resonance produced by the addition of the antibody layer decreases with increasing λ, as predicted with the estimation of the wavelength dependance of the sensitivity performed in Chapter 1.

Looking at the shift of the resonance feature introduced by the immunoassays layer it is possible to recognize that, effectively, the shift produced at λ = 680 nm is maximum and around 0.6° while at 900 nm the variation in the angular position of the resonance is lower, around 0.2°. With this acquisition the validation of the functionalization process is performed, so it is possible to test the performance of the gate by bringing antigens on the surface and test if the specific binding takes place.

## 5.4.  Antigen bonding validation

Working again on a prototype of the gate of the EG-FET updated with a PDMS gasket on top to allow for fluidic measurements (see Figure 5.8), it is possible to flux antigens on the functionalized gate and track the binding events using SPR.
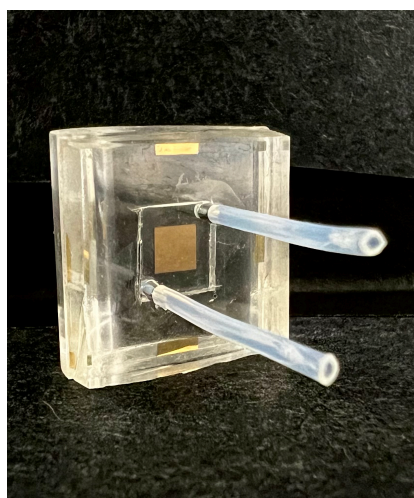
Figure 5.8. Picture of the prototype of the gold gate under investigation fitted with the PDMS fluidic chamber to perform measurements in fluidic conditions.

SPR is in fact frequently used to monitor "real-time" events happening on a metallic surface and represents a complementary information to the one obtained with the FET.[92,140] The focus during this acquisition is to follow the association and dissociation events happening between the antibodies and the respective antigens so dynamic measurements are performed. With the setup in use, it is possible to follow the kinetics of a process using two different and complementary techniques: the fast angular acquisition and the kinetic (fixed angle) acquisition. In both cases the immobilization happens *in situ*, that means that a sample already functionalized with protein G and IgG antibodies is mounted with the PDMS gasket and the binding process is followed without removing the sample from the holder. Another difference is the environment of the characterization: the previous steps are characterized in air, the external medium of the measurement is now the PBS buffer solution of antigens. Both the different configuration and the environment of the measurements bring the necessity of a new reference. This is done by simply flowing PBS in the chamber and acquiring the angular scan. This is crucial since both dynamic measurements are now referred to the position of the resonance when the surface is functionalized, but no antigens are linked to the available binding sites yet. Moreover, since very low variations are expected, the wavelength of investigation is slightly modified to 700 nm, as a compromise between the optimal sensitivity condition and the noise introduced by the tunable light source that works at the edge of its capabilities.

### 5.4.1.  Fast angular scan method

The fast angular scan method is based on tracking of the wavelength shift in the resonance during a surface refractive index change. Since the antigen binding process is expected to be fast, the angular region of investigation is reduced around the resonance dip, then repeated fast scans are performed while flowing the antigen solution. A sketch of the acquisition method is shown in panel a of Figure 5.9.

a.

b.
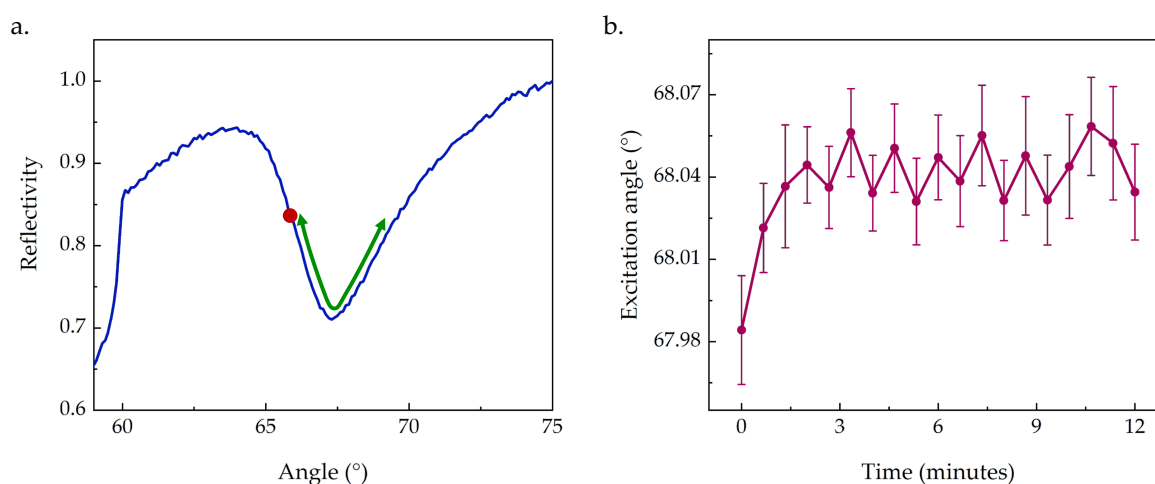


Figure 5.9. a) Experimental reflectivity signal when buffer solution is injected into the fluidic chamber together with a schematic representation of the fast angular scan method of investigation. b) Extrapolated angular positions of the resonance when the antigen solution is brought to the surface. In the first 2 minutes there is a shift of the excitation angle that is linked to the association phase, which then stops when the surface process ends. Error bars are calculated as the standard deviation from the extrapolated value for the minimum of the resonance.

The angular range is set to be from 66.5° to 69.5° with steps of 0.1° while the acquisition time per point is 500 ms. Each scan lasts for about one minute, for a total acquisition time of around 13 minutes while flowing a 6 nM solution of antigen in PBS. Once collected angular spectra, the position of the minimum is extracted through Gaussian fitting and compared to the initial position acquired with the chamber filled with PBS. The resulting plot shown in panel b of Figure 5.9 reports the evolution of the minimum position with respect to the reference one, represented as the 0-time point. During the first 2 minutes there is a sharp shift of the resonance dip probably linked to the association phase of the antigen to the antibody. The molecular weight of antigens is lower than protein G, usually less than 10 kDa,[111] and this could justify the very small, less than 0.1° shift of the dip once the saturation of the process is reached. After 2 minutes the position of the minimum oscillates around 68.04° meaning that the layer is stable, and the association phase is concluded.

## 5.4.2. Kinetic acquisition method

The second technique used for testing the antibody – antigen binding fixes the angle of acquisition and follows the intensity of the reflected beam over time as sketched in panel a of Figure 5.10.
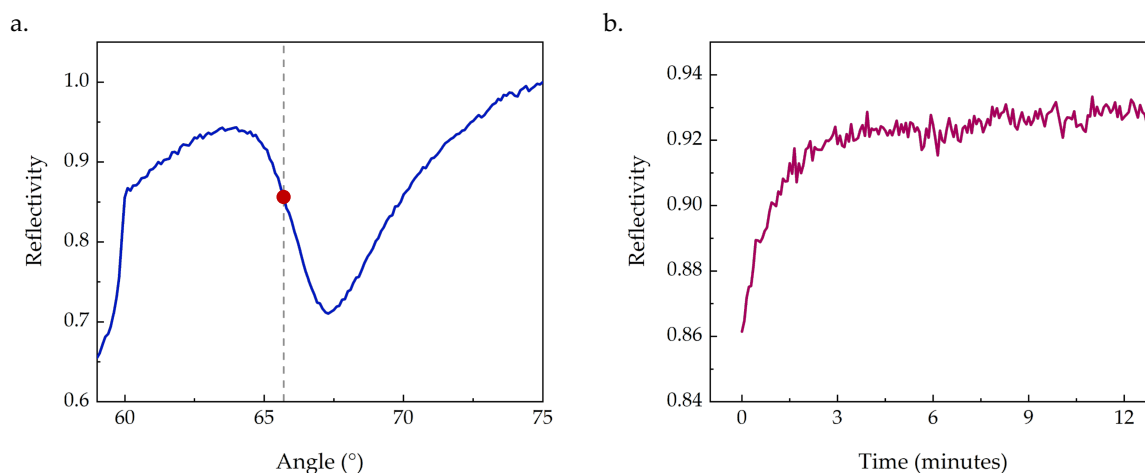
Figure 5.10. a) Experimental reflectivity signal when buffer solution is injected to the fluidic chamber together with a schematic representation of the kinetic acquisition method of investigation. b) Tracking of the reflectivity value at the fixed angle of measurement when the antigen solution is brought to the surface. In the first 2 minutes there is an increase of the signal that is linked to the association phase, that then stops when the surface process ends.

For this kind of measurement, the angular position is chosen around the inflection point of the resonance, around 65.7°. Such position is the most sensitive to variations and following its kinetics it is also possible to state if the resonance is shifted to smaller or bigger angles, meaning decreasing or increasing refractive index of the top layer on the surface. Starting from the buffer, denoted as time 0 in panel b of Figure 5.10, a 6 nM antigen solution is flowed into the chamber for around 30 minutes. As observed with the fast angular technique, the binding process takes around 2 minutes to happen, producing a sharp shift of the resonance towards larger angles, determines an increase of the reflectivity in the kinetic measurement. After that time interval the signal is constant meaning that the association phase is completed, and all available binding sites are now likely occupied. Comparing the two results it is possible to outline a common behavior: in about 2 minutes the association process takes place while afterwards the surface seems to saturate binding sites with only random association and dissociation events.

To conclude, the functionalization process was validated by the reported measurements, confirming that the immobilization of the biorecognition group onto the gold surface is successful and attesting the capability of the home-made optical setup to reach angular sensitivities lower than 0.1°. The antigen immobilization tests are only preliminary measurements performed to push the potentiality of the optical setup to kinetic measurements. From the biotechnology point of view, antigen results could pave the way to a further investigation of the IgG antibody – antigen binding with more sophisticated techniques and immobilization protocols that can give a meaningful outlook in view of the implementation of the system on an EG-FET where optical results can be compared and integrated with electronic measurements.[92]

## 5.5. Electronic measurements

The electronic validation of the functionalization process to confirm the EG-FET operation was performed at the Italian Institute of Technology and measures the drain-source current ($I_{DS}$) as a function of the gate voltage ($V_G$) when the drain-source voltage ($V_{DS}$) is fixed to -0.5 V. A shift of the threshold voltage ($V_T$) obtained by extrapolating the decay value of the exponential behavior of the collected current can be linked to a variation of the configuration of the gate, that is tested for each step of the functionalization. The tested EG-FET, whose prototyped gate was optically characterized, is first cleaned with 15 washing cycles in a 0.5 M $H_2SO_4$ solution. Then, protein G is incubated on the surface of the floating gate for 4 hours before acquiring the current signal. Afterwards, the antibody is maintained on the surface for 2 hours to let the functionalization occur. The drain-source current is then collected and compared with the protein G response as reported in Figure 5.11.
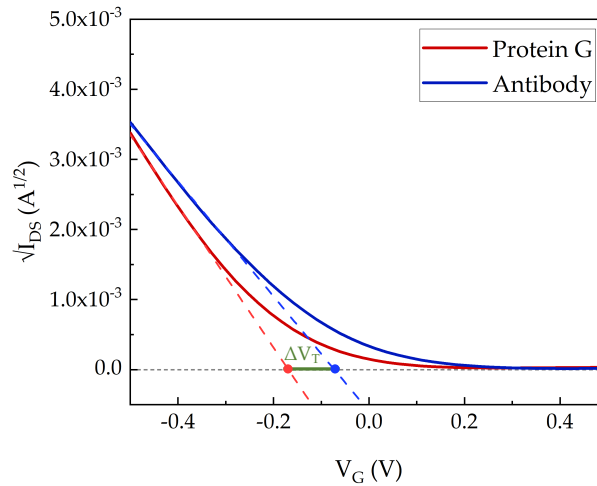


Figure 5.11. Comparison between the electronic responses when the floating gate is functionalized with protein G (red curve) and when the antibody layer is immobilized on top of it (blue curve).

Comparing the two current signals it is possible to observe a threshold voltage shift of about 100 mV that allows us to confirm the successful immobilization of the antibody on the protein G layer. The next step is then to test the binding of the antigen to the correspondent antibody present on the gate of the chip. To prevent unspecific binding, before bringing the antigen to the surface, a bovine-serum-albumin (BSA) solution is incubated for 30 minutes on the surface. BSA plays a well-known antifouling role[101] thanks to its large dimensions and high affinity to a vast variety of elements. A control signal is acquired by injecting testing buffer until reaching a stable I-V signal. After a blank solution is injected for 15 minutes, we bring again the buffer and collect the current signal. This will act as a control curve to compare with the one after antigen immobilization. This procedure is repeated twice to estimate the error in the threshold voltage measurement. The control measurement gives an average threshold shift of 8 mV, as shown in panel a of Figure 5.12.
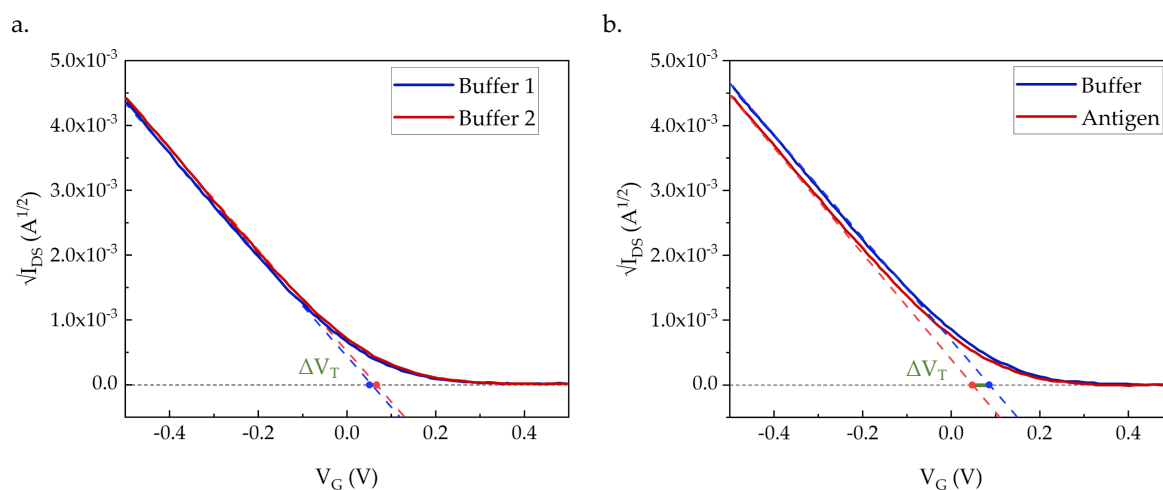
Figure 5.12. a) Comparison between two different acquisitions of the electronic response of the buffer signal. The variation in the threshold voltage represents the noise level of our measurements. b) Comparison between the electric response of the buffer and of the antigen solution. The variation of the threshold voltage confirms the bonding of the antigen on top of the gate surface.

As for the blank, the 6 nM antigen solution is injected onto the gate for 15 minutes and then washed with the buffer to remove unbound elements. The current is collected, and the threshold voltage is calculated. The antigen produces an average shift in the threshold voltage of around 40 mV, validating the ability of the sensor to specifically distinguish the presence of the antigen on the gate, as pointed out in panel b of Figure 5.12. This preliminary characterization is a good starting point for the optimization of the chip and the acquisition procedure, for example implementing a buffer circulating system to decrease the threshold shift in the control experiment. Electrical and optical signals are complementary and show the same behavior when biological components are added, validating the functionalization process.

# 6    Conclusions

The investigation of biological samples has always been of great interest thanks to the possible applications in medicine, pharmacology and life science. The development of tools that allow for the investigation of small quantities of molecular analytes is then of huge interest and represents the main topic of this work. In this field, the employment of surface waves is now well-established, and we focus on both Bloch Surface Waves and Surface Plasmon Polaritons.

BSWs are sustained at the surface of one-dimensional photonic crystals, with the possibility to tune their resonances by fine design materials and thicknesses of the platform. Both polarizations of the surface modes can be sustained, and, in this environment, we propose a platform that allows for the overlap of TE and TM dispersion relations over a broadband spectral range. The first important result shown here is then the experimental demonstration of the surface mode superposition in energy and wavenumber, achieved by the acquisition of reflectivity maps of TE and TM modes to validate their overlap in the visible – UV spectral region. This result represents the first successful experimental demonstration in the literature of degenerate TE and TM BSWs over a broad spectral range.

The simultaneous excitation of TE and TM modes allows for the generation of a so called "superchiral" surface wave, which can be employed for the inspection of chiral molecules through circular dichroism spectroscopy. We performed preliminary CD measurements employing the 1DPC and we experienced an overwhelming "extrinsic" chiral contribution that is introduced by the combination of optical elements of the setup, covering the "intrinsic" chiral signal coming from the molecular structural properties. We studied how we can reduce these artifacts proposing some solutions that will be tested in the near feature. Also, molecular responses in solution have been collected for the estimation of the molecular chiroptical response in view of a future modeling of experimental results.

The TE and TM modes superposition can be also employed for the investigation of the birefringence of a molecular layer since the differential response of the surface modes allows for the distinction between random and oriented molecules anchored to the crystal surface. To exploit this ability, we worked on single-stranded DNA brushes developed onto the platform surface through a process called Rolling Circle Amplification. This technique allows one to grow DNA strands whose length can

reach the order of μm and a birefringence of the layer is expected. We acquire the optical response of the TE and TM modes following the protocol of preparation of the surface and the RCA process itself discovering that also other layers have a birefringent response, and this is now a topic for further discussions and studies. Indeed, we demonstrate our ability to detect the anisotropy of the effective refractive index of a molecular layer paving the way for single-wavelength polarization-resolved spectroscopies. We also suggested that since TE and TM modes have different sensitivities and different extents of the respective evanescent tails, data analysis based on "surface" sensitivities rather than "bulk" sensitivities might be able to shed new light onto the optical response of the anisotropic layer.

SPPs are finally used as well-established tools for the validation of the functionalization protocol of a gold gate belonging to an EG-FET biosensor whose final target is the sensing of a specific antigen in blood. We acquire the reflectivity angular scans of the sample after each step of functionalization to validate the successful immobilization of bioreceptors on the gold surface, recognizable as an angular shift of the resonance. After the demonstration of effective bonding of proteins and antibodies on the gold gate surface, we also tested the ability of the platform to detect the specific antigen immobilization. We used two methods, through fast angular scans to track the variation of the position of the minimum of the resonance, and though the kinetic acquisition of the reflectivity intensity fixing the angle of investigation, collecting the same response, confirming the detection of the antigen. Optical results are supported by electrical measurements, that confirm the ability to immobilize biological elements on the surface and to observe the antibody – antigen association. This confirms the solid operation of the device, that can be then improved for future applications.

To conclude, we explored the potentiality of Bloch Surface Waves and Surface Plasmon Polaritons and their possible applications for the investigation of biologically relevant samples like chiral molecules, DNA and blood components. We plan further developments for each topic, paving the way for future applications of the platforms under investigation.

# Bibliography

1.  Descrovi E, Sfez T, Dominici L, et al. Near-field imaging of Bloch surface waves on silicon nitride one-dimensional photonic crystals. *Opt Express*. 2008;16(8):5453. doi:10.1364/oe.16.005453

2.  Goyal AK, Pal S. Design analysis of Bloch surface wave based sensor for haemoglobin concentration measurement. *Appl Nanosci*. 2020;10(9):3639-3647. doi:10.1007/s13204-020-01437-4

3.  Bulgakov EN, Sadreev AF. Light trapping above the light cone in a one-dimensional array of dielectric spheres. *Phys Rev A - At Mol Opt Phys*. 2015;92(2):1-11. doi:10.1103/PhysRevA.92.023816

4.  Descrovi E, Sfez T, Quaglio M, et al. Guided bloch surface waves on ultrathin polymeric ridges. *Nano Lett*. 2010;10(6):2087-2091. doi:10.1021/nl100481q

5.  Joannopoulos JD, Johnson SG, Winn JN, Meade RD. *Photonic Crystals*.; 2008.

6.  Vigneron JP, Simonis P. Natural photonic crystals. *Phys B Condens Matter*. 2012;407(20):4032-4036. doi:10.1016/j.physb.2011.12.130

7.  Fink Y, Winn JN, Fan S, et al. A Dielectric Omnidirectional Reflector. 1998;282(November):1679-1683.

8.  Wu J, Liang Y, Guo J, Jiang L, Dai X, Xiang Y. Tunable and Multichannel Terahertz Perfect Absorber Due to Tamm Plasmons with Topological Insulators. *Plasmonics*. 2020;15(1):83-91. doi:10.1007/s11468-019-01011-x

9.  Wu F, Lu G, Guo Z, et al. Redshift gaps in one-dimensional photonic crystals containing hyperbolic metamaterials. *Phys Rev Appl*. 2018;10(6):1. doi:10.1103/PhysRevApplied.10.064022

10. Liscidini M, Sipe JE. Analysis of Bloch-surface-wave assisted diffraction-based biosensors. 2009;26(2):279-289.

11. Sinibaldi A, Rizzo R, Figliozzi G, et al. A full ellipsometric approach to optical sensing with Bloch surface waves on photonic crystals. *Opt Express*. 2013;21(20):23331. doi:10.1364/oe.21.023331

12. Li Y, Yang T, Pang Z, Du G, Song S, Han S. Phase-sensitive Bloch surface wave sensor based on variable angle spectroscopic ellipsometry. *Opt Express*. 2014;22(18):21403. doi:10.1364/oe.22.021403

13. Wan Y, Zheng Z, Cheng M, Kong W, Liu K. Polarimetric-phase-enhanced intensity interrogation scheme for surface wave optical sensors with low optical loss. *Sensors (Switzerland)*. 2018;18(10). doi:10.3390/s18103262

14. Farmer A, Friedli AC, Wright SM, Robertson WM. Biosensing using surface electromagnetic waves in photonic band gap multilayers. *Sensors Actuators, B Chem*. 2012;173:79-84. doi:10.1016/j.snb.2012.06.015

15. Kong W, Zheng Z, Wan Y, Li S, Liu J. High-sensitivity sensing based on intensity-interrogated Bloch surface wave sensors. *Sensors Actuators, B Chem*. 2014;193:467-471. doi:10.1016/j.snb.2013.11.101

16. Kang XB, Wen LW, Wang ZG. Design of guided Bloch surface wave resonance bio-sensors with high sensitivity. *Opt Commun*. 2017;383(October 2016):531-536. doi:10.1016/j.optcom.2016.10.004

17. Gryga M, Ciprian D, Hlubina P. Bloch surface wave resonance based sensors as an alternative to surface plasmon resonance sensors. *Sensors (Switzerland)*. 2020;20(18):1-16. doi:10.3390/s20185119

18. Kovalevich T, Belharet D, Robert L, et al. Bloch surface waves at the telecommunication wavelength with lithium niobate as the top layer for integrated optics. *Appl Opt*. 2019;58(7):1757. doi:10.1364/ao.58.001757

19. Robertson WM, May MS. Surface electromagnetic wave excitation on one-dimensional photonic band-gap arrays. *Appl Phys Lett*. 1999;74(13):1800-1802. doi:10.1063/1.123090

20. Byrnes SJ. Multilayer optical calculations. Published online 2016:1-20. http://arxiv.org/abs/1603.02720

21. Kretschmann E. Die Bestimmung optischer Konstanten von Metallen durch Anregung von Oberflächenplasmaschwingungen. *Zeitschrift für Phys*. 1971;241(4):313-324. doi:10.1007/BF01395428

22. Smolik GM, Descharmes N, Herzig HP. Toward Bloch Surface Wave-Assisted Spectroscopy in the Mid-Infrared Region. *ACS Photonics*. 2018;5(4):1164-1170. doi:10.1021/acsphotonics.7b01315

23. Fornasari L, Floris F, Patrini M, et al. Fluorescence excitation enhancement by Bloch surface wave in all-polymer one-dimensional photonic structure. *Appl Phys Lett*. 2014;105(5). doi:10.1063/1.4892423

24. Ferenci P. Review article: Diagnosis and current therapy of Wilson's disease. *Aliment Pharmacol Ther*. 2004;19(2):157-165. doi:10.1046/j.1365-2036.2003.01813.x

25. Smithells RW, Newman CGH. Recognition of thalidomide defects. *J Med Genet*. 1992;29(10):716-723. doi:10.1136/jmg.29.10.716

26. Drezet A, Genet C, Laluet J-Y, Ebbesen TW. Optical chirality without optical

activity: How surface plasmons give a twist to light. *Opt Express*. 2008;16(17):12559. doi:10.1364/oe.16.012559

27.    Plum E, Liu XX, Fedotov VA, Chen Y, Tsai DP, Zheludev NI. Metamaterials: Optical activity without chirality. *Phys Rev Lett*. 2009;102(11):1-4. doi:10.1103/PhysRevLett.102.113902

28.    Sersic I, Van De Haar MA, Arango FB, Koenderink AF. Ubiquity of optical activity in planar metamaterial scatterers. *Phys Rev Lett*. 2012;108(22):1-5. doi:10.1103/PhysRevLett.108.223903

29.    Tang Y, Cohen AE. Optical chirality and its interaction with matter. *Phys Rev Lett*. 2010;104(16):1-4. doi:10.1103/PhysRevLett.104.163901

30.    Tang Y, Cohen AE. Enhanced enantioselectivity in excitation of chiral molecules by superchiral light. *Science (80- )*. 2011;332(6027):333-336. doi:10.1126/science.1202817

31.    Rahman N, Khan S. Circular Dichroism Spectroscopy: A Facile Approach for Quantitative Analysis of Captopril and Study of Its Degradation. *ACS Omega*. 2019;4(2):4252-4258. doi:10.1021/acsomega.8b03384

32.    Hendry E, Carpy T, Johnston J, et al. Ultrasensitive detection and characterization of biomolecules using superchiral fields. *Nat Nanotechnol*. 2010;5(11):783-787. doi:10.1038/nnano.2010.209

33.    Schäferling M, Dregely D, Hentschel M, Giessen H. Tailoring enhanced optical chirality: Design principles for chiral plasmonic nanostructures. *Phys Rev X*. 2012;2(3):1-9. doi:10.1103/PhysRevX.2.031010

34.    Schäferling M, Yin X, Engheta N, Giessen H. Helical Plasmonic Nanostructures as Prototypical Chiral Near-Field Sources. *ACS Photonics*. 2014;1(6):530-537. doi:10.1021/ph5000743

35.    Nesterov ML, Yin X, Schäferling M, Giessen H, Weiss T. The Role of Plasmon-Generated Near Fields for Enhanced Circular Dichroism Spectroscopy. *ACS Photonics*. 2016;3(4):578-583. doi:10.1021/acsphotonics.5b00637

36.    Abdulrahman NA, Fan Z, Tonooka T, et al. Induced chirality through electromagnetic coupling between chiral molecular layers and plasmonic nanostructures. *Nano Lett*. 2012;12(2):977-983. doi:10.1021/nl204055r

37.    Schäferling M, Engheta N, Giessen H, Weiss T. Reducing the Complexity: Enantioselective Chiral Near-Fields by Diagonal Slit and Mirror Configuration. *ACS Photonics*. 2016;3(6):1076-1084. doi:10.1021/acsphotonics.6b00147

38.    Govorov AO, Fan Z, Hernandez P, Slocik JM, Naik RR. Theory of circular dichroism of nanomaterials comprising chiral molecules and nanocrystals: Plasmon enhancement, dipole interactions, and dielectric effects. *Nano Lett*.

2010;10(4):1374-1382. doi:10.1021/nl100010v

39.   Govorov AO, Fan Z. Theory of chiral plasmonic nanostructures comprising metal nanocrystals and chiral molecular media. *ChemPhysChem*. 2012;13(10):2551-2560. doi:10.1002/cphc.201100958

40.   Hendry E, Mikhaylovskiy R V., Barron LD, Kadodwala M, Davis TJ. Chiral electromagnetic fields generated by arrays of nanoslits. *Nano Lett*. 2012;12(7):3640-3644. doi:10.1021/nl3012787

41.   Schäferling M, Yin X, Giessen H. Formation of chiral fields in a symmetric environment. *Opt Express*. 2012;20(24):26326. doi:10.1364/oe.20.026326

42.   Lu F, Tian Y, Liu M, et al. Discrete nanocubes as plasmonic reporters of molecular chirality. *Nano Lett*. 2013;13(7):3145-3151. doi:10.1021/nl401107g

43.   Wang Z, Wang Y, Adamo G, et al. A Novel Chiral Metasurface with Controllable Circular Dichroism Induced by Coupling Localized and Propagating Modes. *Adv Opt Mater*. 2016;4:883-888.

44.   Liu Y, Wang R, Zhang X. Giant circular dichroism enhancement and chiroptical illusion in hybrid molecule-plasmonic nanostructures. *Opt Express*. 2014;22(4):4357. doi:10.1364/oe.22.004357

45.   Valev VK, Baumberg JJ, De Clercq B, et al. Nonlinear Superchiral Meta-Surfaces: Tuning Chirality and Disentangling Non-Reciprocity at the Nanoscale. *Adv Mater*. 2014;26:4074-4081.

46.   Collins JT, Kuppe C, Hooper DC, Sibilia C, Centini M, Valev VK. Chirality and Chiroptical Effects in Metal Nanostructures: Fundamentals and Current Trends. *Adv Opt Mater*. 2017;5(16). doi:10.1002/adom.201700182

47.   Finazzi M, Biagioni P, Celebrano M, Duò L. Quasistatic limit for plasmon-enhanced optical chirality. *Phys Rev B - Condens Matter Mater Phys*. 2015;91(19):1-5. doi:10.1103/PhysRevB.91.195427

48.   Mattioli F, Mazzeo G, Longhi G, et al. Plasmonic Superchiral Lattice Resonances in the Mid-Infrared. *ACS Photonics*. 2020;7(10):2676-2681. doi:10.1021/acsphotonics.0c00161

49.   Vázquez-Lozano JE, Martínez A. Toward Chiral Sensing and Spectroscopy Enabled by All-Dielectric Integrated Photonic Waveguides. *Laser Photonics Rev*. 2020;14(9):1-12. doi:10.1002/lpor.201900422

50.   García-Guirado J, Svedendahl M, Puigdollers J, Quidant R. Enhanced Chiral Sensing with Dielectric Nanoresonators. *Nano Lett*. 2020;20(1):585-591. doi:10.1021/acs.nanolett.9b04334

51.   Solomon ML, Hu J, Lawrence M, García-Etxarri A, Dionne JA. Enantiospecific Optical Enhancement of Chiral Sensing and Separation with Dielectric

Metasurfaces. *ACS Photonics*. 2019;6(1):43-49. doi:10.1021/acsphotonics.8b01365

52. Pellegrini G, Finazzi M, Celebrano M, Duò L, Biagioni P. Chiral surface waves for enhanced circular dichroism. *Phys Rev B*. 2017;95(24):1-5. doi:10.1103/PhysRevB.95.241402

53. Mogni E, Pellegrini G, Gil-Rostra J, et al. One-Dimensional Photonic Crystal for Surface Mode Polarization Control. *Adv Opt Mater*. 2022;10(21). doi:10.1002/adom.202200759

54. Daimon M, Masumura A. Measurement of the refractive index of distilled water from the near-infrared region to the ultraviolet region. *Appl Opt*. 2007;46(18):3811-3820. doi:10.1364/AO.46.003811

55. Gao L, Lemarchand F, Lequime M. Exploitation of multiple incidences spectrometric measurements for thin film reverse engineering. *Opt Express*. 2012;20(14):15734. doi:10.1364/oe.20.015734

56. Liu V, Fan S. S 4: A free electromagnetic solver for layered periodic structures. *Comput Phys Commun*. 2012;183(10):2233-2244. doi:10.1016/j.cpc.2012.04.026

57. Johnson PB, Christy RW. Optical Constants of the Noble Metals. *Phys Rev B*. 1972;6(12):4370-4379.

58. Sinibaldi A, Danz N, Descrovi E, et al. Direct comparison of the performance of Bloch surface wave and surface plasmon polariton sensors. *Sensors Actuators, B Chem*. 2012;174:292-298. doi:10.1016/j.snb.2012.07.015

59. Pellegrini G, Finazzi M, Celebrano M, Duò L, Biagioni P. Surface-enhanced chiroptical spectroscopy with superchiral surface waves. *Chirality*. 2018;30(7):883-889. doi:10.1002/chir.22971

60. Giorgis F, Descrovi E, Summonte C, Dominici L, Michelotti F. Experimental determination of the sensitivity of Bloch Surface Waves based sensors. *Opt Express*. 2010;18(8):8087. doi:10.1364/oe.18.008087

61. Homola J. Surface plasmon resonance sensors for detection of chemical and biological species. *Chem Rev*. 2008;108(2):462-493. doi:10.1021/cr068107d

62. Choi S, Yang Y, Chae J. Surface plasmon resonance protein sensor using Vroman effect. *Biosens Bioelectron*. 2008;24(4):893-899. doi:10.1016/j.bios.2008.07.036

63. Aguilar MI, Small DH. Surface plasmon resonance for the analysis of β-amyloid interactions and fibril formation in alzheimer's disease research. *Neurotox Res*. 2005;7(1-2):17-27. doi:10.1007/BF03033773

64. Paeder V, Musi V, Hvozdara L, Herminjard S, Herzig HP. Detection of protein aggregation with a Bloch surface wave based sensor. *Sensors Actuators, B Chem*. 2011;157(1):260-264. doi:10.1016/j.snb.2011.03.060

65. Qiao H, Guan B, Gooding JJ, Reece PJ. Protease detection using a porous silicon

based Bloch surface wave optical biosensor. *Opt Express*. 2010;18(14):15174. doi:10.1364/oe.18.015174

66. Danz N, Sinibaldi A, Michelotti F, et al. Improving the sensitivity of optical biosensors by means of Bloch surface waves. *Biomed Tech*. 2012;57(SUPPL. 1 TRACK-E):584-587. doi:10.1515/bmt-2012-4246

67. Deng CZ, Ho YL, Lee YC, et al. Two-pair multilayer Bloch surface wave platform in the near- and mid-infrared regions. *Appl Phys Lett*. 2019;115.

68. Chen J, Zhang D, Wang P, Ming H, Lakowicz JR. Strong Polarization Transformation of Bloch Surface Waves. *Phys Rev Appl*. 2018;9(2):24008. doi:10.1103/PhysRevApplied.9.024008

69. Gattass RR, Mazur E. Femtosecond laser micromachining in transparent materials. *Nat Photonics*. 2008;2(4):219-225. doi:10.1038/nphoton.2008.47

70. Correa DS, Cardoso MR, Tribuzi V, Misoguti L, Mendonca CR. Femtosecond laser in polymeric materials: Microfabrication of doped structures and micromachining. *IEEE J Sel Top Quantum Electron*. 2012;18(1):176-186. doi:10.1109/JSTQE.2011.2106764

71. Sugioka K, Cheng Y. Fabrication of 3D microfluidic structures inside glass by femtosecond laser micromachining. *Appl Phys A Mater Sci Process*. 2014;114(1):215-221. doi:10.1007/s00339-013-8107-3

72. Eaton SM, De Marco C, Martinez-Vazquez R, et al. Femtosecond laser microstructuring for polymeric lab-on-chips. *J Biophotonics*. 2012;5(8-9):687-702. doi:10.1002/jbio.201200048

73. Martínez Vázquez R, Eaton SM, Ramponi R, Cerullo G, Cerullo R. Fabrication of binary Fresnel lenses in PMMA by femtosecond laser micromachining. *Opt InfoBase Conf Pap*. 2011;19(12):11597-11604. doi:10.1364/cleo_at.2011.jmg5

74. Serafetinides AA, Makropoulou M, Fabrikesi E, et al. Ultrashort laser ablation of PMMA and intraocular lenses. *Appl Phys A Mater Sci Process*. 2008;93(1):111-116. doi:10.1007/s00339-008-4666-0

75. Eaton SM, Ng ML, Osellame R, Herman PR. High refractive index contrast in fused silica waveguides by tightly focused, high-repetition rate femtosecond laser. *J Non Cryst Solids*. 2011;357(11-13):2387-2391. doi:10.1016/j.jnoncrysol.2010.11.082

76. Haske W, Chen VW, Hales JM, et al. 65 nm feature sizes using visible wavelength 3-D multiphoton lithography. *Opt Express*. 2007;15(6):3426. doi:10.1364/oe.15.003426

77. Piliarik M, Homola J. Surface plasmon resonance (SPR) sensors: approaching their limits? *Opt Express*. 2009;17(19):16505. doi:10.1364/oe.17.016505

78. Sproul WD. New routes in the preparation of mechanically hard films. *Science (80- )*. 1996;273(5277):889-892. doi:10.1126/science.273.5277.889

79. Swann S. Magnetron sputtering. *Phys Technol*. 1988;19(2):67-75. doi:10.1088/0305-4624/19/2/304

80. Safi I. Novel reactive magnetron sputtering technique for producing insulating oxides of metal alloys and other compound thin films. *Surf Coatings Technol*. 2000;135(1):48-59. doi:10.1016/S0257-8972(00)00985-3

81. Schiller S, Beister G, Sieber W, et al. Influence of deposition parameters on the optical and structural properties of TiO2 films produced by reactive d.c. plasmatron sputtering. *Thin Solid Films*. 1981;83:239-245.

82. Rizk A, Habib SK. Glow discharge characteristics when magnetron sputtering copper in different plasma atmospheres operated at low input power. *Vacuum*. 1988;38(2):93-95.

83. Vossen JL, Krommenhoek S, Koss VA. Some experiments that provide direct visualization of reactive sputtering phenomena. *J Vac Sci Technol A Vacuum, Surfaces, Film*. 1991;9(3):600-603. doi:10.1116/1.577372

84. Yamamoto H, Maeda Y, Kitano H. Molecular recognition by self-assembled monolayers of cyclodextrin on Ag. *J Phys Chem B*. 1997;101(35):6855-6860. doi:10.1021/jp963916u

85. Ribeiro JC, Minas G, Turmezei P, Wolffenbuttel RF, Correia JH. A SU-8 fluidic microsystem for biological fluids analysis. *Sensors Actuators, A Phys*. 2005;123-124:77-81. doi:10.1016/j.sna.2005.03.032

86. Chang HK, Kim YK. UV-LIGA process for high aspect ratio structure using stress barrier and C-shaped etch hole. *Sensors Actuators, A Phys*. 2000;84(3):342-350. doi:10.1016/S0924-4247(00)00408-8

87. Lorenz H, Laudon M, Renaud P. MICROELECTRONIC ENGINEERING Mechanical Characterization of a New High-Aspect-Ratio Near UV-Photoresist. *Microelectron Eng*. 1998;41:371-374.

88. Machalek NS, Li C, Barton C, Yan G, Arthur KK. Universal Qualification of Near Ultraviolet Circular Dichroism Spectroscopy: Method Performance Parameters and Limits of Detection for Structural Differences. *J Pharm Sci*. 2020;109(12):3728-3733. doi:10.1016/j.xphs.2020.09.038

89. Ladokhin AS, Fernández-Vidal M, White SH. CD spectroscopy of peptides and proteins bound to large unilamellar vesicles. *J Membr Biol*. 2010;236(3):247-253. doi:10.1007/s00232-010-9291-0

90. Miles AJ, Wallace BA. Circular dichroism spectroscopy of membrane proteins. *Chem Soc Rev*. 2016;45(18):4859-4872. doi:10.1039/c5cs00084j

91.    Angelesky O V., Ushenco AG, Uschenko YA, Pishak VP, Peresunko AP. Statistical,correlation and topological approaches in Diagnostics of the Structure and Physiological State of Birefringent Biological Tissues. In: *Handbook of Photonics for Biomedical Science*. ; 2010:21-67.

92.    Aspermair P, Ramach U, Reiner-Rozman C, et al. Dual Monitoring of Surface Reactions in Real Time by Combined Surface-Plasmon Resonance and Field-Effect Transistor Interrogation. *J Am Chem Soc*. 2020;142(27):11709-11716. doi:10.1021/jacs.9b11835

93.    Piccinini E, Alberti S, Longo GS, et al. Pushing the Boundaries of Interfacial Sensitivity in Graphene FET Sensors: Polyelectrolyte Multilayers Strongly Increase the Debye Screening Length. *J Phys Chem C*. 2018;122(18):10181-10188. doi:10.1021/acs.jpcc.7b11128

94.    Decher G, Eckle M, Schmitt J, Struth B. Layer-by-layer assembled multicomposite films. *Curr Opin Colloid Interface Sci*. 1998;3(1):32-39. doi:10.1016/S1359-0294(98)80039-3

95.    Dubas ST, Schlenoff JB. Factors controlling the growth of polyelectrolyte multilayers. *Macromolecules*. 1999;32(24):8153-8160. doi:10.1021/ma981927a

96.    Siegerink B, Maino A, Algra A, Rosendaal FR. Hypercoagulability and the risk of myocardial infarction and ischemic stroke in young women. *J Thromb Haemost*. 2015;13(9):1568-1575. doi:10.1111/jth.13045

97.    Wilkinson DA, Pandey AS, Thompson BG, Keep RF, Hua Y, Xi G. Injury mechanisms in acute intracerebral hemorrhage. *Neuropharmacology*. 2018;134:240-248. doi:10.1016/j.neuropharm.2017.09.033

98.    Blaszykowski C, Sheikh S, Thompson M. Surface chemistry to minimize fouling from blood-based fluids. *Chem Soc Rev*. 2012;41(17):5599-5612. doi:10.1039/c2cs35170f

99.    Kotlarek D, Curti F, Vorobii M, et al. Surface plasmon resonance-based aptasensor for direct monitoring of thrombin in a minimally processed human blood. *Sensors Actuators, B Chem*. 2020;320(May):128380. doi:10.1016/j.snb.2020.128380

100.   Di Iorio D, Marti A, Koeman S, Huskens J. Clickable poly-l-lysine for the formation of biorecognition surfaces. *RSC Adv*. 2019;9(61):35608-35613. doi:10.1039/c9ra08714a

101.   Ma GJ, Ferhan AR, Jackman JA, Cho NJ. Conformational flexibility of fatty acid-free bovine serum albumin proteins enables superior antifouling coatings. *Commun Mater*. 2020;1(1). doi:10.1038/s43246-020-0047-9

102.   Fologea D, Ledden B, McNabb DS, Li J. Electrical characterization of protein molecules by a solid-state nanopore. *Appl Phys Lett*. 2007;91(5):1-9.

doi:10.1063/1.2767206

103. Lechner B, Hageneder S, Schmidt K, et al. In Situ Monitoring of Rolling Circle Amplification on a Solid Support by Surface Plasmon Resonance and Optical Waveguide Spectroscopy. *ACS Appl Mater Interfaces*. 2021;13(27):32352-32362. doi:10.1021/acsami.1c03715

104. Watson JD, Crick FHC. Molecular structure of nucleic acids. *Nature*. 1953;171:737-738. doi:10.1140/epja/i2001-10240-x

105. Umazano JP, Bertolotto JA. Optical properties of DNA in aqueous solution. *J Biol Phys*. 2008;34(1-2 SPEC. ISS.):163-177. doi:10.1007/s10867-008-9061-8

106. Samoc A, Miniewicz A, Samoc M, Grote JG. Refractive-Index Anisotropy and Optical Dispersion in Films of Deoxyribonucleic Acid. *J Appl Polym Sci*. 2007;105:23. doi:10.1002/app

107. Elhadj S, Singh G, Saraf RF. Optical properties of an immobilized DNA monolayer from 255 to 700 nm. *Langmuir*. 2004;20(13):5539-5543. doi:10.1021/la049653+

108. Finer EG, Darke A. Orientation of poly-L-lysine hydrobromide by magnetic fields. *J Chem Soc Faraday Trans 1 Phys Chem Condens Phases*. 1975;71:984-987. doi:10.1039/F19757100984

109. Nishioka M, Kikuchi K, Yoshioka K. Electro-optical properties of poly(ε-carbobenzosy-l-lysine) in organic solvents. *Polymer (Guildf)*. 1975;16(11):791-796. doi:10.1016/0032-3861(75)90108-1

110. Rodríguez-Maldonado L, Fernández-Nieves A, Fernández-Barbero A. Dynamic light scattering from high molecular weight poly-L-lysine molecules. *Colloids Surfaces A Physicochem Eng Asp*. 2005;270-271(1-3):335-339. doi:10.1016/j.colsurfa.2005.09.003

111. Canziani GA, Klakamp S, Myszka DG. Kinetic screening of antibodies from crude hybridoma samples using Biacore. *Anal Biochem*. 2004;325(2):301-307. doi:10.1016/j.ab.2003.11.004

112. Chang CW, Yang SY, Yang CC, Chang CW, Wu YR. Plasma and Serum Alpha-Synuclein as a Biomarker of Diagnosis in Patients With Parkinson's Disease. *Front Neurol*. 2020;10(January):1-7. doi:10.3389/fneur.2019.01388

113. Goedert M, Jakes R, Spillantini MG. The Synucleinopathies: Twenty Years on. *J Parkinsons Dis*. 2017;7(s1):S53-S71. doi:10.3233/JPD-179005

114. Twohig D, Nielsen HM. α-synuclein in the pathophysiology of Alzheimer's disease. *Mol Neurodegener*. 2019;14(1):1-19. doi:10.1186/s13024-019-0320-x

115. Iskierko Z, Sosnowska M, Sharma PS, et al. Extended-gate field-effect transistor (EG-FET) with molecularly imprinted polymer (MIP) film for selective inosine

determination. *Biosens Bioelectron*. 2015;74:526-533. doi:10.1016/j.bios.2015.06.073

116.    Sheibani S, Capua L, Kamaei S, et al. Extended gate field-effect-transistor for sensing cortisol stress hormone. *Commun Mater*. 2021;2(1):1-10. doi:10.1038/s43246-020-00114-x

117.    Shibata K, Nakamura A. An extended gate field-effect transistor (EG-FET) type non-enzymatic glucose sensor with inkjet-printed copper oxide nanoparticles. *SN Appl Sci*. 2022;4(10). doi:10.1007/s42452-022-05133-6

118.    Furlan de Oliveira R, Livio PA, Montes-García V, et al. Liquid-Gated Transistors Based on Reduced Graphene Oxide for Flexible and Wearable Electronics. *Adv Funct Mater*. 2019;29(46):1-11. doi:10.1002/adfm.201905375

119.    Ricci S, Casalini S, Parkula V, et al. Label-free immunodetection of α-synuclein by using a microfluidics coplanar electrolyte-gated organic field-effect transistor. *Biosens Bioelectron*. 2020;167(July):112433. doi:10.1016/j.bios.2020.112433

120.    Jonsson A, Inal S, Uguz L, et al. Bioelectronic neural pixel: Chemical stimulation and electrical sensing at the same site. *Proc Natl Acad Sci U S A*. 2016;113(34):9440-9445. doi:10.1073/pnas.1604231113

121.    Campos A, Riera-Galindo S, Puigdollers J, Mas-Torrent M. Reduction of Charge Traps and Stability Enhancement in Solution-Processed Organic Field-Effect Transistors Based on a Blended n-Type Semiconductor. *ACS Appl Mater Interfaces*. 2018;10(18):15952-15961. doi:10.1021/acsami.8b02851

122.    Campana A, Cramer T, Simon DT, Berggren M, Biscarini F. Electrocardiographic recording with conformable organic electrochemical transistor fabricated on resorbable bioscaffold. *Adv Mater*. 2014;26(23):3874-3878. doi:10.1002/adma.201400263

123.    Casalini S, Dumitru AC, Leonardi F, et al. Multiscale sensing of antibody-antigen interactions by organic transistors and single-molecule force spectroscopy. *ACS Nano*. 2015;9(5):5051-5062. doi:10.1021/acsnano.5b00136

124.    Parkula V, Berto M, Diacci C, et al. Harnessing selectivity and sensitivity in electronic biosensing: A Novel Lab-on-Chip Multigate Organic Transistor. *Anal Chem*. 2020;92(13):9330-9337. doi:10.1021/acs.analchem.0c01655

125.    White SP, Dorfman KD, Frisbie CD. Operating and Sensing Mechanism of Electrolyte-Gated Transistors with Floating Gates: Building a Platform for Amplified Biodetection. *J Phys Chem C*. 2016;120(1):108-117. doi:10.1021/acs.jpcc.5b10694

126.    White SP, Sreevatsan S, Frisbie CD, Dorfman KD. Rapid, Selective, Label-Free Aptameric Capture and Detection of Ricin in Potable Liquids Using a Printed Floating Gate Transistor. *ACS Sensors*. 2016;1(10):1213-1216.

doi:10.1021/acssensors.6b00481

127. White SP, Dorfman KD, Frisbie CD. Label-Free DNA Sensing Platform with Low-Voltage Electrolyte- Gated Transistors. *Anal Chem*. 2015;87:1861-1866.

128. Lai S, Barbaro M, Bonfiglio A. Tailoring the sensing performances of an OFET-based biosensor. *Sensors Actuators, B Chem*. 2016;233:314-319. doi:10.1016/j.snb.2016.04.095

129. Picca RA, Manoli K, Macchia E, et al. Ultimately Sensitive Organic Bioelectronic Transistor Sensors by Materials and Device Structure Design. *Adv Funct Mater*. 2020;30(20):1-23. doi:10.1002/adfm.201904513

130. Torricelli F, Adrahtas DZ, Bao Z, et al. Electrolyte-gated transistors for enhanced performance bioelectronics. *Nat Rev Methods Prim*. 2021;1(1). doi:10.1038/s43586-021-00065-8

131. Chen S, Liu L, Zhou J, Jiang S. Controlling antibody orientation on charged self-assembled monolayers. *Langmuir*. 2003;19(7):2859-2864. doi:10.1021/la026498v

132. Lu B, Smyth MR, O'Kennedy R. Oriented immobilization of antibodies and its applications in immunoassays and immunosensors. *Analyst*. 1996;121(3):29-32. doi:10.1039/an996210029r

133. Hearty S, Leonard P, Kennedy RO. *Chapter 24 Measuring Antibody – Antigen Binding Kinetics Using*. Vol 907. doi:10.1007/978-1-61779-974-7

134. Oh BK, Lee W, Kim YK, Lee WH, Choi JW. Surface plasmon resonance immunosensor using self-assembled protein G for the detection of Salmonella paratyphi. *J Biotechnol*. 2004;111(1):1-8. doi:10.1016/j.jbiotec.2004.02.010

135. Young MB, Oh BK, Lee W, Won HL, Choi JW. Study on orientation of immunoglobulin G on protein G layer. *Biosens Bioelectron*. 2005;21(1):103-110. doi:10.1016/j.bios.2004.09.003

136. Martin VS, Sullivan BA, Walker K, Hawk H, Sullivan BP, Noe LJ. Surface plasmon resonance investigations of human epidermal growth factor receptor 2. *Appl Spectrosc*. 2006;60(9):994-1003. doi:10.1366/000370206778397498

137. Welch NG, Scoble JA, Muir BW, Pigram PJ. Orientation and characterization of immobilized antibodies for improved immunoassays (Review). *Biointerphases*. 2017;12(2):02D301. doi:10.1116/1.4978435

138. Krivosudský O, Dráber P, Cifra M. Resolving controversy of unusually high refractive index of a tubulin. *Epl*. 2017;117(3):1-5. doi:10.1209/0295-5075/117/38003

139. Zhao H, Brown PH, Schuck P. On the distribution of protein refractive index increments. *Biophys J*. 2011;100(9):2309-2317. doi:10.1016/j.bpj.2011.03.004

140. Hasler R, Reiner-Rozman C, Fossati S, et al. Field-Effect Transistor with a

Plasmonic Fiber Optic Gate Electrode as a Multivariable Biosensor Device. *ACS Sensors*. 2022;7(2):504-512. doi:10.1021/acssensors.1c02313

# List of Figures